



HAL
open science

Une boîte quantique dans un fil photonique : spectroscopie et optomécanique

Inah Yeo

► **To cite this version:**

Inah Yeo. Une boîte quantique dans un fil photonique : spectroscopie et optomécanique. Autre [cond-mat.other]. Université de Grenoble, 2012. Français. NNT : 2012GRENY076 . tel-00809344

HAL Id: tel-00809344

<https://theses.hal.science/tel-00809344>

Submitted on 9 Apr 2013

HAL is a multi-disciplinary open access archive for the deposit and dissemination of scientific research documents, whether they are published or not. The documents may come from teaching and research institutions in France or abroad, or from public or private research centers.

L'archive ouverte pluridisciplinaire **HAL**, est destinée au dépôt et à la diffusion de documents scientifiques de niveau recherche, publiés ou non, émanant des établissements d'enseignement et de recherche français ou étrangers, des laboratoires publics ou privés.

THÈSE

Pour obtenir le grade de

DOCTEUR DE L'UNIVERSITÉ DE GRENOBLE

Spécialité : **PHYSIQUE/ PHYSIQUE DE MATIÈRE CONDENSÉE
ET DU RAYONNEMENT**

Arrêté ministériel : 7 août 2006

Présentée par

Inah YEO

Thèse dirigée par **Jean-Philippe POIZAT** et
codirigée par **Jean-Michel GERARD**

préparée au sein de l'**Institut Néel**
dans l'**École Doctorale de Physique de Grenoble**

A quantum dot in a photonic wire : spectroscopy and optomechanics

Thèse soutenue publiquement le **24 octobre 2012**,
devant le jury composé de :

Dr. Antoine HEIDMANN

Directeur de Recherche au Laboratoire Kastler Brossel (Président)

Dr. Isabelle ROBERT-PHILIP

Directrice de Recherche au Laboratoire de Photonique et de Nanostructures
(Rapporteure)

Dr. Sébastien SAUVAGE

Directeur de Recherche à l'Institut d'Electronique Fondamentale (Rapporteur)

Prof. Armando RASTELLI

Professeur à l'Université Johannes Kepler de Linz (Examinateur)

Dr. Jean-Michel GÉRARD

Ingénieur de Recherche à l'INAC/CEA Grenoble (Co-Directeur)

Dr. Jean-Philippe POIZAT

Directeur de Recherche à l'Institut Néel (Directeur)



To Sang-Keum Lee

Having gone through frustrating obstacles, I believe that God guided me to have an eventual success in the laboratory. Such guidance has come through my mother's prayer, nice colleagues in the institut Néel and CEA, and all of my friends.

Acknowledgements

First of all, this thesis would not be possible at all without the contribution of many colleagues in the institut Néel and CEA. A few years ago, I would not expect this thesis would contain such a variety of subjects within the main PhD objective. I believe that God indeed leads me to find such an exciting road during my PhD by invaluable guidances. So many times when I was discouraged with unexpected phenomena which seemed to be failed experiments, God taught me how to overcome the frustrating obstacles.

From the lab, I would first of all like to acknowledge my advisor, Dr. Jean-Philippe Poizat. His enthusiasm and insight to do challenging research have strongly impacted me by shaping my individual development as a scientist. He was always ready whenever I needed him for advice. He always encouraged me to go ahead no matter how discouraged I was. I gained valuable experiences thanks to his advising in my PhD work. I would also like to thank Dr. Signe Sidelin for her mentoring in the laboratory. I am also grateful to Edward Wagner, who was a labview programmer. His user-friendly programs particularly helped me doing the experiment. I would also like to thank Fabrice Donatini for his instrumental advices.

I would also like to acknowledge my co-advisor, Dr. Jean-Michel Gérard for his guidance throughout my dissertation. His critical comments and suggestions were crucial for the success of my research. His deep insight and knowledge in this project has greatly inspired me in constructive meetings.

I would like to acknowledge Dr. Gilles Nogues for his advising especially on the subject of surface effect. His idea stimulated me to work on this subject. He gave me very valuable suggestions and comments during my PhD. I am also thankful for his willingness to advice me with whatever was needed in the lab.

I would like to acknowledge Dr. Maxime Richard and Dr. Olivier Arcizet for their collaboration on the optomechanics subject. When I faced again with another unexpected problem after a nearly year and a half span of experiments, Maxime's suggestion and idea guided me to change front and find very interesting optomechanical properties of a trumpet-like photonic wire. His insight and knowledge greatly helped in my quantitative understanding of a strain-mediated quantum dot coupling. I also would like to acknowledge Dr. Olivier Arcizet for great experimental supports on the optomechanics subject. His guidance and experimental tips in the laboratory have greatly inspired me.

I would also like to express my appreciation to Dr. Dang for his mentoring as both an intellectual scientist and a nice human being. He sincerely advised my research during my PhD. Discussion with him indeed helped in sharpening my understanding of physics concepts.

I would also like to thank Dr. Henri Mariette, Director of the group NPSC, for his support and valuable comments in my PhD work. He did not hesitate to discuss my work and advise my PhD life even outside of his official hours at the bus station.

I would also like to thank Dr. Julien Claudon who provided fantastic trumpet-like wires. For theoretical support, I would like to thank Dr. Alexia Auffèves. I also thank to other fellows in the NPSC who have been a help: Lucien Besombes, Jacek Kasprzak, Pierre Louis de Assis, Nitin Singh Malik, Arnaud Gloppe, Eva Dupont-Ferrier, Mathieu Munsch, Emmanuel Dupuy and Joël Bleuse.

I would also like to express my sincere gratitude to the members of the jury, Dr. Isabelle Robert-Philip, Dr. Sébastien Sauvage, Dr. Antoine Heidmann and Prof. Armando Rastelli for refereeing my thesis and accepting to serve in the jury. I am deeply grateful for their constructive and keen comments which helped me to improve manuscript to its present shape. In particular, I would like to express my special thanks to Dr. Sébastien Sauvage, Prof. Armando Rastelli and Dr. Isabelle Robert-Philip for their careful proof-reading.

I would also like to express my deep gratitude to my master supervisor, Prof.Kyungsoo Lee in Pusan National University. As I started my first research in his theory group, he advised me to understand the physics in a prudent manner.

I also want to thank people who have been helping me during my three-year research: Junseok, Chonglong, Adalberto, Liu, Giang, Yenjing, Bao, Viet, Minki, Sutirtha, Heajeong, Kiyong, Paulo, Daniel, Igor, Emilien, Peter, Olivier and many others whose names I forgot to list.

Finally, I dedicate this dissertation to Rev.Sang-Keum Lee, who is my mother. Her pray was the most powerful force that has kept me on track and to reach my goals.

Abstract

Dans cette these, nous avons etudie les proprietes optiques de boites quantiques InAs/GaAs contenues dans un fil photonique. Des resultats anterieurs a cette these ont montre que ces fils photoniques permettent d'extraire les photons avec une efficacite tres elevee. Le premier resultat original de ce travail est l'observation de la derive temporelle de la raie d'emission de la photoluminescence d'une boite quantique. Cet effet a ete attribue a la lente modification de la charge de surface du fil due a l'absorption des molecules d'oxygene presentes dans le vide residuel du cryostat. Nous avons montre qu'une fine couche de Si₃N₄ permettait de supprimer cette derive. La derive temporelle pouvant etre differente pour differentes boites quantiques, nous avons pu tirer partie de cet effet pour mettre en resonance deux boites quantiques contenues dans le meme fil. Le deuxieme resultat original est la mise en evidence de la modification de l'energie d'emission d'une boite quantique soumise a une contrainte mecanique induite par la vibration du fil. Nous avons observe que le spectre de la raie d'emission d'une boite quantique s'elargit considerablement lorsque le fil est mecaniquement excite a sa frequence de resonance. A l'aide d'une illumination stroboscopique synchronisee avec l'excitation mecanique, nous avons pu reconstruire l'evolution du spectre d'une boite quantique au cours d'une periode de la vibration mecanique. L'amplitude de l'oscillation spectrale de la raie de luminescence depend de la position de la boite dans le fil a cause d'un tres fort gradient de contrainte. En utilisant deux modes d'oscillation mecanique de polarisations lineaires et orthogonales, nous pouvons extraire une cartographie complete de la position des boites quantiques a l'interieur du fil. Enfin, grace a ce gradient, on peut, dans certains cas, trouver une position du fil pour laquelle deux boites quantiques peuvent etre amenees en resonance.

Contents

List of Figures	ix
1 Introduction	1
1.1 Single Photon Source	1
1.1.1 QD-based Single Photon Source	3
1.1.1.1 Resonant Spontaneous Emission Control: Purcell Effect	3
1.1.1.2 Non Resonant Spontaneous Emission Control: Single- photon Optomechanics in One-dimensional Waveguide .	5
1.1.1.3 Surface Effect	8
1.1.1.4 Strain-mediated Dynamic Control	9
1.1.2 Thesis Outline	9
2 Self-Assembled InAs Quantum Dots	13
2.1 Self-assembled InAs QD	13
2.2 InAs QD as a Single Photon Emitter	14
2.2.1 Discrete Energy State	14
2.2.2 QD Charging and Single Photon Emission	16
2.2.3 Complex Excitonic States	18
2.3 Interaction of QD with Light in a Photonic Wire	19
2.3.1 QD Decay in the Bulk	20
2.3.2 QD Decay in a Photonic Wire	21
2.3.2.1 Modified Spontaneous Emission Rate	22
2.3.3 Global Efficiency	23
2.3.4 Sample Summary	25
2.3.4.1 Cylindrical Photonic Wire: Champion	26

CONTENTS

2.3.4.2	Conical Photonic Wire: Trumpet	27
2.4	Chapter Summary	28
3	Optical Spectroscopy of a Single InAs QD in a GaAs photonic wire	29
3.1	Experimental Setup	30
3.1.1	Optical Source	31
3.1.1.1	Non Resonant Excitation	31
3.1.1.2	Quasi Resonant and Resonant Excitations	31
3.1.2	Cryogenics	32
3.1.3	Spectrometer	33
3.1.3.1	CCD	33
3.2	QD Characterization with photoluminescence Spectroscopy	33
3.3	Single Photon Emission via Photoluminescence Excitation Spectroscopy	37
3.4	Temperature-dependent Photoluminescence Excitation Spectroscopy . .	41
3.5	Temperature-dependent Photoluminescence Spectroscopy	43
3.6	Chapter Summary	45
4	Surface effects in a semiconducting photonic wire; spectral stability of an embedded single QD	47
4.1	Electronic Surface States in p-type Semiconductor	48
4.2	Band Bending in p-doped Photonic Wires	49
4.3	Emission Energy Drift of an Embedded Single QD	52
4.4	Spectral Tuning of QDs	60
4.4.1	Two QD Crossing: Continuous Tuning	61
4.4.2	Giant Blue Shift	63
4.5	Chapter Summary	66
5	Strain-induced optomechanical coupling for quantum dots in photonic wires	67
5.1	Band Structure of InAs/GaAs System	69
5.1.1	$\mathbf{k} \cdot \mathbf{p}$ theory	72
5.1.2	Influence of Stress on InAs/GaAs Structures	73
5.1.2.1	Pikus-Bir Hamiltonian for Bulk Semiconductors	73
5.1.2.2	Influence of Intrinsic Stress on InAs/GaAs Structure	76

5.1.2.3	Influence of an Applied Uniaxial Stress on InAs/GaAs Structure	77
5.1.2.4	Other Effects of Strain on QD Confinement Potential Well	78
5.2	Strain Effect on Oscillating GaAs Photonic Wires Embedding InAs QDs	82
5.2.1	Flexural Eigenmodes	82
5.2.2	Strain-field Coupling Strength with QDs	85
5.2.3	QD Response to Mechanical Strain	86
5.3	Optomechanical Characterization of GaAs Photonic Wires	90
5.3.1	Optomechanical Setup	91
5.3.1.1	Optical Detection: Split-photodiode	93
5.3.1.2	Micro-positioning of Photonic Wire in Optical Waist . .	93
5.3.1.3	Displacement Calibration	95
5.3.1.4	Ratio of AC and DC Gains	96
5.3.2	Measured Mechanical Response: Q Factor	97
5.3.3	Strain Effects on QD Emission Energy	99
5.3.4	Mechanical Resonance Effects on Collected Photoluminescence .	102
5.3.5	Stroboscopic Illumination	104
5.3.6	QD Spatial Mapping	109
5.3.7	Mechanical Bistability	115
5.4	Chapter Summary	121
6	Conclusions and Outlook	123
	References	125

CONTENTS

List of Figures

1.1	Ideal single photon emission	1
1.2	Spontaneous emission control in Purcell effect based cavity systems. . .	4
1.3	Spontaneous emission control mechanism in an one-dimensional atom .	6
1.4	SEM images of a trumpet-like GaAs photonic wire embedding self-assembled InAs QDs	10
2.1	Self-assembled InAs QDs grown by a Stransky-Krastanov method	14
2.2	Potential profile of a self-assembled InAs quantum dot in the growth direction	15
2.3	A schematics of the QD energy band digram of the studied self-assembled InAs QD embedded in a GaAs matrix	16
2.4	Schematic multiparticle states of a single QD	18
2.5	Schematic guided mode of a photonic nanowire embedding a QD	22
2.6	Photon emission in a one-dimensional waveguide	24
2.7	Schematic diagram of two photonic nanowires embedding a single QD .	25
2.8	Tapered cylindrical photonic wire	26
2.9	Geometry of the conical photonic wire	27
3.1	Schematic diagram of photoluminescence measurement setup	30
3.2	Power-dependent photoluminescence spectra on a single QD embedded in the GaAs photonic wire taken at T=4.5 K	34
3.3	Excitation intensity dependence of photoluminescence spectra from dif- ferent photonic wires	35
3.4	Power dependence of the photoluminescence linewidths from different photonic wires	36

LIST OF FIGURES

3.5	The photoluminescence excitation spectra in a GaAs photonic wire with a diameter of 200nm at 4K	37
3.6	PLE spectrum of a single QD in a GaAs photonic wire with a diameter of 200 nm at 4 K	39
3.8	High temperature PLE spectrum of a single QD in a GaAs photonic wire with a diameter of 200nm	42
3.9	Temperature-dependence of integrated photoluminescence intensities peak evolution of a single InAs QD in a GaAs photonic wire with the diameter of 200 nm	43
3.10	Temperature-dependence of the photoluminescence peak evolution of a single InAs QD in a GaAs photonic wire with the diameter of 200 nm	45
4.1	Schematic diagram for the Fermi-level pinning mechanism in p-type semiconductor	50
4.2	Schematic of a band bending profiles in p-type photonic wires with different radii R	51
4.3	Schematic diagram for the Fermi-level pinning mechanism in p-type GaAs semiconductor	52
4.4	Photoluminescence spectra and blue-drift for a single InAs QD in a GaAs photonic wire	53
4.5	Blue drift in a bare photonic wire	54
4.6	Schematics of oxygen physisorption process for p-doped GaAs photonic wire surface at the QD level	56
4.7	The electronic energy level diagram of physisorbed O_2 for p-doped GaAs photonic wire surface at the QD level	57
4.8	Temperature dependence of the temporal drift	58
4.9	Power dependence of the blue-drift	59
4.10	Time dependence of QD detuning in a GaAs photonic wire with a diameter of 370 nm.	61
4.11	Time dependence of photoluminescence spectra in a GaAs photonic wire with a diameter of 370 nm.	62
4.12	Spectral tuning of a single QD with 20 K temperature cycle	64
4.13	Reproducible blue shift after several 20 K temperature cycles	64

4.14 ΔE_{PL} versus time and 20 K temperature cycle for excitation power $P/P_{\text{sat}} = 0.2$ in a bare photonic wire	65
5.1 Dynamics of trumpet-like GaAs photonic wire embedding self-assembled InAs QDs	68
5.2 Strain effects on InAs system	70
5.3 Deformation of crystal from the unstrained lattice (a) to the strained lattice (b)	74
5.4 Strain-induced modification in InAs band structures	77
5.5 Schematic diagram of an infinite QD potential well	80
5.6 Simulated eigenfrequency of GaAs photonic wires	84
5.7 Simulated eigenfrequency of GaAs photonic wires	85
5.8 Simulated coupling strength of GaAs photonic wires	86
5.9 Mechanical effects on InAs quantum dots embedded in a resonantly oscillating GaAs photonic wire	87
5.10 Oscillating vertical GaAs photonic wire embedding InAs QDs at its resonant frequency	89
5.11 Experimental setup for the nano-optomechanical characterization of a GaAs photonic wire	90
5.12 Schematics of the detection setup for imaging vibrating wires	92
5.13 Static 2D map	94
5.14 Static 2D map	95
5.15 Mechanical resonance characteristics of a GaAs photonic wire of diameter $D_{\text{Top}} = 1.98 \mu\text{m}$	98
5.16 Two orthogonally polarized mechanical modes of a GaAs photonic wire	100
5.17 Mechanical resonance characteristics on QD photoluminescence spectra	101
5.18 Signatures of wire dynamics	103
5.19 The normalized integrated intensity of the single QD embedded in a photonic wire by increasing the driving the piezo voltage	104
5.20 Stroboscopic setup	105
5.21 Stroboscopic illumination	106
5.22 Stroboscopic photoluminescence measurement	107
5.23 Stroboscopic tuning of two individual QDs	108

LIST OF FIGURES

5.24	Phase-amplitude polar plots of embedded QDs in a vibrating GaAs photonic wire of diameter 720 nm	109
5.25	Statistics on single exciton emission lines obtained for several size of wires	111
5.26	QD spatial mapping	112
5.27	Power dependence of single QDs embedded in the GaAs photonic wire of top diameter 1.98 μm	114
5.28	Hysteresis phenomenon in the nonlinear frequency response of GaAs photonic wire embedding InAs QDs	115
5.29	Temperature dependence of the mechanical resonance frequency for GaAs photonic wire of $D_{Top}=1.97 \mu\text{m}$	116
5.30	Temperature dependence of energy dissipation for GaAs photonic wire of $D_{Top}=1.97 \mu\text{m}$	117
5.31	Comparison of the strain-induced spectral shift for up- and down-sweep experiments of Fig.5.28	118
5.32	Color coded waterfall plot of the photoluminescence spectra for forward and reversed sweeping in the frequency domain.	119
5.33	Strain effects on the QD emission lines at 630 mV	120

1

Introduction

1.1 Single Photon Source

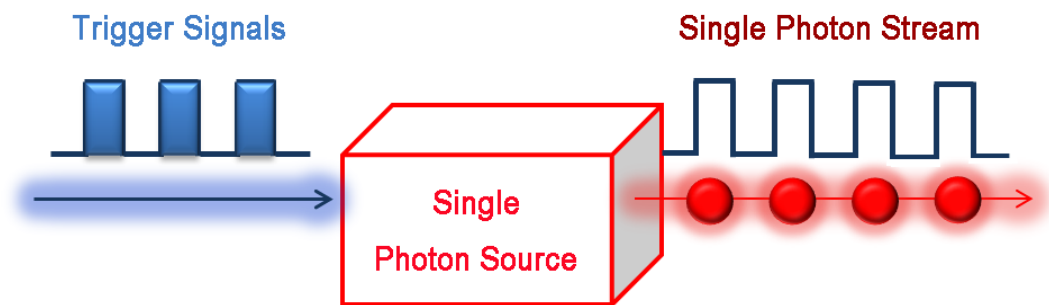


Figure 1.1: Ideal single photon emission - After an optical or electrical triggering, a single photon source emits photon one by one at a time.

Single photon source, simply put, is a device capable of emitting only one photon after each triggering signal. In the last decades, numerous research studies have been done for developing “on-demand” single photon devices. Such research interests stem from superior performance of single photon devices over attenuated Poissonian sources for various tasks in the field of quantum communication protocols (1, 2, 3), quantum information processing (4), etc. As the quantum nature of single photon source enables the superposition of two-level states and quantum entanglement, such single photon device is applicable for quantum key distribution, which allows two parties to share a random key securely. The quantum light source brings the information in several degrees of freedom of quantum states, for example, polarization, time-bin, path, etc.

1. INTRODUCTION

Furthermore, quantum properties at the single photon level promise advantages in device applications such as low power optics (optical nonlinearities) (5), metrology (6, 7), and fields yet to be identified. All these demanding functionalities impose that each emitted photon should be in the same quantum state. This criteria means that the emitted photon should have a well-defined emission energy and polarization at the same spatial mode. Indistinguishability achieved in this way enables further application of a linear optical quantum computing.

The first experimental step towards “on-demand single photon device” was conducted by Kimble et al. in 1977 (8); Kimble et al. demonstrated the production of antibunched photons via resonance fluorescence of sodium atoms. This experiment was further improved by holding a single atomic ion in electromagnetic traps via laser cooling (9, 10, 11). Similar type of complementary experiments have been performed as well on a single organic molecule, which allow much easier and practical setup (12, 13, 14). Light antibunching of the fluorescence from single organic molecules has been demonstrated at low temperature (12) and even at room temperature (13). However, these molecules become inactive typically after about 10^9 emissions due to the interaction with environment (photo-bleaching).

Other schemes of single photon source have then led to their implementation in solid state systems. These devices typically feature high quantum efficiency without photo-bleaching. One such solid state system is color centers in synthetic diamond crystals. A continuous stream of antibunched photons from single color centers has been demonstrated at room temperature (15, 16). Still a drawback is impractical incorporation of the emitters into devices.

An alternative scheme uses semiconductor *quantum dots* (QDs). Traditionally, QDs are referred to as “artificial atom”, which is capable of confining carriers in quantized energy levels. Such QDs can behave as an atomic two-level transitions. A continuous stream of single photons from QDs has been observed (17, 18, 19) by using pulsed laser trigger, as for single molecules.

The QDs have several attractive features as a single photon source. For example, QDs offer high quantum efficiencies and oscillator strengths. A particularly appealing feature is their photostabilities, thereby free from photo-bleaching or -blinking. Unlike Diamond color centers, QDs are also compatible for further integration into larger photonic structures. This last advantage is significant to harvest single photons in a

well-guided mode. This is the type of object that will be studied in this thesis. The following section will discuss the implementation of QDs in nanophotonic structures.

1.1.1 QD-based Single Photon Source

As mentioned, designing single photon device based on QDs in a nanophotonic structures (18, 20, 21) has been a fascinating strategy for further scalability and improving the collection efficiency. In order to realize the QD-based single photon device, it is necessary to control quantum states of single QD efficiently.

Hence, the key idea of QD-integrated single photon devices is based on tailoring the spontaneous decay of a single QD. Spontaneous emission is a process where a QD emits a photon by decaying to the lower energy state. For simplicity, the QD can be approximated as a two-level system. The ground and excited states of a two-level system are then denoted by $|g\rangle$ and $|e\rangle$ respectively, whose energy separation is $\hbar\omega_0$. The spontaneous emission is set by the Fermi's Golden rule:

$$\Gamma = \frac{2\pi}{\hbar^2} |\langle e | -\mu \cdot \mathbf{E} | g \rangle|^2 \rho(\omega_0), \quad (1.1)$$

with μ the dipole operator, \mathbf{E} the electric field at the position of the dipole emitter and $\rho(\omega_0)$ the photonic mode density at the emission frequency ω_0 . Viewing the spontaneous emission rate in Eq.(1.1), one can clearly read that the electromagnetic environment modifies the decay rate of an electric dipole. Adjusting the photonic mode density is, therefore, at the heart of spontaneous emission control in nanophotonic structures of different dimensionality: a homogeneous bulk medium (3D), a quantum well (2D), a quantum wire (1D) and a cavity (0D).

1.1.1.1 Resonant Spontaneous Emission Control: Purcell Effect

One successful approach of spontaneous emission control has been to embed a single emitter in a 0D cavity and to enhance the spontaneous emission rate selectively in a cavity resonant mode. The so-called ‘‘Purcell effect’’ has been proposed in 1946 (22) and stated that an electromagnetic resonator (a cavity) can strongly enhance the spontaneous emission rate of an embedded emitter. Following this idea, D. Kleppner has proposed (23) and observed (24) the inhibition of the spontaneous emission rate of Rydberg atoms via a cavity in 1980s. In the meantime, the ‘‘Purcell effect’’ has been demonstrated by Serge Haroche et al. using as well Rydberg atoms (25).

1. INTRODUCTION

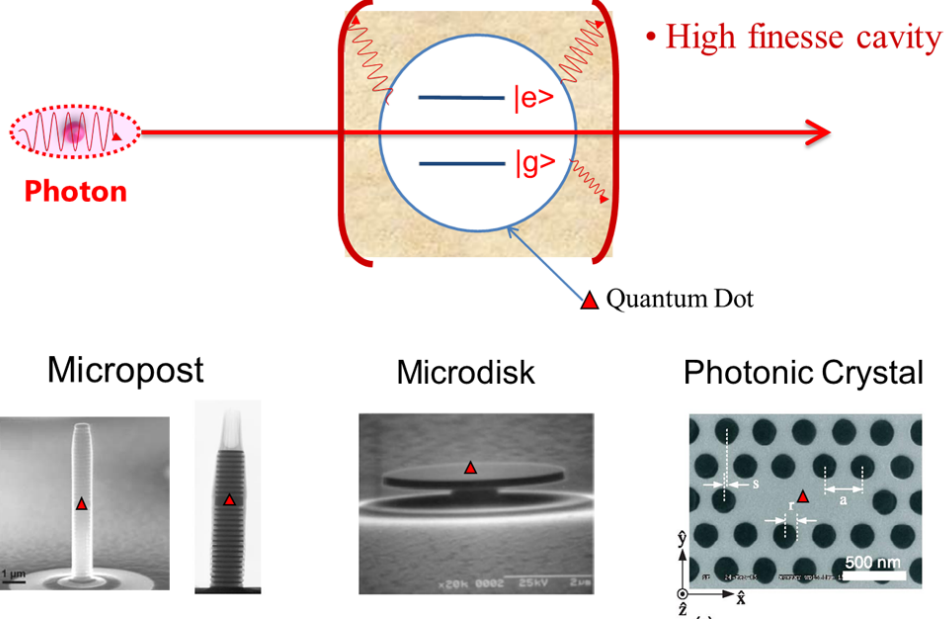


Figure 1.2: Spontaneous emission control in Purcell effect based cavity systems.
 - SEM images of micropost (26, 27), microdisk (17) and photonic crystal nanocavity (28).

Cavity is a 0D photonic structure whose electromagnetic field is confined in all directions resulting in an atom-like discrete energy density of states. Since the cavity has its intrinsic loss with a rate of κ , a localized cavity mode has a certain width of $\delta\omega$ given by κ . The spectral density of the cavity mode is described as a normalized Lorentzian distribution. For a single mode cavity in resonance with the two-level transition, the spontaneous emission rate of a quantum emitter of emission frequency ω is then given by

$$\Gamma_{cav}(\omega) = \frac{2}{\hbar^2} |\langle e | -\boldsymbol{\mu} \cdot \mathbf{E} | g \rangle|^2 \frac{\delta\omega/2}{(\omega_c - \omega)^2 + (\delta\omega/2)^2}, \quad (1.2)$$

with the resonance frequency $\omega_c = \omega_0$ and the full width at half maximum $\delta\omega$. Comparing a spontaneous emission rate Γ_0 of the quantum emitter in a bulk GaAs medium, the maximum spontaneous emission rate Γ_{cav} can be captured by the ‘‘Purcell factor’’ (22):

$$F(= \frac{\Gamma_{cav}}{\Gamma_0}) = \frac{3Q}{4\pi^2 V} \left(\frac{\lambda_c}{n}\right)^3 \quad (1.3)$$

at the emitter’s spatial and spectral mode maximum, aligned along the cavity mode field. Here, λ_c is the emission wavelength of the cavity resonance in vacuum, $Q = \omega_c/\delta\omega$ is the quality factor of the mode, and V is the mode volume of the cavity. To enhance

the spontaneous emission rate of the emitter in a cavity, high Q factor and small mode volume V are then required as seen by Eq.(1.3).

Within this purpose, since the early 1990's, several types of the single photon device based on a QD inserted in a cavity have been proposed and developed: micropost (26, 27, 29, 30, 31, 32), microdisk (17, 33) and photonic crystal nanocavity (20, 28, 34, 35, 36). Figure 1.2 shows the high quality cavity systems. On top of Fig. 1.2, a schematic diagram shows the idea of cavity systems; if the QD frequency matches with a cavity frequency, the spontaneous emission is considerably enhanced and collected within a narrow cavity mode. For the cavity systems with $Q > 1000$, the enhanced spontaneous emission around 900 nm can be collected efficiently in a cavity mode of width below $\Delta\lambda=1$ nm.

Regarding the inhomogeneous distribution of self-assembled InAs QDs of about 50 nm typically, the high frequency selectivity, however, is a constraint since it requires frequency matching between the QD and the cavity.

1.1.1.2 Non Resonant Spontaneous Emission Control: Single-photon Optomechanics in One-dimensional Waveguide

As a mean to achieve both highly efficient and broad-band single photon emissions, an alternative approach has been employed by integrating QDs in one-dimensional waveguides (37, 38). Once a single QD is photo-excited in one-dimensional waveguides, their recombinations at different energy will couple only with the one-dimensional guided mode. A large fraction (90%) of the spontaneous emission of the QD is collected by the waveguide. This property is featured over a bandwidth of 70 nm around 950 nm. On a route toward the single photon source, the one-dimensional GaAs photonic wire can be used to demonstrate the giant nonlinearity of an embedded single QD. This was the initial objective of my PhD. The idea is to experimentally demonstrate the single atom nonlinearity on an input field. In detail, at low excitation levels of less than one photon per QD lifetime, the weak incident field interferes destructively with the QD scattered photons. As the QD saturates with only one probe photon per QD lifetime, incomplete interference between the driving field and QD allows the light to be transmitted. The QD response to the driving field is highly nonlinear as the QD saturates. Such nonlinearities hold great promise for applications of ultra low-power optical switching (5, 39) and quantum nondemolition measurement of photons (40, 41, 42).

1. INTRODUCTION

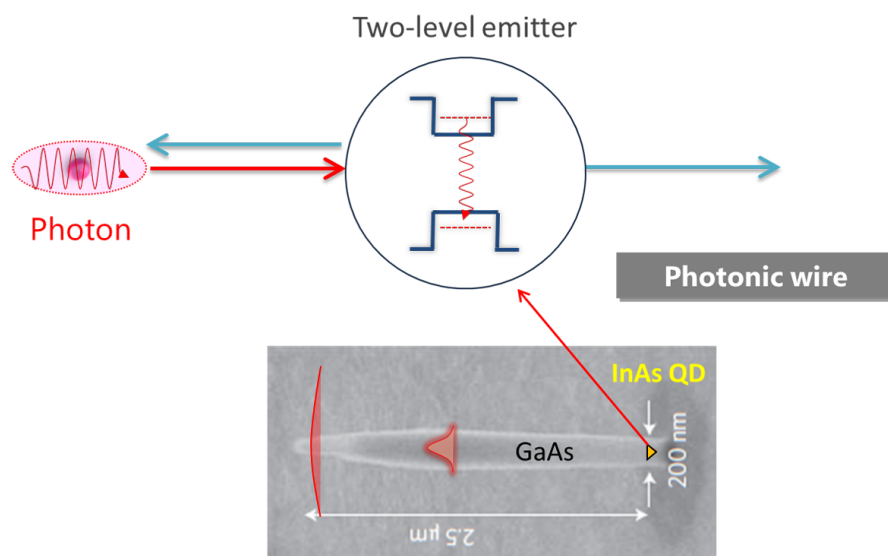


Figure 1.3: Spontaneous emission control mechanism in an one-dimensional atom - One-dimensional atoms are schematically viewed with SEM image of a regular taper wire. One-dimensional atom denotes the two-level emitter that mainly interacts with a single spatial electromagnetic mode. Photonic wire embedding QD (two-level system) provides only one single spatial mode that interacts with photons. Yellow triangle illustrates the two-level emitter. Red arrow represents the incident probe field. Blue arrow represents reflected or transmitted light. Our GaAs sample acts as an one-dimensional photonic waveguide.

Such kind of the photon-photon interaction has been demonstrated by Turchette et.al. (43) in an atomic system. An important restriction on this type of measurement is given by the one-dimensional spatial electromagnetic mode that only interacts with the two-level emitter. Among the solid-state implementation of the pioneering approach, the one-dimensional waveguide can be an adequate structure (44). This interaction scheme can therefore be exploited by the large nonlinearity of a single QD that is embedded in an one-dimensional GaAs photonic wire. Figure 1.3 illustrates one-dimensional waveguide candidates embedding a single QD for giant nonlinearity.

Certainly there is another restriction that has to be considered: the energy level of two-level emitter has to be stable enough for strict resonant pumping. Strikingly, QD emission lines in our one-dimensional photonic wire showed temporal blue-drift continuously. Thus, it was extremely difficult to follow the drifting excitonic lines and excite them resonantly. We were suspicious of surface effects on QD properties due to the large surface-to-volume ratio of the wire of few hundreds nanometer diameter. Then a proper surface passivation stopped the drift, as will be discussed in Chapter.4.

Still there was another problem; the QD linewidth was rather broad. Note that interactions of embedded QD emitters with the solid state environment leads to random fluctuations in the QD emission energy, thereby broadening their linewidths (45). As a suspect, we worried that the Brownian motion of miniature wires could degrade the stability of the QD emission energy. In particular, our trumpet-like photonic wire has a large dynamic strain-mediated coupling with QDs. Eventually, it turned out that there was negligible effects on the linewidths of QDs. However, this question led us to find exciting possibilities of the dynamic control of a single quantum level via the mechanical motion of the GaAs photonic wire. Thanks to the position of single QDs close to the bottom of the wire, the strain is rather large for the first flexural mode of the wire. Owing to the QD location, we gained a rather large dynamical strain-mediated coupling. Several interesting subjects have then studied in this thesis, for example, strain-mediated QD tuning, QD crossing, and QD mapping. The strain-mediated dynamic coupling with single QDs will be discussed in details later on in Chapter.5.

To summarize, we demonstrate several ways to manipulate quantum states of embedded single QDs in GaAs 1D photonic wires in a route towards QD-based single photon devices. In details, quantum properties of single QDs rely on such ingredients:

1. INTRODUCTION

- Size, shape and composition of QD,
- Random defect surrounding QD,
- Temperature,
- Built-in (surface) electric fields,
- Strain-induced fields.

In this thesis, we will specifically manipulate and control QD emission energies via built-in surface electric and strain-induced fields in one-dimensional GaAs photonic wires embedding single InAs QDs.

1.1.1.3 Surface Effect

In view of highly efficient and broad-band single photon emissions in one-dimensional photonic waveguide, the advantages comes from its lateral nanoscale size of about 100 nm. Photonic nanowire has been proven to be a highly efficient one-dimensional waveguide (38). The miniaturization of the photonic device, however, makes the system highly sensitive to the environment of surface, possibly affecting the emission properties of single photon emitters embedded in photonic wires. Due to the large surface to volume ratio, numerous surface states can effectively pin the Fermi level by bending the band profiles and depleting free carriers near the surface. Furthermore, the electronic states at the surface can be modified by adsorbing (desorbing) molecules (ex., oxygen) even in a cryostat vacuum of about $10^{-5}mbar$. Since QD energy levels are linked to the band-gap profile of the wire, this surface modification results in spectral instability of QD emission line.

These problems with the surface have been investigated intensively in a photonic nanowire. Several surface passivation techniques at least partially overcame these spectral drift by isolating the core of photonic wire from the surface. Nevertheless, the spectral instability of photonic wires, crucial for resonant quantum optics experiments, has not been investigated so far.

In this thesis, we will study temporal spectral instability of QD emission lines and its proper treatment for GaAs photonic wire embedding self-assembled InAs QDs, using high resolution photoluminescence spectroscopy. We will present the continuous drift

of QD excitonic emission line towards high energy-side in vacuum at low temperature. Possible origin and proper passivation will be discussed. We will also show the utility of the surface electric field as a versatile tuning tool.

1.1.1.4 Strain-mediated Dynamic Control

Another issue that has been considered in this work is the mechanical motion of miniature wires. As previously discussed, the GaAs photonic wire studied in this thesis has been designed for efficient single photon production. Within this purpose, the dot is located at a place where the optimum confinement of the guided mode is achieved. In our work, single QDs are very close to the bottom in the trumpet-like photonic wire, as shown in Fig. 1.4. The dynamical strain is then large for the fundamental flexural modes of the wire. Hence, dynamic motion of wires can induce considerable strain effects onto embedded single QDs in the photonic wire. This thesis therefore investigates the strain-mediated manipulation of QD emission properties. We will stroboscopically tune QD emission energies via large strain-mediated coupling. From the strength and the phase of this coupling, we will draw the two-dimensional spatial map of embedded QDs in the photonic wire with a sub-wavelength accuracy.

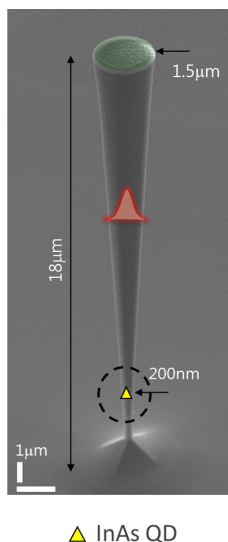


Figure 1.4: SEM images of a trumpet-like GaAs photonic wire embedding self-assembled InAs QDs - Yellow triangle illustrates the InAs QD. Self-assembled InAs QD is embedded 3 μm from the bottom of the wire.

1. INTRODUCTION

1.1.2 Thesis Outline

In this thesis, the experiments are performed on embedded self-assembled InAs QDs in vertical photonic nanowires. Followed by this introduction, this thesis is organized as follows:

Chapter 2 describes InAs QD single photon devices based on vertical photonic wires. This chapter begins with the description of general band structure of self-assembled InAs dots and their carrier properties. Sample structures are then presented and their specific features on single QD studies are discussed.

Chapter 3 discusses the optical characterization of single self-assembled InAs QDs embedded in a vertical photonic wire. In this chapter, a high resolution optical setup is described for single QD spectroscopy at cryogenic temperatures of liquid helium. Optical characterizations of single QDs are then presented via photoluminescence and photoluminescence excitation spectroscopies. These studies form the basic for the following chapters.

Chapter 4 discusses surface effects of nano-scale photonic devices which affect QD emission properties embedded in photonic wires. Experimental efforts to deal with the surface effects in a GaAs photonic nanowire are presented in this chapter. Chapter 4 first presents a continuous temporal drift of the QD emission energy. A possible mechanism of this phenomena is discussed by studying the influence of temperature and excitation laser power on this temporal drift. The phenomenon is attributed to oxygen adsorption onto the sidewall of the wire. A proper surface passivation is then demonstrated by achieving the spectral stability of the QD emission line. This is the first study of the spectral stability of photonic wires embedding QDs, crucial for resonant quantum optics experiments. For the other side, this chapter also shows that the surface effect can be an effective tool to tune QDs embedded in a photonic nanowire. Preliminary results of tunable coupled-QDs are then presented by utilizing the surface effect in a controlled way.

In Chapter 5, the spectral modulation of individual InAs QD emission lines is explored in nanowires undergoing mechanical oscillations. Chapter 5 represents a first signature of dynamical strain-mediated coupling between nanomechanical oscillators and QDs. First, we discuss the experimental setup employed in optomechanical studies

covered in this chapter. The mechanical oscillation is driven with a piezoelectric transducer attached at the back of the sample holder. The mechanical oscillation induces dynamical stress on the QDs which modulates in turn the QD emission energy. By performing the stroboscopic photoluminescence spectroscopy at the mechanical resonance frequency, the full time-dependent spectral lineshape is reconstructed by varying the phase between the optical and mechanical excitations. Careful phase adjustments leads to stroboscopic tuning of the photoluminescence energy of a QD over 0.5 meV. In particular, two QDs which were located in the same photonic wire but experiencing different strains can be brought into resonance.

Chapter 6 concludes this thesis with a short summary of our works and future perspectives.

1. INTRODUCTION

2

Self-Assembled InAs Quantum Dots

Single semiconductor QD is a promising candidate for single photon sources. Single QD is often referred as an artificial atom. The QD is in general a nanoscale region of relatively narrow-bandgap semiconductor (ex., InAs) in a wide-bandgap semiconductor (ex., GaAs). The reduced-bandgap region creates a potential well, which leads to a confinement of electron and hole carriers on the nanometer scale. The confinement in this region leads to quantize the energy levels of electron and hole carriers in the QD. Inside the QD, exciton is formed by an electron and hole pair due to the attractive electrostatic Coulomb force. The exciton recombination by emitting photon thus reveals the characteristics of quantum mechanical electronic states in the QDs.

2.1 Self-assembled InAs QD

Self-assembled semiconductor QDs realize thoroughly the above features of the QD. Self-assembled InAs QDs embedded in a GaAs substrate, the type investigated in this thesis, are a well-characterized prototype of self-assembled dot. A lot of research of self-assembled InAs QDs has been conducted in a wide range of high-performance optoelectronic devices, such as high-temperature operating infrared photodetectors (46), low-threshold and temperature-stable laser diodes (47), wide bandwidth superluminescent diodes (48), and single photon sources (38) for quantum cryptography. However, the key characteristics and availability of self-assembled InAs QDs depend very much

2. SELF-ASSEMBLED INAS QUANTUM DOTS

on the growth condition which strongly influences their size, shape, and the wetting layer structure.

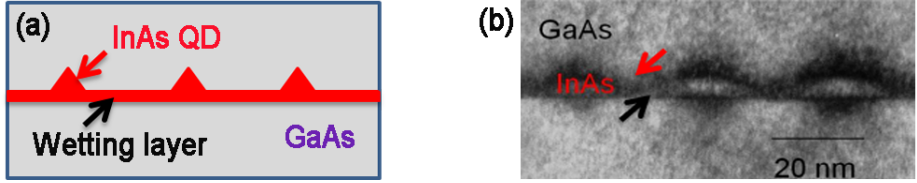


Figure 2.1: Self-assembled InAs QDs grown by a Stransky-Krastanov method - (a) The simple sketches schematically show a self-assembled single InAs QD grown by the Stransky-Krastanov method. (b) Transmission electron microscopy image of a self-assembled single InAs QD

Self-assembled InAs QDs are grown by molecular beam epitaxy by the Stransky-Krastanov growth method. When the InAs material is deposited on the surface of GaAs, a strained InAs monolayer is first formed which is referred to as the wetting layer. Since InAs has a lattice mismatch of 7% with GaAs, further growth of InAs on the GaAs substrate begins to form strained InAs islands on the wetting layer. The island is the QD, whose dimensions are about few tenth of nanometer (20-30nm) in diameter and about 2~3 nm in height. The strained InAs island are then capped by a layer of GaAs. Due to the low areal density of QD layer of about $300 \mu\text{m}^{-2}$, for example, a 200 nm-diameter wire typically contains 10 randomly located self-assembled InAs QDs. As illustrated in Fig. 2.1, the result of the growth scheme is a strained InAs island based on the wetting layer in a GaAs matrix. Figure 2.1(b) shows a transmission electron microscopy image of capped InAs QDs. In the Stransky-Krastanov mode, the size, shape and density of QDs can be controlled by regulating the deposition rate, temperature, etc.

2.2 InAs QD as a Single Photon Emitter

2.2.1 Discrete Energy State

Figure 2.2 illustrates the confinement potential of a self-assembled InAs QD. In lateral directions, the self-assembled InAs distribution varies rather smoothly. The InAs distribution abruptly changes along the growth direction with a strong confinement. The

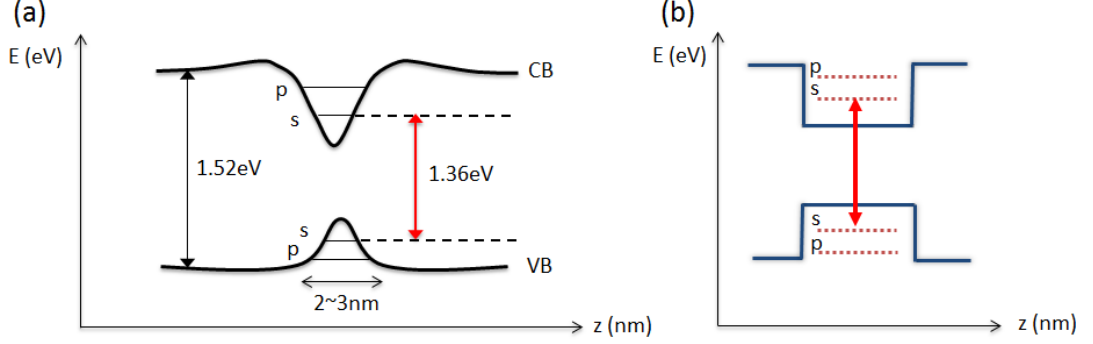


Figure 2.2: Potential profile of a self-assembled InAs quantum dot in the growth direction - (a) The reduced bandgap of InAs in a GaAs matrix provides a confinement potential for electrons in the conduction band (CB) and holes in the valence band (VB). A ladder of discrete energy levels in the quantum dot are labeled as s and p similar to the classification of atomic states owing to the symmetry of the manipulation. (b) The QD can be simply described by a square-well potential.

confinement potential energy in the growth direction results in a series of quantized energy levels. The potential landscape of the QD can be often simplified by a square-well potential in the growth z direction (49). The three dimensional confinement results in atom-like discrete energy states as follows. The three dimensional potential is described by

$$V(\mathbf{R}) = \begin{cases} \frac{1}{2}m^*\omega_0^2(x^2 + y^2) & \text{if } -|z| < L/2, \\ +\infty & \text{if } -|z| > L/2, \end{cases}$$

where L is the height of the QD, and ω_0 is the energy-level spacing. Hence the main level spacing is provided by the vertical confinement.

The potential well of the QD can trap electrons and holes at a ladder of discrete states. In general, the energy states of QDs can be found in the *Schrödinger* equation:

$$\left[-\frac{\hbar^2}{2m^*}\nabla^2 + V(\mathbf{r}) \right] \Psi(\mathbf{r}) = E\Psi(\mathbf{r}). \quad (2.1)$$

Here, m^* is the effective mass, $V(\mathbf{r})$ is the effective potential, E is the energy state, and Ψ is the wavefunction of an electron. Created bound states in the dot are then obtained from this *Schrödinger* equation by (50)

$$E = (n_x + n_y + 1)\hbar\omega_0 + \left(\frac{\pi^2\hbar^2}{2m^*L^2} \right) n_z^2. \quad (2.2)$$

Here, $n_{x,y} \geq 0$ and $n_z \geq 1$ are integers.

2. SELF-ASSEMBLED INAS QUANTUM DOTS

In analogy to the shell structure of atoms, the lowest bound state of confined carriers in the dot shows s-type standing-wavefunction symmetry (no orbital degeneracy). The atom-like confined level is referred as s-shell (51) and, in turn, the next confined level as p-shell.

2.2.2 QD Charging and Single Photon Emission

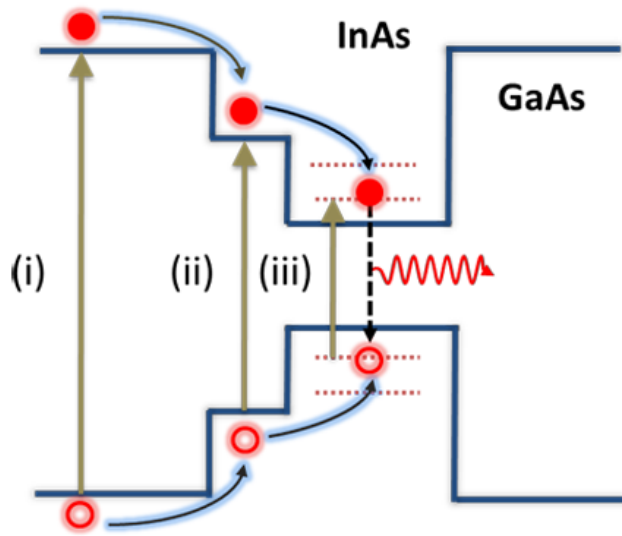


Figure 2.3: A schematics of the QD energy band diagram of the studied self-assembled InAs QD embedded in a GaAs matrix - Several optical excitations and recombination processes are simply depicted for an InAs QD in GaAs semiconductor. The figure illustrates the excitations (straight gray arrows) of (i) above BandGap (BG) of 1.52 eV, (ii) Wetting layer of 1.47 eV and (iii) p-shell of about 1.39 eV. After the relaxation of electron(closed red circle) and hole (open red circle) carriers, the radiative recombination of states in the s-shell is shown with the wavy red arrow in the band gap (1.35 eV).

We now consider ways to charge a single QD and its radiative cascade. The simplest way to excite InAs QDs is the above-bandgap pumping. In above-bandgap pumping, a laser excites above the GaAs bandgap of about 1.52 eV, as illustrated in Fig. 2.3(i). The above-bandgap excitation creates charges in a large volume of the GaAs matrix efficiently. In a random manner, a fraction of these charge carriers is firstly captured by the wetting layer. In fact, the carriers can be directly photo-created in the wetting layer (see, Fig. 2.3(ii)). Since the wetting layer is thin on the order of a few angstroms in the immediate vicinity of QDs, the wetting layer excitation prevents unwanted heatings of

the GaAs absorber and allow the exciting light to propagate in the photonic wire. The charge carriers then relax into QD energy levels by giving off phonons on a few 10 ps timescale (52, 53). During the relaxation process, the informations of spin and phase are lost. Once carriers reach to the lowest unoccupied states of QDs, they recombine by emitting a single photon after a characteristic lifetime of about 1 ns (54). The so-called “photoluminescence” of QD is a standard tool to study optical emission properties of a single QD. The details of the photoluminescence spectroscopy performed in this work are explained in later chapters.

Alternatively, InAs QDs can be excited by quasi-resonant or resonant pumping. In quasi-resonant excitation, the Photo-Luminescence Excitation (PLE) spectroscopy is performed by scanning the laser across p-shell states of a single QD. Since the laser is tuned to a higher excited state within a single QD, the excited state excitation deterministically creates an exciton for a given excited state. The absorption enhancement can also proceed through the longitudinal optical (LO) phonon above the QD fundamental transition. The technical details of this optical pumping are given in Chapter 3. In this way, the p-shell excitation can select a unique excited state of a single QD since many QDs have variable sizes, and thereby different energy spacings. Once a single QD is excited quasi-resonantly, Rabi oscillation is then expected to be observed between the empty-dot state and p-shell exciton state. For a π pulse, one could manipulate the p-shell exciton in the QD (55).

Strict resonant pumping also selectively excites a single QD by creating the “s-shell exciton” as illustrated in Fig. 2.3(iii). Under the s-shell optical excitation, the excitonic ground state is directly probed either by the photoluminescence or reflection spectroscopy. In photoluminescence measurements, it is rather difficult to resolve the radiative light from scattered laser lights under the resonant s-shell excitation.

To achieve highly efficient and purified single photon emission, there is a trade-off between these pumping techniques. First, the non-resonant excitation scheme, despite its efficient charging, has several drawbacks in single photon device based QDs in a nanophotonic structures. Since a bulky host material embedding QDs are also excited with random defects, the potential landscape can fluctuate in the vicinity of the QD. Subsequent QD emission instability is unavoidable. Furthermore, the carrier capturing process via phonon.

2. SELF-ASSEMBLED INAS QUANTUM DOTS

On the other hand, (quasi-) resonant excitation directly generate an exciton inside the QD by getting off above disadvantages. From the viewpoint of the adsorption cross-section, the resonant excitation, however, needs much intense light to excite a single QD and probe to separate exciting laser light from the emission.

2.2.3 Complex Excitonic States

So far it has been stated only a single exciton state consisting of an electron and hole pair. In general, a number of carriers captured inside the QD results in complex excitonic states. A few of simplest series of energy states of a QD is schematically shown in Fig. 2.4. Fortunately, each complex excitonic state emits at a slightly different energy and its emission can be spectrally filtered (17, 56). When a carrier is captured inside a neutral QD, the Coulomb interaction plays a crucial role. The “charging energy” is about 25 meV (57). When more than an electron-hole pair are created in the dot, the Coulomb interaction, however, fails to estimate the magnitude of the exciton charging energy. Note that not only the Coulomb energy but also a net attractive interaction between two excitons has to be considered. The binding energy of namely “bi-exciton” then can induce a splitting whose emission energy varies the exciton energy by few meV or even few tens of meV (56). In a case of a charged-dot initially containing a single charge, the interaction with a resident charge has to be considered for the optical generation of exciton, as the spectral emission line shifts from the neutral exciton (58, 59). In this way, single QD can produce a single photon source at different emission energies.

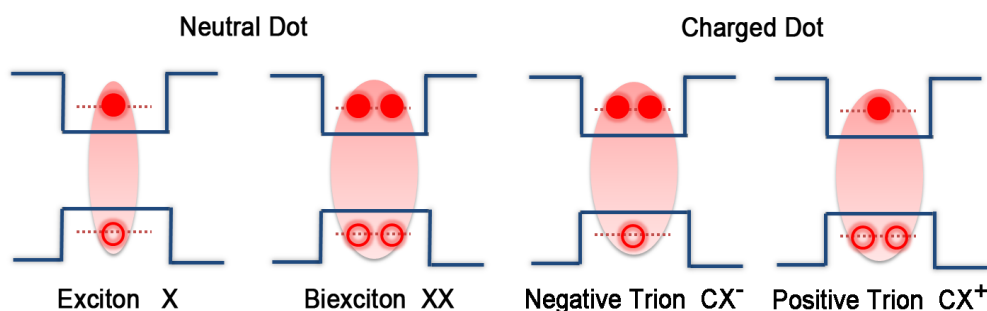


Figure 2.4: Schematic multiparticle states of a single QD - Simplified configurations of the conduction and valence bands are depicted for neutral and charged QDs after optical excitations.

2.3 Interaction of QD with Light in a Photonic Wire

As described in the previous sections, QD is indeed an attractive choice for a single photon emitter. Unfortunately, embedded InAs QDs for example in a three-dimensional host GaAs matrix lose most of the emission about 99% at the semiconductor-air interface (38). Then, extracting a large fraction of the light emitted by an embedded QD is an important issue when designing a single photon source. To enhance the collection efficiency, several nanophotonic structures embedded QDs have been used, like a micropillar (31), photonic crystal (20, 36, 60), or photonic wire (38). With these techniques, these devices are tailored to couple efficiently the QD photoluminescence to a fundamental optical mode. One successful approach of the micropillar structure has offered an effective coupling of a single photon emitter to a localized mode of cavity with a high quality factor (31). Extraction efficiency of 38% with a rate of up to 31 MHz (31) has been demonstrated with a highly selective photon emission within a narrow bandwidth of a few tenth of a nanometer. Despite this high frequency selectivity of emitted photons, subsequent reduction of the collection efficiency is a limitation of micropillar cavities for a single photon device. Another drawback of this approach is the narrow bandwidth emission determined by the high cavity quality factor.

Very recently, an embedded quantum dot in a photonic wire, studied in this thesis, has been fabricated to overcome these limitations (38). Photonic wires are structures with a radius of the order of 100 nm and a much larger length scale in microns. In view of a nanometer scale radius, GaAs photonic wires studied in this work are classified as a one-dimensional waveguide where the light propagates only in one dimension. The GaAs waveguides made of a high refractive index of 3.45, offer a strong lateral confinement of the guided mode simultaneously screening the coupling into the leaky modes. In this sense, embedded InAs QDs in a GaAs photonic wire can effectively interact with a single spatial mode of the photonic wire. Noting that each QD recombines at a different energy, many different QDs will be coupled to the guided mode of the photonic wire. This advantage makes the GaAs photonic waveguide fundamentally different from the cavity system. A GaAs wire studied in this work has been proved to its efficient QD emission control over a broad wavelength range (A large fraction (90%) of spontaneous emission over a bandwidth exceeding 70 nm at $\lambda = 950$ nm)(38). As another advantage of the GaAs waveguide, almost perfect radiation yield can be achieved

2. SELF-ASSEMBLED INAS QUANTUM DOTS

in its far-field emission if properly designed. By tailoring the wire end properly, the far-field outcoupling efficiency of the guided photons can reach unity (61).

2.3.1 QD Decay in the Bulk

This section describes the spontaneous emission of QDs in a bulk homogeneous medium. QDs can be prepared in the excited state and then decay to the ground state by emitting photons. The radiative process is spontaneous emission by which an electron in an excited state relaxes to the lower level. Noting that InAs QDs, studied in this thesis, are on the order of ten times smaller than the emission wavelength, the QD can be approximated by a two-level system. The ground and excited states of a two-level system are denoted by $|g\rangle$ and $|e\rangle$ respectively.

The following Hamiltonian describes the interaction between a QD and the free radiation field in the dipole approximation (62):

$$\mathbf{H}_{\text{Int}} = -\boldsymbol{\mu} \cdot \mathbf{E} \quad (2.3)$$

with the electric dipole moment of the transition $\mu_{ij} = e \langle i | \mathbf{r} | j \rangle$ and the electric field \mathbf{E} .

Applying the rotating-wave approximation, the total energy of the system can be given by the Hamiltonian of

$$\begin{aligned} \mathbf{H}_{\text{Tot}} &= \mathbf{H}_{\text{QD}} + \mathbf{H}_{\text{Env}} + \mathbf{H}_{\text{Int}} \\ &= \hbar\omega_{ab}|a\rangle\langle a| + \sum_{\mathbf{k},\epsilon} \hbar\omega_{\mathbf{k}} a_{\mathbf{k},\epsilon}^\dagger a_{\mathbf{k},\epsilon} \\ &\quad + \hbar \sum_{\mathbf{k},\epsilon} \left(g_{\mathbf{k},\epsilon}^* |a\rangle\langle b| a_{\mathbf{k},\epsilon} + g_{\mathbf{k},\epsilon} a_{\mathbf{k},\epsilon}^\dagger |b\rangle\langle a| \right). \end{aligned} \quad (2.4)$$

Here, $|a(b)\rangle$ corresponds to the QD level with the transition energy $\hbar\omega_{ab}$ of two-level atom, and $a_{\mathbf{k},\epsilon}$ are photon annihilation operators for wavevector \mathbf{k} and polarization ϵ . The atom-photon coupling coefficients $g_{\mathbf{k},\epsilon}$ are given by (62)

$$g_{ij,\mathbf{k},\epsilon} = \left(\frac{\omega_{\mathbf{k}}}{2\epsilon_0 \hbar L^3} \right)^{1/2} \boldsymbol{\epsilon} \cdot \boldsymbol{\mu}_{ij}. \quad (2.5)$$

If a QD state is initially prepared in the excited level at time $t = 0$, the quantum state for a finite time $t > 0$ can be written by

$$|\Psi(t)\rangle = c_e(t)|e, 0\rangle + \sum_{\mathbf{k},\epsilon} c_{g,\mathbf{k},\epsilon} |g, 1_{\mathbf{k}}\rangle, \quad (2.6)$$

2.3 Interaction of QD with Light in a Photonic Wire

where \mathbf{k} is all available optical modes. In the Wigner-Weisskopf approximation, solving the *Schrödinger* equation (2.5) by inserting this state results in a set of the complex coefficients of (62)

$$\begin{aligned} c_e(t) &= e^{-(\Gamma/2+i\omega_{ab})t}, \\ c_{g,\mathbf{k},\epsilon} &= g_{\mathbf{k},\epsilon} \frac{e^{-i\omega_{\mathbf{k}}t} - e^{-(\Gamma/2+i\omega_{ab})t}}{(\omega_{\mathbf{k}} - \omega_{ab}) + i\Gamma/2}. \end{aligned} \quad (2.7)$$

Here, the radiation field $\omega_{\mathbf{k}}$ is assumed to vary little around the photon mode of ω_0 . Resulting dipole decay rate Γ in a bulk homogeneous medium is found by

$$\Gamma = \frac{n\omega^3|\mu|^2}{3\pi\epsilon_0\hbar c^3}, \quad (2.8)$$

where n , ϵ_0 and c are, respectively, the refractive index, the electric permittivity and the speed of light in vacuum.

2.3.2 QD Decay in a Photonic Wire

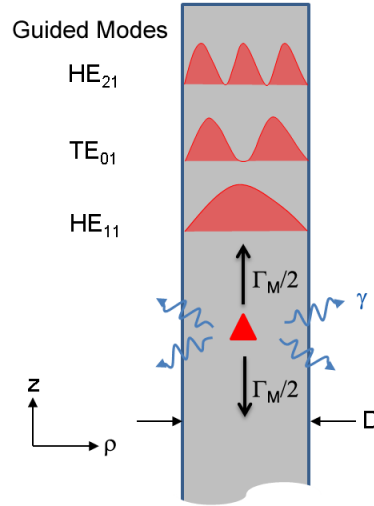


Figure 2.5: Schematic guided mode of a photonic nanowire embedding a QD - Various optical modes are present that are guided by the photonic wire with diameter D . Leaky modes are also illustrated in which QD (red triangle) emits light with a rate of γ .

Given spontaneous emission rate Γ from a QD in the bulk, the next question would be how to extract a large fraction of its spontaneous emission into a fundamental

2. SELF-ASSEMBLED INAS QUANTUM DOTS

optical mode. A strategy here is to insert a QD in a properly designed one-dimensional photonic waveguide. As shown in Fig. 2.5, several guided channels can exist depending on a nanowire diameter D . In addition, a coupling into the unguided modes (γ) also appears. However, further optimization of the diameter within $0.18\lambda < D < 0.23\lambda$ has demonstrated the excellent spontaneous emission coupling into the fundamental guided mode (38). Since the well-designed photonic wire allows the light guiding via one-dimensional channel, an embedding QD in the one-dimensional path of light ideally provides 100% extraction efficiency. Here, the extraction efficiency is defined as a fraction of collected photons with respect to spontaneously emitted photons from the QD. Up to now, an extraction efficiency of 72% (38) has been achieved in this QD-photonic waveguide with the multiphoton emission of less than 1%.

2.3.2.1 Modified Spontaneous Emission Rate

For an dipole emitter located in the center of wire and aligned perpendicular to the wire axis, the spontaneous emission decay rate Γ_M into the one-dimensional guided mode M is given by

$$\Gamma_M = \frac{\omega |\mu|^2}{\hbar \epsilon_0 n^2 S_{eff} v_g}, \quad (2.9)$$

where ω is the frequency of the emitter, v_g is the group velocity, and S_{eff} is the effective surface area of the mode.

The fraction β of spontaneous emission funneled into a well-guided localized optical mode of M can be expressed, in terms of the spontaneous emission rate into the HE₁₁ mode Γ_M , as

$$\beta = \frac{\text{Spontaneous emission rate into a guided mode}}{\text{Total spontaneous emission rate}} \quad (2.10)$$

$$= \frac{\Gamma_M}{\Gamma_M + \gamma}. \quad (2.11)$$

Here, γ is the spontaneous emission rate into all the other unwanted modes. A high β therefore means the inhibition of all unwanted modes ($\Gamma_M \gg \gamma$). GaAs photonic nanowire, studied in this thesis, has a benefit of about 0.9 β -factor by suppressing the γ of Eq.(2.11) down to a few percent due to the large GaAs-air index contrast (38).

Now, one can also derive the ‘‘generalized Purcell factor’’, which is a key parameter for the optimization of an effective atom-cavity coupling. The generalized Purcell factor

2.3 Interaction of QD with Light in a Photonic Wire

$F_M = \Gamma_M/\Gamma$ can be derived as

$$F_M = \frac{3}{4\pi} \frac{(\lambda/n)^2 n_g}{S_{eff} n} \quad (2.12)$$

to the case of the embedded emitters in the nanowire. The generalized Purcell factor $F_M = \Gamma_M/\Gamma$ represents the factor of the density of photon states in an one-dimensional photonic wire. As shown in Eq.2.12, the Purcell factor solely relies on the waveguide properties. Anticipating a small S_{eff} and large n_g in a photonic waveguide, the efficient funneling of photons (a large Purcell factor) is indeed achievable. In fact, the generalized Purcell factor indicates the inhibition of γ instead of the enhancement of Γ_M . It was shown in Ref. (63) that the emission rate 0.045 /ns of off-axis QD was 16 times slower than that of an on-axis QD embedded in a GaAs photonic wire. As the emitter is close to the surface of the photonic wire, the light coupling to the guided mode is dramatically reduced but γ is still inhibited.

2.3.3 Global Efficiency

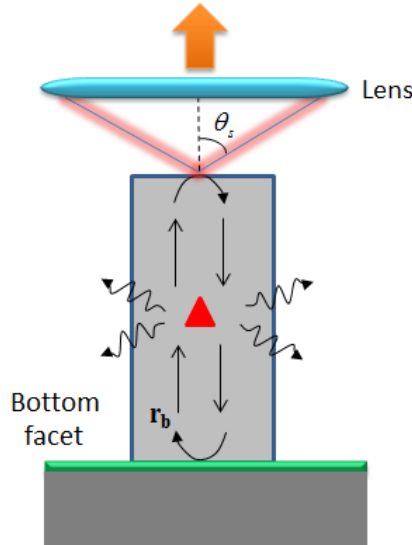


Figure 2.6: Photon emission in a one-dimensional waveguide - Sketch of a photonic wire containing a QD dipole source (red triangle) and the upward- and backward-propagating HE_{11} guided modes. r_b is the reflection coefficient of the HE_{11} mode at the bottom.

Although the efficient coupling (high β -factor) is achieved, the emitted light must be efficiently extracted to the free space mode. The extraction efficiency η is defined as

2. SELF-ASSEMBLED INAS QUANTUM DOTS

the probability to collect the emitted photons above the top facet within a solid angle $2\pi[1 - \cos(\theta_s)]$, as illustrated in Fig. 2.6(a). The extraction efficiency η is then given by

$$\eta(\theta_s) = T(\theta_s) \frac{\beta(1 + |r_b|)^2}{2(1 + \beta|r_b|)}, \quad (2.13)$$

where $T(\theta_s)$ is the fraction of the emitted photons carried into the upward HE_{11} mode that are scattered into a cone defined by the angle θ at the top facet. Here, r_b is the reflection of the fundamental mode on the bottom facet.

The extraction efficiency can reach up to

$$\eta_{max} = \frac{2\beta}{\beta + 1} \quad (2.14)$$

with a high reflective photonic wire ($r_b \sim 1$) and with a perfect transmission $T(\theta_s) \sim 1$. As mentioned in Section 2.3.4, our geometry ensures a large β -factor which exceeds 90% for a QD embedded in a GaAs photonic wire with a diameter of $D \sim 0.22\lambda$. r_b can easily reach unity by putting a high-reflectivity mirror at the bottom. Now remaining parameter is the transmitted intensity $T(\theta_s)$ through the top facet. As we will show in the next section, a proper tapering can increase $T(\theta_s)$ for efficient collection of light with standard objectives. Two possibilities are the conical top tapering and inverted taper photonic wires.

Let's first discuss a conical top tapering in which diameter gradually decreases with the height. The wire geometry is illustrated in Fig. 2.7. For a photonic wire with a conical top taper, the adiabatic reduction of the top diameter decreases the effective refractive index, thereby completely deconfining the guided mode at the top. In such way, the conical tapering strongly reduces the back-scattering at the top facet and the beam divergence in air. Hence almost perfect transmission can be achieved ($T(\theta_s) \sim 1$) with the directive far-field emission. Photonic wire with a tapering angle of around $\alpha = 5^\circ$ and a gold bottom mirror, a large transmission through the top allows an outcoupling efficiency of 72% (38).

Second possibility to improve the extraction efficiency is inverted taper photonic wires. This time, the diameter of the wire adiabatically increases from the bottom to the top. As the conical taper does, adiabatic lateral deconfinement of the guided mode yields almost perfect far-field radiation. A figure of merit of the trumpet-like wire is the gradual increase of the mode area as well as the effective mode index with the height.

Then we can put single two-level emitters where the light is optimally confined in the fundamental guided mode, as illustrated in Fig. 2.7(b).

2.3.4 Sample Summary

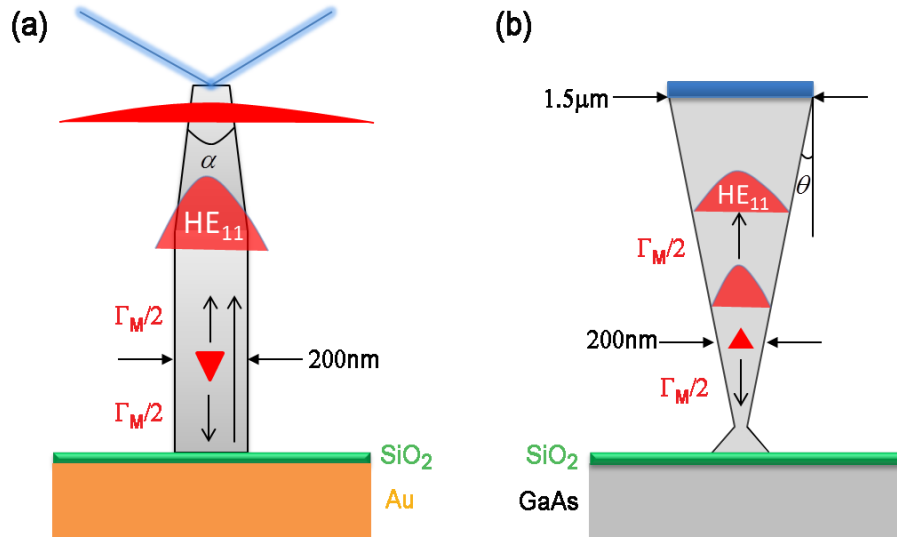


Figure 2.7: Schematic diagram of two photonic nanowires embedding a single QD - Schemes of the photon emission in (a) a needle-type GaAs photonic nanowire and (b) an trumpet-like GaAs photonic nanowire. An InAs QD is presented with a red triangle.

A detailed description of the fabrication technique (64) is outside the scope of this thesis. In this section, only brief view of two photonic devices will be given. The optical measurements investigated in this thesis were performed with two types of GaAs photonic nanowires embedding self-assembled InAs QDs. As illustrated in Fig. 2.7, two vertical photonic nanowires were fabricated as efficient single-photon devices. Both wires are made of a GaAs with a high refractive index of 3.45. In the two designs, the GaAs photonic wires offer a strong lateral confinement of the guided mode at the level of QDs with an optimum diameter of about 200 nm. For the optimization of the far-field outcoupling efficiency, a regular tapering is tailored for the first single photon device. As another strategy, overall structure of the second GaAs wire act as an inverted taper by adiabatically varying the diameter from 200 nm to 1.5 μm for an etching angle of $\theta = 2.1^\circ$. Therefore, this trumpet-like wire features a superior control of the far-field radiation. For both GaAs photonic devices, an efficient spontaneous emission control is

2. SELF-ASSEMBLED INAS QUANTUM DOTS

achieved over a broad wavelength range ($\beta \geq 90\%$ over a bandwidth exceeding 100 nm at $\lambda = 950$ nm)(61, 63). Two single photon devices fabricated in this sense are described below.

2.3.4.1 Cylindrical Photonic Wire: Champion



Figure 2.8: Tapered cylindrical photonic wire - Scanning electron micrography of a tapered GaAs photonic nanowire containing few InAs QDs. An InAs QD is presented with a red triangle.

A planar structure was grown by molecular beam epitaxy. A single layer of self-assembled Stranski-Krastanov InAs QDs were buried inside the GaAs matrix. Tapered photonic wires are defined by a top-down approach. An electron-beam lithography and several dry etching techniques (Ar – SiCl₄ plasma) are used to optimize the size and the shape of the photonic wires. The GaAs wire is 2.5 μm height embedding InAs QDs 80 nm above the highly reflective gold mirror ($|r|^2 > 91\%$) at the bottom, as illustrated in Fig. 2.8. A few of InAs QDs are located 80 nm above this mirror. A strong confinement of the fundamental guided mode HE_{11} was achieved by optimizing the diameter of about 200 nm at the level of the QDs. The diameter of about $200\text{nm} \sim \lambda/2n$ at the level of the QDs leads the emitted photon to effectively couple to the fundamental guided mode HE_{11} with high efficiency $\beta \sim 90\%$ by screening other unwanted modes. In order to optimize the collection of the far-field emission, an integrated modal mirror

2.3 Interaction of QD with Light in a Photonic Wire

(gold and SiO₂ spacer) is prepared at the bottom via a flip-chip technique. Here, a gold mirror redirects the downward emitted photons since half of the emitted photons ($\beta/2$) directs towards the substrate. A SiO₂ spacer layer of 11 nm thickness was introduced between the wire and gold mirror to avoid the plasmonic effects and absorption losses. A smooth tapering of the wire tip is tailored with an opening angle, $\alpha \sim 5^\circ$. The tapered structure provides the adiabatic conversion of the HE_{11} mode into a strongly deconfined mode, thereby the large coupling to the free space mode.

2.3.4.2 Conical Photonic Wire: Trumpet

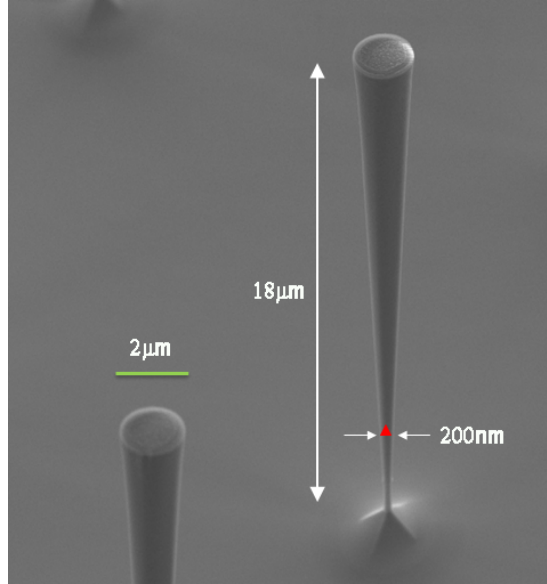


Figure 2.9: Geometry of the conical photonic wire - (a) Conical shape of a GaAs photonic wire embedding InAs QD (red triangle) are schematically shown. (b) Scanning electron microscopy image of a GaAs photonic wire defined by e-beam lithography and reactive ion etching.

The device fabrication starts from a planar structure grown by molecular beam epitaxy on a GaAs wafer. A single layer of InAs self-assembled QDs (areal density $300 \mu\text{m}^{-2}$) is located in a GaAs matrix (residual positive doping $p = 10^{16} \text{ cm}^{-3}$). The ensemble luminescence peaks at 920 nm (50 nm inhomogeneous broadening). Photonic wires are defined with a top-down approach, using e-beam lithography and dry plasma etching (Ar – SiCl₄ plasma). A careful control of the etching leads to a conical wire geometry to control the optical mode transverse profile along the wire, as shown in

2. SELF-ASSEMBLED INAS QUANTUM DOTS

Fig. 2.9. The adiabatic conversion of the guided mode HE_{11} along the wire into a mode of diameter $\sim 1.5 \mu\text{m}$ can then be collected efficiently with an objective of numerical aperture $NA=0.75$. A series of the photonic wires with top diameters varying by a fine 10 nm step were fabricated. The actual wire diameter at the dot location d_{QD} is measured with a ~ 10 nm accuracy by scanning electron microscopy.

2.4 Chapter Summary

A general overview of properties and applications of self-assembled InAs QDs embedded in a GaAs photonic wire was given. QD charging and its spontaneous emission were theoretically discussed, respectively in GaAs bulk and one-dimensional photonic wire. Two types of wire structures were then discussed with an emphasis on different tapering structures. Their basic optical properties will be given in the following Chapters.

3

Optical Spectroscopy of a Single InAs QD in a GaAs photonic wire

Our principle tool for investigating the emission from a single self-assembled QD based single-photon sources is photoluminescence. As described in previous Chapter 2, it is shown how the QD recombination process occurs with nonresonant excitation. In order to measure the photoluminescence of a single QD, the luminescence is sent through a spectrometer to spectrally isolate a single QD. The sample also needs to be mounted in the cryostat and should be cooled to low temperature 4K. The setup requires a high collection in the microscope objective and, high detection efficiencies.

In this Chapter, the high resolution experimental setup is presented for single self-assembled QD studies, addressing the above requirement. Experimental results are then discussed for the characterization of a single InAs QD based GaAs photonic wire. Single InAs QDs is first characterized with photoluminescence signals whose charge states are identified by the power dependence. With a Ti:Sa Continuous Wave (CW) optical source, photoluminescence excitation spectroscopy is then performed to characterize the excited states of a single InAs QD and to excite QD states selectively. The selective excitation can further be utilized to investigate two-level properties. Temperature-dependent photoluminescence studies, however, tell us the environment effect that might perturb the QD stability.

3. OPTICAL SPECTROSCOPY OF A SINGLE INAS QD IN A GAAS PHOTONIC WIRE

3.1 Experimental Setup

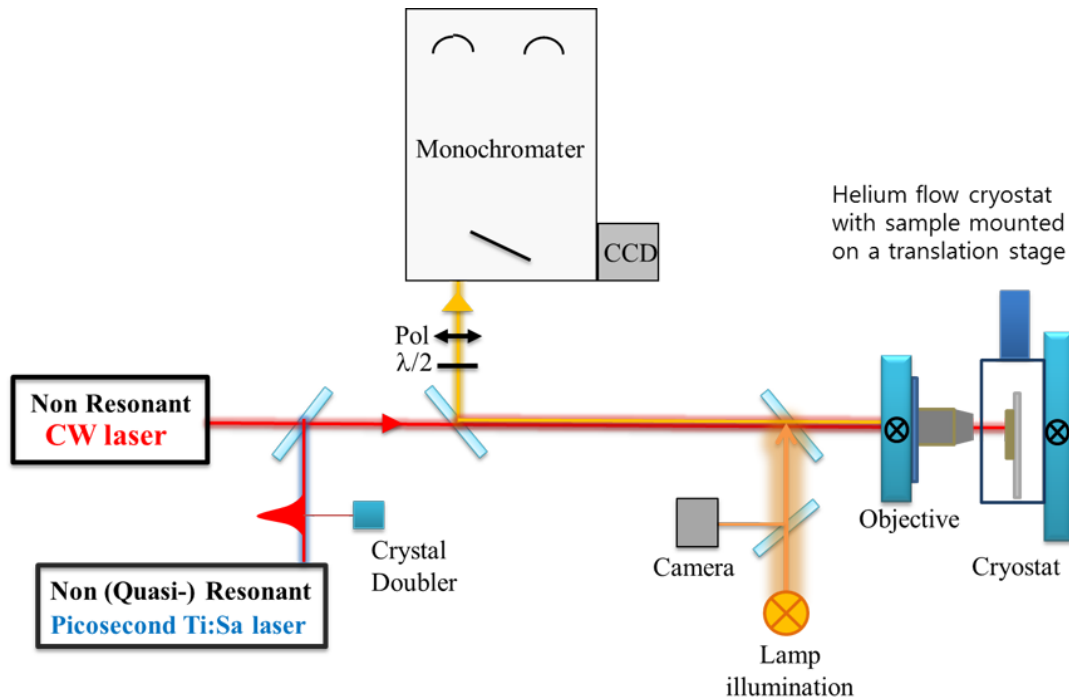


Figure 3.1: Schematic diagram of photoluminescence measurement setup - More details are described in the text. The laser light is sent to the cryogenic confocal microscope. The microscope focuses the light on an emitter and subsequently recollects the emitted light. The light is guided into a spectrometer and then detected either by a Peltier-cooled Si-CCD camera or Avalanche Photodiode (APD).

Figure 3.1 shows the experimental setup used for photoluminescence experiment presented in this thesis. The sample is located in a He-flow cryostat which is mounted on a translation stage. Standard laser diodes or CW Ti:Sa laser are used to excite the sample either off-resonantly or quasi-resonantly. The light is sent to the sample and focused by a high NA microscope objective. Two objectives are used NA=0.4 and NA=0.75. A high precision piezo-electric positioning system is used to fine-tune the objective, together with the coarse translation stage. With the help of an imaging camera, the movable objective allows us to bring emitters into the laser focus. The light emitted by the recombination of the QD is recollects by the same objective, and directed to a 1.5 m focal length spectrometer ($12 \mu\text{eV}$ spectral resolution at 930 nm). Half wave plate $\lambda/2$ and polarizer are used to rotate the polarization along the

best polarization of the spectrometer grating (1200 *grooves/mm*). The light is then detected with a Peltier-cooled Si-CCD (Charge Coupled Device) camera. The camera pixel size (20 μm) corresponds to an energy step comparable to the resolution. This photoluminescence setup thus enables high resolution photoluminescence spectroscopy on a single QDs, as well as studies simultaneously employing narrow bandwidth optical fields. We now discuss the details of this setup.

3.1.1 Optical Source

3.1.1.1 Non Resonant Excitation

A continuous-wave (CW) diode laser and a Tsunami titanium-Sapphire laser can both be used as the non-resonant optical pumping source. At first, the CW optical excitation is provided by a 825 nm continuous-wave diode laser whose intensity and temperature are controlled by Thorlabs ITC 502. The excitation wavelength corresponds to the energy slightly below the GaAs band gap so that the light can be guided without absorption losses, and creates excitons in the QD wetting layer. The detailed band structure was already shown in Fig.2.3 in Chapter2. In the usual mode of operation, the output power is 60mW. The excitation power is further adjusted with a couple of polarizers and a set of neutral optical density filters.

The pulsed optical source is a Tsunami titanium-Sapphire (Ti:Sa) laser manufactured by Spectraphysics operating between 650~980 nm. The Tsunami Ti:Sa laser is also capable of switching between picosecond or CW mode operation. To utilize Ti:Sa laser in this wavelength range, a YAG doubled laser (Millennia Xs J) emitting at 532 nm pumps the Tsunami with a maximum output power of 10 W. The maximum power of 1.5 W is then obtained at the output of the Tsunami at 825 nm. The wavelength is tuned by using a Lyot birefringent filter placed inside the laser.

3.1.1.2 Quasi Resonant and Resonant Excitations

In our system, the InAs quantum dots embedded in GaAs photonic wire emits light typically in a 900~950 nm wavelength range. Since the Ti:Sa laser spans the energy range of 825~900 nm below the GaAs bandgap, excited states of QD can be studied by monitoring the QD emission of ground state. We also have a Toptica DL pro 940 laser for quasi-resonant or resonant excitation spectroscopy. The DL pro 940 is a continuous

3. OPTICAL SPECTROSCOPY OF A SINGLE INAS QD IN A GAAS PHOTONIC WIRE

frequency tunable external cavity laser between 910 ~ 985 nm, delivering a maximum powers up to 100 mW. The DL pro 940 is capable of a mode-hop free laser tuning up to 50 GHz. The principle of a DL pro diode is to combine highly stable external cavity to select a specific wavelength so as to dramatically enhance the finesse of the entire system. The linewidth of laser then reaches down to 100 kHz against that of 100 MHz in a conventional diode.

3.1.2 Cryogenics

In order to study the optical properties of the emitters such as QDs, the cryogenic temperature is required. In our experiment, the sample is kept at liquid helium temperatures around 4.5 K. The sample is positioned inside a Oxford Instruments Company continuous Helium flow optical cryostat. The cryostat itself was mounted on a 2-axis translation stage for horizontal and vertical adjustment of the sample position. Liquid helium is delivered from a vessel via transfer tube, to a heat exchanger located near the substrate of the sample; The gas produced then exits to a recovery line. The cryostat temperature can also be tuned from 3.5 K to 80 K with 0.1 K step with a heater driven by the temperature controller ITC 601. The thermal dilatation is low at the level of less than 100 nm/K, which permit to maintain a good alignment for variations in temperature.

The optical access is through a vacuum window whose circular diameter is 10 mm and the thickness is 0.4 mm. The objective should be positioned at a working distance of a few mm from the surface of the sample depending on the choice of a focal length and its opening numerical aperture. The two objectives we have used have a numerical aperture NA of 0.4 and 0.75. The larger opening angle of an objective allows to gather more light from the sample and to have a higher resolution of the image. In photoluminescence measurements presented in the thesis, both objectives of 0.4 NA Olympus LMPL and 0.75 NA ZEISS LD Plan-NEOFLUAR objective are used of which the working distances are respectively 8.1 mm and 2.2 mm, resulting 20 and 63 magnifications. The objective is mounted on the Thorlabs three-axis piezo electric positioning system so to achieve a precision positioning of 20 nm. The sample and cryostat are as well mounted on a coarse two axis positioning stack which allows a positioning of the sample with respect to the objective.

3.1.3 Spectrometer

The emitted photons from the sample are recollected with the same objective and guided to a grating spectrometer that disperses the light. We can then detect a spectrally resolved light on a Peltier-cooled charge-coupled device (CCD), or study their time-resolved dynamics by means of an avalanche photodiode (APD). We use a Jobin-Yvon THR1500 spectrometer possessing a 1.5 m monochromator. The monochromator has a grating with 1200 grooves/mm, blazed at 750 nm, which gives a spectral resolution of about 0.0088 nm at 930 nm. The grating is controlled by computer via a GPIB interface, which position is rotated leading to a high precision of $\delta\lambda = 0.001$ nm by a motor. The spectral resolution can be checked with a resolution limited emission source, in our case, the DL Pro Toptica laser. At very low power, the characteristic width of 12 μ eV is extracted by fitting with a Lorentzian function and is taken as the resolution of our spectrometer.

3.1.3.1 CCD

The detector used with the THR1500 is a Pixis 100 Peltier-cooled CCD camera of Princeton Instruments with a CCD chip consisting of a 1340×100 grid of $20 \mu\text{m} \times 20 \mu\text{m}$ pixels. The CCD camera acquires a spectral information, within a spectral window of about 10 nm window selected by the grating, with the quantum efficiency of about 25% in the near infrared region (~ 900 nm).

3.2 QD Characterization with photoluminescence Spectroscopy

This section presents photoluminescence spectroscopic measurements on single self-assembled InAs QD embedded in a "tapered photonic wire" at 4.5 K. Figure 3.2(a) shows power-dependent photoluminescence characteristics of a single QD embedded in a needle-type photonic wire under nonresonant CW excitation (825 nm). In Fig. 3.2(a), there are three lines labeled X , XX and X^* in the spectral range between 1.361 \sim 1.349 eV. In the weak-excitation regime, a single broad excitonic line (X) is prominent, while others spring up on the high-energy side for higher power. These peaks correspond to the various states of a single QD in the lowest-energy configuration.

3. OPTICAL SPECTROSCOPY OF A SINGLE INAS QD IN A GAAS PHOTONIC WIRE

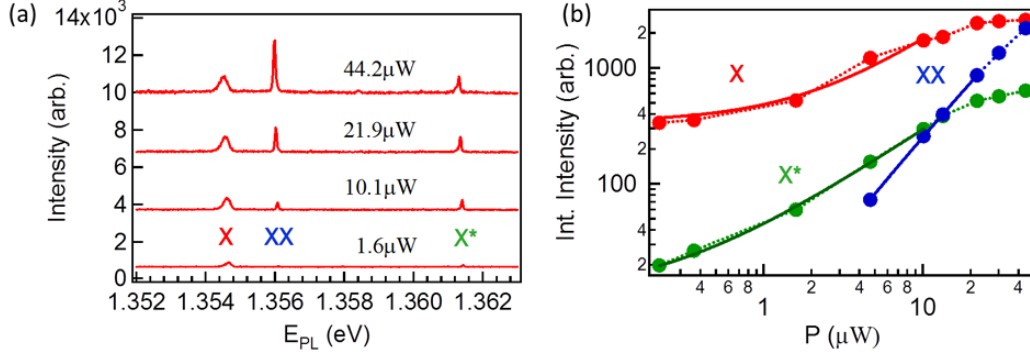


Figure 3.2: Power-dependent photoluminescence spectra on a single QD embedded in the GaAs photonic wire taken at $T=4.5$ K - (a) μ -photoluminescence spectra of the photonic wire as a function of the optical excitation intensity P under CW excitation at 825 nm. The photoluminescence spectra were obtained for the detection at E_{PL} with 0.1 s integration. In a single QD spectra, three emission lines are marked as X , XX , and X^* . (b) The integrated intensity of X , XX , and X^* as a function of P under CW and the wetting layer excitation. The solid line shows a fitting with a power law data. Fitted curves of X , XX , and X^* scale like $\sim P_X$, $\sim P_{XX}^{1.5}$, and $\sim P_{X^*}^{0.9}$ respectively.

A way of identifying these lines is to check the evolution of the emission pattern versus the excitation power. Figure 3.2(b) shows their respective integrated intensities under pulsed excitation, as the excitation power is increased from 220 nW to 44 μ W. In the power dependence measurement, a single excitonic emission X follows a linear dependence and saturates at high power where the average occupancy of excitons is one in the s-shell. While other lines, XX and X^* appearing at higher power have respectively a quadratic and linear dependence of their intensities with the excitation power. Integrated intensities of X and XX are seen to saturate as well at high excitation powers. These peaks X , XX , and X^* are then ascribed to neutral exciton, biexciton and charged exciton of a single QD, respectively.

This identification of X and XX is supported qualitatively by a simple model for the CW excitation. Let's consider a neutral QD which captures the electron-hole pairs, and imagine that electron-hole pairs recombine independently in the presence of other charges. Then, the probability P of finding n electron-hole pairs in the QD follows a Poisson distribution, which is expressed in terms of power p

$$P(n) = \frac{p^n e^{-p}}{n!}. \quad (3.1)$$

3.2 QD Characterization with photoluminescence Spectroscopy

In the weak excitation regime where photons are emitted at exciton energy in the dot, the intensity of the emission due to the exciton recombination is proportional to the probability of having one or more exciton in the dot:

$$I(n) \propto n_1 = 1 - P(0) = 1 - e^{-p} \sim p. \quad (3.2)$$

In the same sense, if two or more excitons are generated, the intensity of the emission due to the biexciton recombination is given by

$$I(n) \propto n_2 = 1 - P(0) - P(1) \sim p^2. \quad (3.3)$$

Therefore, the linear and quadratic pump-power dependences of X and XX identify these lines as emissions from one-exciton and biexciton that are very likely to be in the same QD. However, this simple model has a drawback for describing the charged states of the QD. At high power, the spectrum shows more complicated behavior with the appearance of the additional line X^* . As shown in Fig.3.2(b), X^* presents a linear dependence of its intensities with the excitation power, which is likely related to charged state.

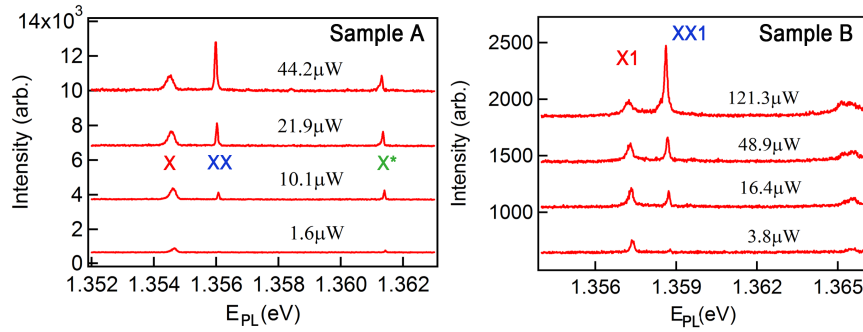


Figure 3.3: Excitation intensity dependence of photoluminescence spectra from different photonic wires - Individual QD photoluminescence spectra is plotted as a function of the optical pump power P for sample A and B at $T=4.5\text{K}$ under CW wetting layer excitation.

Here, the peculiar point to be noticed is a much broader linewidth of X with respect to that of XX . An obvious question is then why such different linewidth is observed in this exciton family of a single QD. Similar broadening pattern is also observed from different photonic wires in our sample. Figure 3.3 presents the power dependences of single QD emission lines performed on two different photonic nanowires. Note that

3. OPTICAL SPECTROSCOPY OF A SINGLE INAS QD IN A GAAS PHOTONIC WIRE

each emission line is fitted by a Lorentzian function on top of a background and its full width at half maximum (FWHM) is extracted.

The extracted power-dependent linewidth of a single QD from different photonic wires is then presented in Fig.3.4. The Lorentzian fit to the exciton and biexciton emissions of the needle-shape wire yields $\gamma_X = 250\mu\text{eV}$ and $\gamma_{XX} = 65\mu\text{eV}$ at $P = 20\mu\text{W}$. The exciton linewidth γ_X is thus almost triple the one of the biexciton ($\gamma_X \sim 3\gamma_{XX}$). Here, a triangle toward the right axis directly gives the corresponding ratio between the exciton and biexciton in Fig.3.4. The ratio of γ_X and γ_{XX} is found to be similar to that of γ_{X1} and γ_{XX1} of the sample B. Strikingly, the exciton lines show similar tripled FWHMs of XX (check, $R_{X/XX}$, $R_{X1/XX1}$).

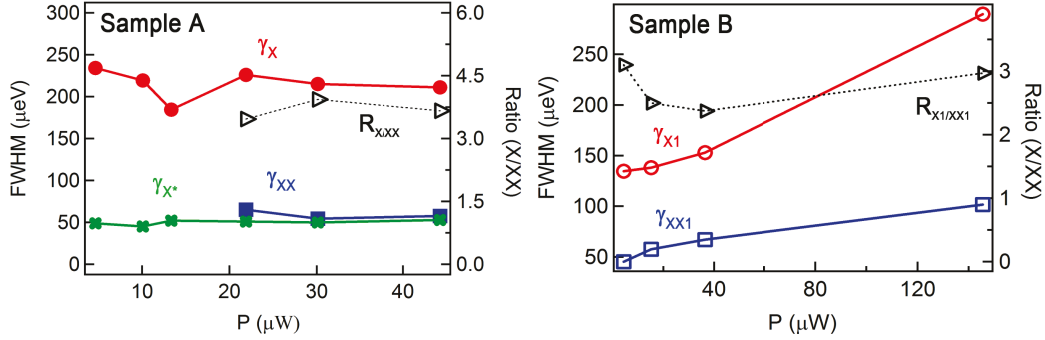


Figure 3.4: Power dependence of the photoluminescence linewidths from different photonic wires - The extracted linewidths of $\gamma_{X(X1)}$ (red circles), $\gamma_{XX(XX1)}$ (blue rectangle), and γ_{X^*} (green cross) are given with respect to the excitation intensity. A triangle toward the right axis shows the ratio ($R_{X/XX}$, $R_{X1/XX1}$) between FWHMs of exciton and biexciton of the investigated QD.

The significantly different linewidth between X and XX is in contrast with a typical behavior from the same dot (65). From the observation, one may doubt the previous identification of the exciton family followed by the excitation power dependence. If X and XX are indeed the exciton and biexciton, the different broadening has to be clarified. One likely possibility is that the wave function of exciton can be more sensitive to the environment of the QD than those of complex other states (66, 67). Whether the QD is affected by nearby impurities or fluctuating charge traps in the barrier, the linewidth could be significantly broadened. Moreover, the surface of a photonic wire is very close to the QD, where numerous surface states capture the fluctuating charges, possibly modifying the built-in electric field inside the wire. Further justification of

3.3 Single Photon Emission via Photoluminescence Excitation Spectroscopy

the linewidth broadening mechanism could be provided with the photon correlation measurements.

3.3 Single Photon Emission via Photoluminescence Excitation Spectroscopy

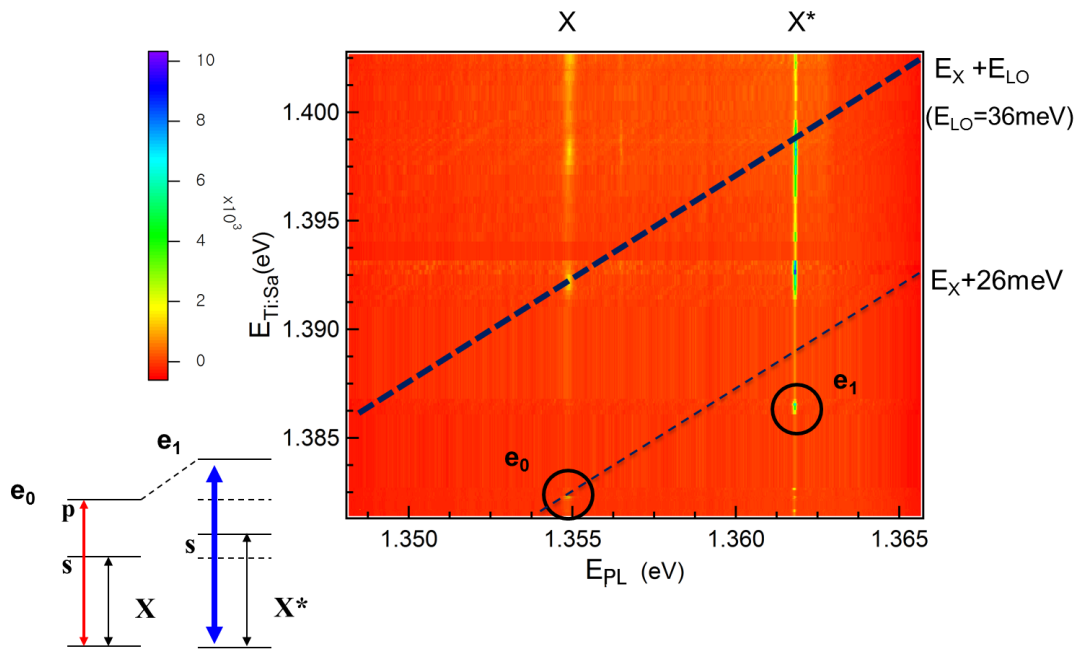


Figure 3.5: The photoluminescence excitation spectra in a GaAs photonic wire with a diameter of 200nm at 4K - Two-dimensional photoluminescence excitation (PLE) plot obtained by measuring photoluminescence spectra with several the laser excitation energy. The absorption resonance in the first excited state is indicated by the black circle. The blue dashed-lines indicate the phonon-mediated resonance.

Since excitonic species of a single QD were identified by the photoluminescence study, this section shows how the system emits most of photons from a single exciton in the dot via PhotoLuminescence Excitation (PLE) spectroscopy. As mentioned in Chapter 2, the quasi-resonant excitation enables the selective creation of a single excitonic line. In the PLE experiment, the laser excitation energy is swept while spontaneously emitted photons from the excitonic ground state are monitored. When the laser excitation energy is tuned into a transition resonance above the s-shell of a QD,

3. OPTICAL SPECTROSCOPY OF A SINGLE INAS QD IN A GAAS PHOTONIC WIRE

the transition resonances reveal themselves as a sharp enhancement of photons spontaneously emitted from the excitonic ground state. In this way, a careful tuning of the laser leads a clean situation where the photon-emission only comes from a specific excitonic line.

Figure 3.5 presents a typical map of the PLE measurement. As shown in Fig. 3.5, transition resonances of excitonic species are mapped by tuning a CW Ti:Sa laser energy of E_{TiSa} in steps of about 100~1000 μeV . When luminescence peaks is hardly observed, we skipped the data points in that region. Each photoluminescence spectrum was recorded under the same excitation power of $I_{ex} = 12.6 \mu\text{W}$. The integration time was 10 s. Colors of Fig. 3.5 indicate the intensity of luminescence. Alongside the PLE two-dimensional spectrum, the emission intensity from each s-shell line is extracted and recorded with respect to the laser excitation energy, and the result is shown in Fig. 3.6.

Clearly, the PLE spectrum shows absorption resonances of X and X^* . As the laser excitation energy increases, the X PLE spectra first reveals the resonance (e_0) at $E_{ex}=1.382 \text{ eV}$. Further scanning to the high energy side, the second resonance (e_1) at $E_{ex}=1.387 \text{ eV}$ is seen for X^* . The optical transitions are schematically summarized for X and X^* on the left side of Fig. 3.5. From the transition scheme, the p-state splitting between X and X^* is simply given by $V_p(= E(e_1) - E(e_0))=4.2 \text{ meV}$ which is large enough to select a clean single emission from a single QD. With the selective excitation of X^* , for example, all emission lines except X^* are absent, as shown with the photoluminescence spectrum taken at $P_{non-res}=0.0 \mu\text{W}$ in Fig.3.7(a).

Further scanning on third and fourth absorption resonances, selective “clean single emission” is no more reliable due to the LO phonon coupling; the phonon-assisted selective excitation of each X and X^* brings both of them into resonance. In general, phonon is the quantized vibrational modes of the crystal lattice. In the bulk GaAs, the presence of a diatomic basis distincts acoustic and optical phonons. The optical phonon has an energy of $E_{LO} = 36 \text{ meV}$ (68, 69). When the energy difference matches exactly to the bulk GaAs LO phonon energy, the phonon replica typically gives rise to the virtual phonon-mediated absorption resonance in the exciton line (69). In this context, X and X^* emission rates in vicinity of the phonon replica will be strongly influenced by the interaction with the LO phonon. As seen in Fig.3.6, the phonon-assisted X and X^* emissions are no more selective at third and fourth transition resonances and their absorption spectra seem to be correlated. This can be understood in terms of

3.3 Single Photon Emission via Photoluminescence Excitation Spectroscopy

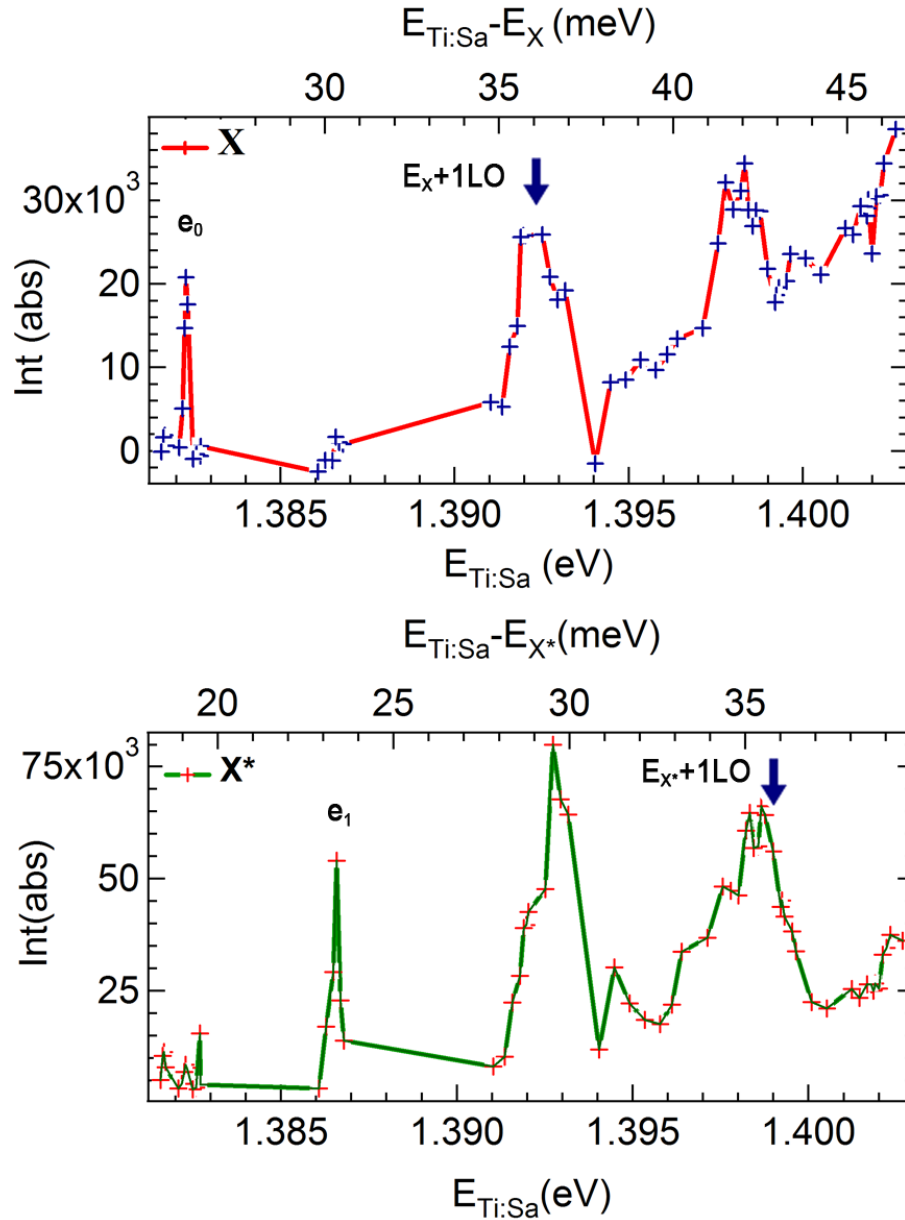


Figure 3.6: PLE spectrum of a single QD in a GaAs photonic wire with a diameter of 200 nm at 4 K - Integrated photoluminescence intensities of X and X* emission lines are presented in figures (a) and (b), respectively. PLE spectra are taken at the detection energy at around 1.392 eV, while CW Ti:Sa laser energy is tuned quasi-resonantly. The red and green solid lines connecting the crosses are, respectively, the X and X* PLE traces. As indicated by the arrow, the absorption resonance spectrum are shown corresponding to a p-shell transition.

3. OPTICAL SPECTROSCOPY OF A SINGLE INAS QD IN A GAAS PHOTONIC WIRE

their cross talking. If a neutral QD is selectively excited at $E_{ex} = E_X + E_{LO}$, the QD can possibly capture an extra charge in vicinity of the QD via LO phonon absorption. Then an electron and hole pair can scatter into the excited state of X^* , revealing the X^* emission line. When a QD initially containing a charge is selectively excited via LO phonon absorption ($E_{ex} = E_{X^*} + E_{LO}$), a charge can as well escape from the QD via the phonon scattering resulting in the X emission line. In such a way, the scattering of a charge via LO phonon seems to reveal in both absorption enhancement of neutral and charged states.

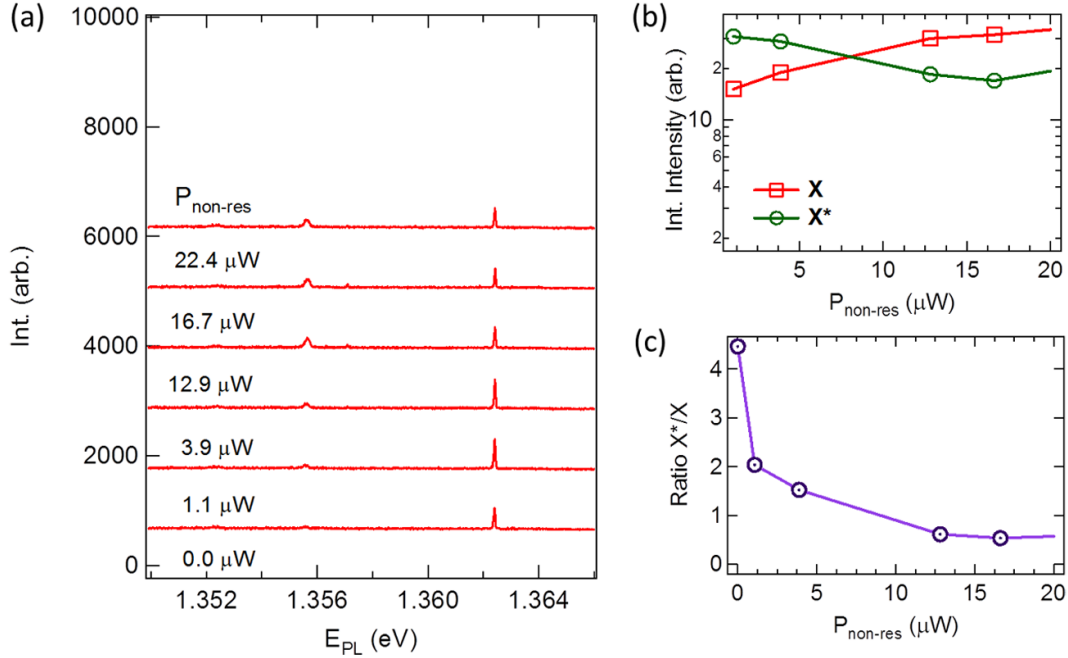


Figure 3.7: - (a) Photoluminescence spectra of a single QD under a fixed p-shell excitation of X^* at e_1 with several nonresonant excitation intensities. The X^* decreases as the simultaneous nonresonant power is increased. (b) The integrated intensities of X and X^* are shown as a function of nonresonant excitation intensity under a simultaneous p-shell excitation at e_1 . (c) Relative intensity variation of X with respect to X^* as a function of $P_{non-res}$ for a given quasi-excitation power of 12.6 μ W.

Still the identification of excitonic lines has ambiguity, one can have another clue from the photoluminescence evolution under simultaneous resonant sub- and nonresonant above-bandgap illuminations. The idea is as follows; if we excite the charge state with a selective quasi-resonant excitation, single charged QD emission line will only

3.4 Temperature-dependent Photoluminescence Excitation Spectroscopy

appear in the photoluminescence spectra. Once the above-bandgap laser is superimposed with that of the p-shell excitation, the nonresonant excitation induces carrier recombinations in the charged QD with extra carriers dissociated in the space charge region (55, 70). The QD discharging then leads the progressive appearance of exciton emission line. As seen in Fig. 3.7 (a), we first measure single X^* emission line at e_1 . As the nonresonant excitation power increases, X^* emission line progressively decreases with the appearance of X emission line. Figures 3.7(b) plots respectively the integrated intensity of X and X^* with respect to $P_{\text{non-res}}$ for a given quasi-resonant excitation $P = 12.6 \mu\text{W}$. The ratio between the integrated intensities decreases with higher $P_{\text{non-res}}$, as plotted in Fig. 3.7(c). The intensity exchange between X and X^* is in good agreement with the experimental observation (55).

3.4 Temperature-dependent Photoluminescence Excitation Spectroscopy

Returning to the generation of the single photons, another interesting question is how the single emission spectrum changes with temperature. Note that the temperature changes the carrier distribution in vicinity of the dot, thereby influencing the absorption properties of excitonic states. To capture the temperature effect quantitatively, PLE spectra were measured at 30 K, as displayed in Fig. 3.8. Indeed, the high temperature PLE spectrum reveals a thermal-induced indirect resonance of exciton at e_1 . From the comparison with low-temperature PLE of Fig. 3.6, the photoluminescence spectra recorded at e_1 now includes not only X^* but also X excited state resonance lines. The observation implies that the temperature induces the thermal perturbation of a carrier in the dot. Note that the inelastic phonon scattering processes increase at elevated temperatures (71), possibly assisting the carrier recombination in the dot with a thermally excited charge. Thermal-induced phonon effect will be discussed more in the next section. Starting from a charged exciton configuration at e_1 , carrier escaping processes result in the neutral dot, thereby revealing as X photoluminescence line. If the carrier is re-captured, the charged exciton configuration reveals again as X^* line. Two sequential events would then be integrated in a time-integrated photoluminescence spectra. In such a way, we see the temperature-induced leak in the neutral state X at e_1 in favor of X^* in high-temperature PLE of Fig. 3.8.

3. OPTICAL SPECTROSCOPY OF A SINGLE INAS QD IN A GAAS PHOTONIC WIRE

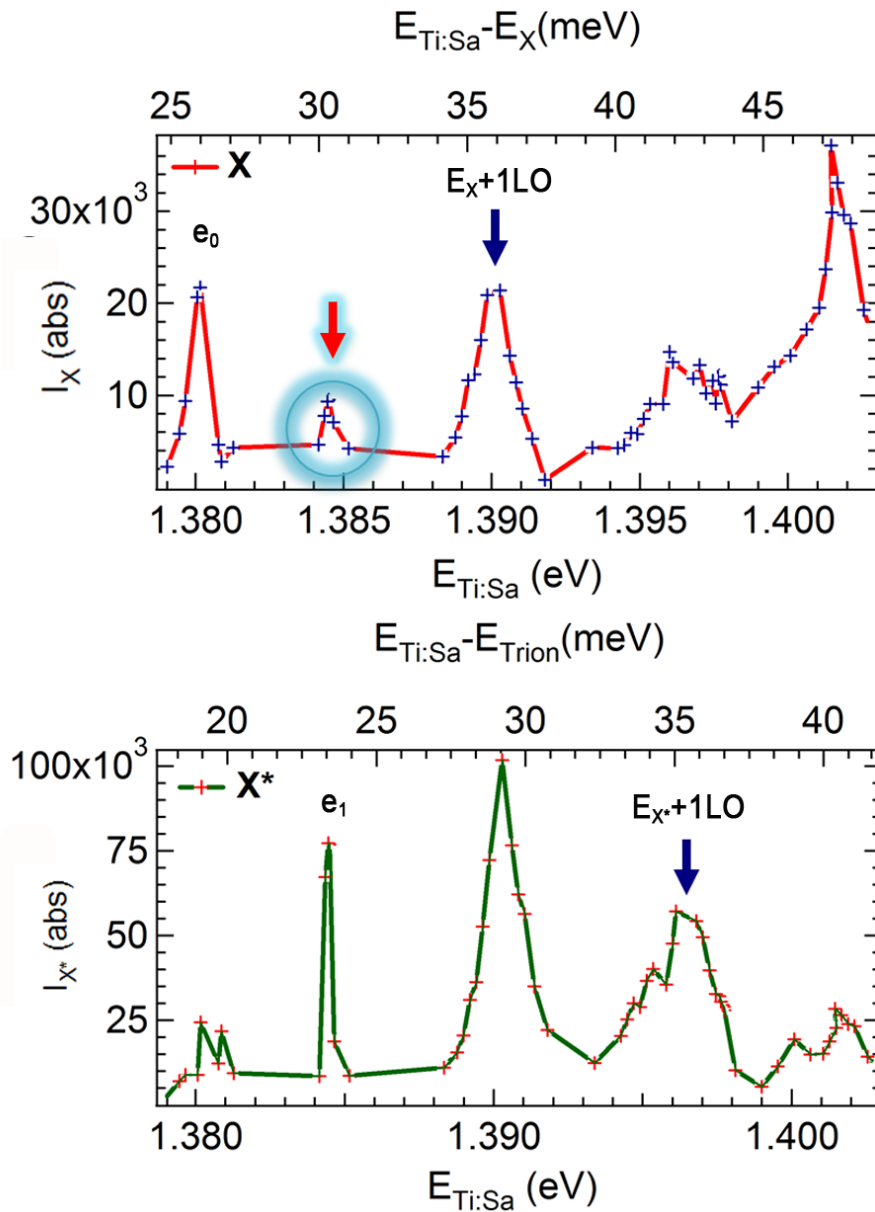


Figure 3.8: High temperature PLE spectrum of a single QD in a GaAs photonic wire with a diameter of 200nm - X and X* emission lines are monitored at 28K, while CW laser is swept. Photoluminescence integrated intensities of X and X* are, respectively, displayed in Fig.(a) and (b). Comparing with the low temperature case, the thermal-induced resonance of X at e_1 is indicated by the circle.

3.5 Temperature-dependent Photoluminescence Spectroscopy

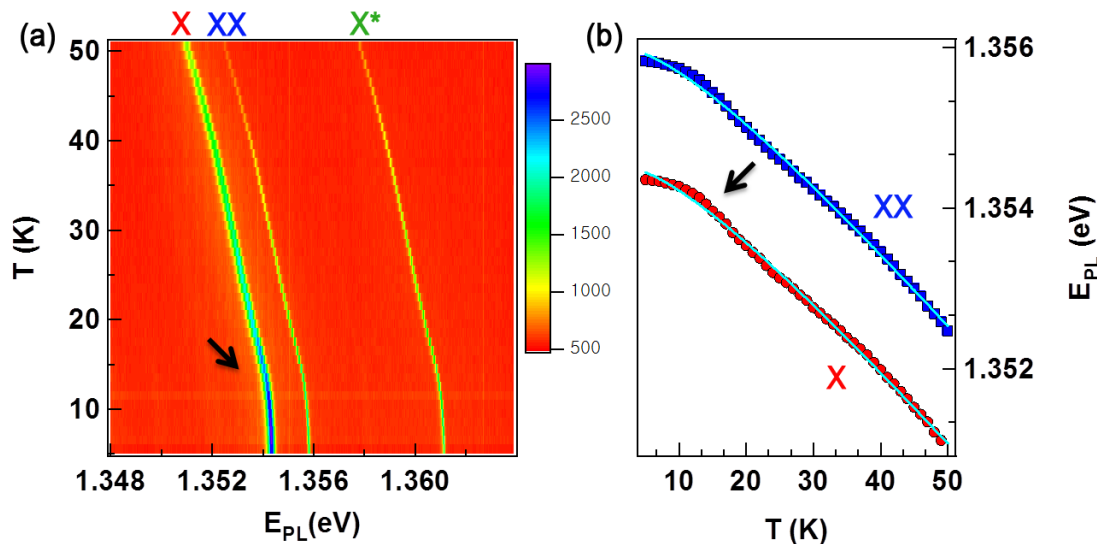


Figure 3.9: Temperature-dependence of integrated photoluminescence intensities peak evolution of a single InAs QD in a GaAs photonic wire with the diameter of 200 nm - (a) A collective photoluminescence spectra is shown versus the temperature ranging from 5 to 50 K. A color scale of the mapping indicates the intensity of photoluminescence spectra taken as a function of the temperature. (b) Temperature dependences of the photoluminescence emission peaks are presented as a function of temperatures ranging from 5 to 50 K. The red circle and blue rectangle correspond to the temperature dependence of the X and XX emission lines. The light-blue solid line presents the projected photoluminescence energy variations by using Varshni model.

For the implementation of single photon-QD devices, the QD system has to be well-isolated from its environment. Contrary to the atomic case, random interactions of a semiconductor QD with the environment can significantly perturb identical wave packets of emitted single photons. Such a loss of phase coherence will limit the indistinguishability of single photon-QD source due to dephasing. As intensively studied in literature, the temperature dependence of the photoluminescence spectrum has been used to probe the influence of environment charges on QD properties. In this section, we report the temperature-dependent measurements on the fundamental excitonic transition of a single InAs QD embedded in a photonic wire of 200 nm. Figures 3.9(a) and (b) show temperature-dependent photoluminescence evolutions of InAs QDs of a GaAs photonic wire from 5 to 50 K. As noted in the previous section, three emission lines X ,

3. OPTICAL SPECTROSCOPY OF A SINGLE INAS QD IN A GAAS PHOTONIC WIRE

XX , and X^* correspond to exciton, biexciton and charged-exciton. First interesting feature is sigmoidal temperature-dependences, as indicated with black arrow in Fig. 3.9. At relatively low temperature (< 50 K), the photoluminescence peak shows, in general, the monotonic redshift.

To understand the sigmoidal behavior, temperature-dependent photoluminescence evolutions are fitted by a well-known Varshni model. The Varshni model for bulk semiconductor (72, 73) is empirically expressed as

$$E(T) = E(0) - \frac{\alpha T^2}{\beta + T}, \quad (3.4)$$

where $E(0)$ is the band gap energy at 0 K and, α and β are the two Varshni coefficients to be determined. The Varshni equation was devised to fit the seemingly linear decrease in the high temperature region and the quadratic decrease in the low temperature region as observed in many semiconductor material systems.

The fitted dependences are shown in Figure 3.9(b). The light-blue solid line correspond to the projected energy gap variations by the Varshni model. Comparison with the fitted photoluminescence dependence, the evolution of photoluminescence peak energies of X and XX exhibit three regions: first region below 20 K in which the photoluminescence peak energy slowly decays and a transition region near 20 K where the photoluminescence peak energy decreases rather rapidly; high temperature region where the Varshni model tracks accurately. As will be discussed later, this phenomena could be connected with the surface effect on a GaAs photonic wire embedding a single QD. This point will be discussed in more details in the next chapter.

To bring more informations about environment effects on single QDs, the temperature dependences of photoluminescence emission linewidths are summarized in Fig. 3.10. With increasing temperature, fundamental transition linewidths of X and X^* broaden gradually but not identically. As shown with two solid lines in Fig. 3.10, good fits to temperature-dependent linewidths are obtained using a common model of

$$\Gamma(T) = \Gamma(0) + aT + be^{(-E_a/k_B T)}. \quad (3.5)$$

Here, $\Gamma(0)$ is the zero-temperature linewidth. The linear term aT accounts for dephasing by acoustic phonon scatterings, while the last term $be^{(-E_a/k_B T)}$ accounts for dephasing by optical phonon scatterings characterized by the activation energy E_a . By fitting with Eq.(3.5), we estimate that $a = 1.0$ $\mu\text{eV/K}$ for X , and $a = 1.4$ $\mu\text{eV/K}$

for X^* . Estimated thermal broadening coefficients of $a \sim 1 \mu\text{eV}$ is within a reported range of $0.05 \mu\text{eV/K}$ to $2 \mu\text{eV/K}$ (74, 75, 76) for a single QD. Rather large thermal broadening coefficient reveals a considerable environment effect on the lineshape of single QDs. For example, thermal fluctuations of charges around the dot may induce the spectral jittering involving the acoustic phonon absorption. As for the activation energy, we evaluate $E = 29K$ for X and $E = 20K$ for X^* . Thermal quenching of the emission intensity also gives the estimated activation energies of 29 K for X , and 28 K for X^* (see, Fig.3.10 (a)), comparable with the evaluation from Eq.(3.5). However, fitted values of E are one order of magnitude smaller than reported values (77, 78, 79). Different binding energies of the two excitonic species seem to cause the 10 K difference in activation energies between X and X^* .

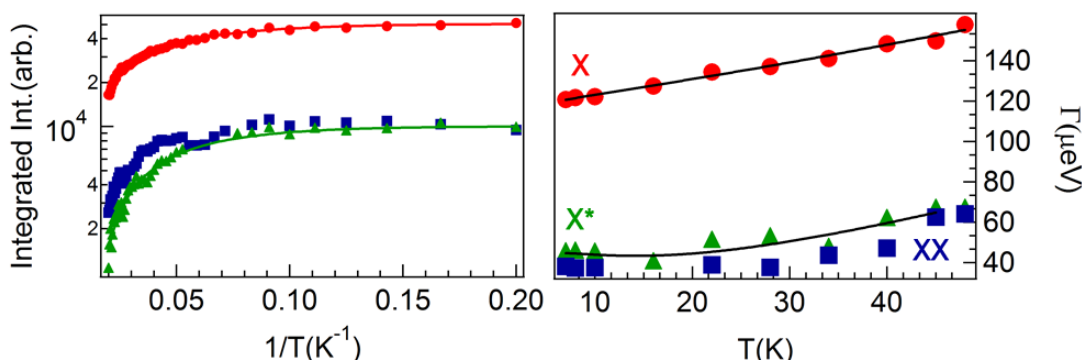


Figure 3.10: Temperature-dependence of the photoluminescence peak evolution of a single InAs QD in a GaAs photonic wire with the diameter of 200 nm - (a) Photoluminescence integrated intensity is plotted with temperature ranging from 5 to 50 K. Solid lines present a least-squared fit for X and X^* . (b) Temperature dependence of the photoluminescence linewidths is displayed with temperature. The red circle, blue rectangle and green triangle respectively correspond to the temperature dependence of the X , XX and X^* emission lines.

3.6 Chapter Summary

First, an experimental setup was presented in detail for optical spectroscopies. Basic optical properties were then characterized for self-assembled single InAs QDs embedded in a needle-type GaAs photonic wire. Photoluminescence spectroscopy was first

3. OPTICAL SPECTROSCOPY OF A SINGLE INAS QD IN A GAAS PHOTONIC WIRE

presented in order to identify the transition energies of a QD family. The power dependence of the QD family revealed them as neutral exciton, charged exciton and biexciton. PLE spectroscopy was then presented for the next step, which identified the p-states of QD species. Motivated by significantly different linewidths between the neutral exciton and biexciton, another method was also used to clarify their relation, including killing the charged state by superimposed quasi-resonant and nonresonant excitations. As the different linewidths were attributed to environment effects on single QDs, a typical temperature study was then performed. Their temperature dependence presented rather sigmoidal behavior at 20 K. The change of QD emission energies around 20K will be further discussed in the following Chapter 4 with the new generation of trumpet-like photonic wires.

4

Surface effects in a semiconducting photonic wire; spectral stability of an embedded single QD

Efficient nanophotonic devices like single photon sources require to funnel a large fraction β of the spontaneous emission (SE) of a single emitter into a single optical mode. This situation offers an ideal platform for quantum optics and quantum information processing experiments (5, 80). In this context, photonic semiconducting nanowires (photonic wire) embedding a single quantum dot (QD) have emerged as appealing systems (38, 61, 81). As we already described Chapter 2, these monomode waveguides made of a high refractive index material offer a tight lateral confinement of the guided mode while simultaneously screening all the other transverse modes. Hence, they ensure an efficient SE control over a broad wavelength range ($\beta \geq 90\%$ over a bandwidth exceeding 70 nm at $\lambda = 950$ nm) (38, 61). Here, β factor has already been defined in Chapter 2. Moreover, the far-field outcoupling efficiency of the guided mode can reach unity by proper engineering of the wire ends (61). Following this strategy, an on-demand single-photon source with a record-high brightness was demonstrated (38).

However, miniaturization of photonic devices enhances surface effects, inducing for example non radiative surface recombinations, which affect the emission properties of semiconducting nanowires (82, 83). In the case of photonic wires, single mode operation

4. SURFACE EFFECTS IN A SEMICONDUCTING PHOTONIC WIRE; SPECTRAL STABILITY OF AN EMBEDDED SINGLE QD

imposes a wire diameter $d \lesssim \lambda/n$, where n is the index of refraction of the material. For GaAs photonic wires, the QD is thus located at distances not larger than 100 nm from side walls. It was shown in Ref. (38) that the almost perfect QD radiative yield is preserved in photonic wires with d as small as 200 nm. Photon correlation experiments showed no bunching in the 1-100 ns temporal range (38), a strong evidence of absence of blinking at this timescale. Nevertheless, the spectral stability of the photonic wires, crucial for resonant quantum optics experiments, has not been investigated so far. In this chapter, we perform high resolution spectroscopy and show that the excitonic emission line of the QD undergoes a continuous energy drift. We discuss the possible origin of the phenomenon, which we attribute to oxygen adsorption on the wire side walls, and demonstrate a way to circumvent this problem with a proper surface treatment.

4.1 Electronic Surface States in p-type Semiconductor

Periodicity of the chemical bonding in the semiconductor crystal is disrupted at the surface, resulting in dangling bonds. Since the band structure is related to the periodicity of the crystal, the surface electronic structure is modified. As a consequence, the unsaturated covalent bonds (dangling bonds) build up a high density of surface states for electrons at the free surface of semiconductors. For a p-doped semiconductor, the dangling bonds give up electrons to neutralize free holes in the bulk. The result is a modification of the band that can reach inside the photonic wire.

In earlier studies, surface states of the p-doped GaAs semiconductor are observed at 0.7 eV and 0.8 eV above the valence band respectively for the As missing acceptor-like and Ga missing donor-like states (84). The situation for a p-type GaAs bulk material with these surface states is illustrated in Fig. 4.1(a). It has been found by Iimura (84) that the number of surface states per unit area is respectively at least about $\sim 10^{18} \text{ m}^{-2}$ for the acceptor-like level and, about $\sim 10^{17} \text{ m}^{-2}$ for the donor-like level. Filled surface Ga donor-like states in principle could give off electrons into empty available acceptor states and can therefore lead to a positively charged surface. Due to the charge neutrality, the net positive surface charge n_s is balanced by a region around the GaAs surface of equal negative charge $-n_s$, referred to as the depletion region. Alternatively, the positively charged traps compensate electrons from the Fermi level by lowering the energy band in the vicinity of the surfaces. Until overall charge neutrality

4.2 Band Bending in p-doped Photonic Wires

is satisfied, the surface traps are filled and neutralized by finally stabilizing the Fermi level at the position of the average energy at the surface. Therefore, the positive surface potential results in downward-bent bands. Figure 4.1(b) depicts a depletion layer and its band-bending at the GaAs surface.

The shape of band bending can be described by solving the Poisson equation $\nabla^2 V = -e^2 N_D / \epsilon$. Here, N_D is the dopant density per unit volume and ϵ is the dielectric constant of the material. Therefore, in principle, the magnitude of electric field is determined by doping types and levels in the depletion region and the carrier concentration at the surface. As dictated by doping, the band bending profile contains a net surface charge $-n_s$ by depleting free carriers over a distance d_{dep} , as illustrated in Fig. 4.1 (b). One can see that, in the depletion region, the same but the opposite sign of free carriers make balance with the surface charge $n_s = -d_{dep} N_D$ within a few lattice constants maintaining charge neutrality. The surface charge n_s thus form a dipole layer over a depletion distance d_{dep} with carriers $-n_s$ left behind from acceptor states that screens the semiconductor interior.

4.2 Band Bending in p-doped Photonic Wires

For photonic wires with a small diameter and a moderate doping, the depletion layer extends throughout the nanowire (82) by pinning the Fermi level at the midgap, as shown in Fig. 4.2. Note that photonic wires contain an extremely high density of surface states due to the large surface-to-volume ratio. Since the Fermi energy pinning at the surface strongly depends on the geometry and size of the wire, photonic wires exhibit a size-dependent depletion space charge layer. A schematic of surface state effects on band bending is depicted in Fig. 4.2 with different diameters. The photonic wires with small diameters lower than the depletion width in bulk ($R < d_{dep}$) result in the full-depletion of the entire wire. Even large diameters ($R > d_{dep}$) show an appreciable band bending by depleting the layer up to d_{dep} from the surface.

For an order of magnitude estimate, let's take the GaAs photonic wire under study with the typical GaAs band-gap energy $E_{BG} = 1.51\text{eV}$ and the unintended residual doping density of $p = 10^{22} \text{ m}^{-3}$. The dopant density corresponds to 1 dopant for every 10^6 crystal atoms. Assuming a planar interface, the depletion length is given by

$$d_{dep} = \sqrt{\frac{2\epsilon_r \epsilon_0 \Delta V}{e^2 N_D}}. \quad (4.1)$$

4. SURFACE EFFECTS IN A SEMICONDUCTING PHOTONIC WIRE;
SPECTRAL STABILITY OF AN EMBEDDED SINGLE QD

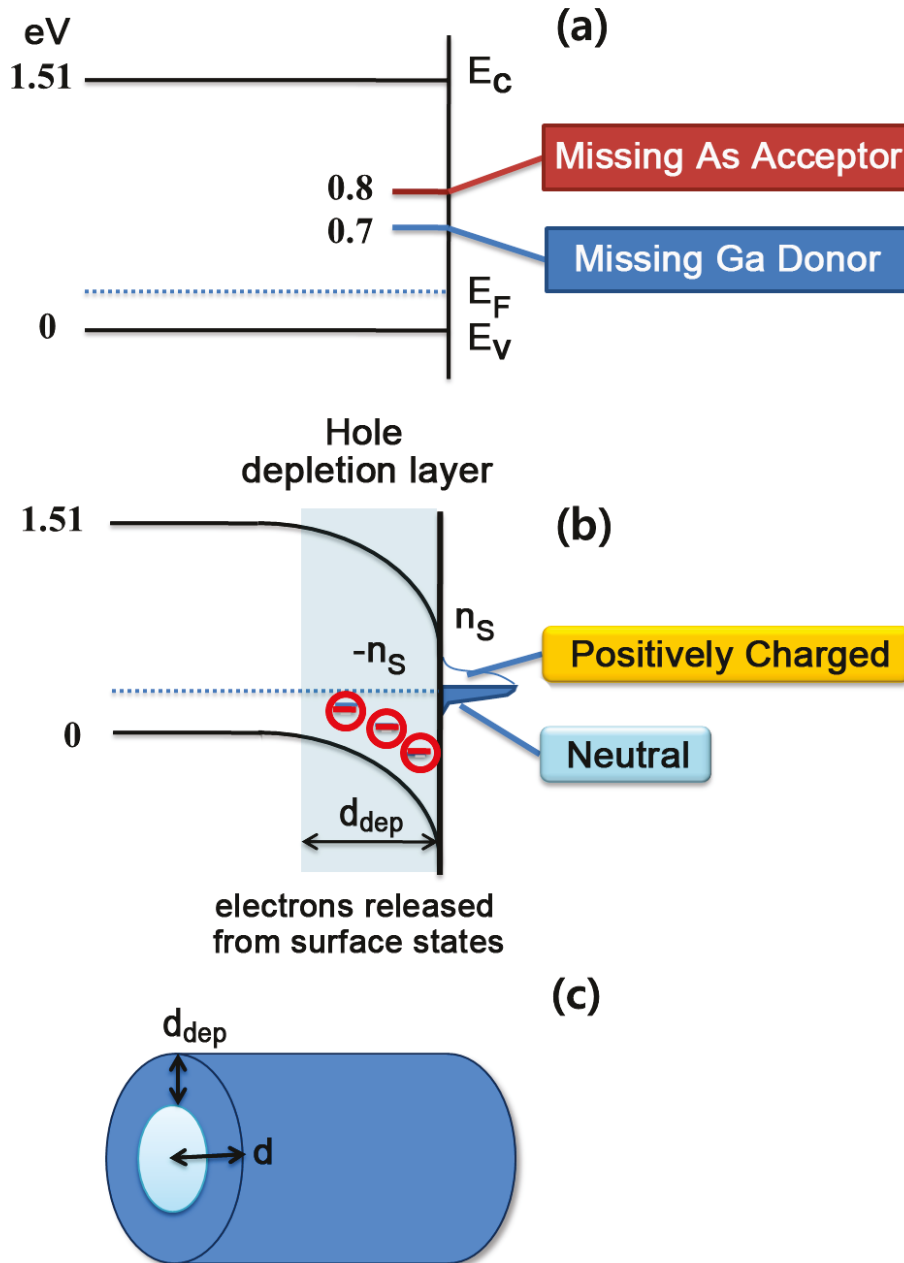


Figure 4.1: Schematic diagram for the Fermi-level pinning mechanism in p-type semiconductor - (a) Surface states in GaAs band gap. There are 0.8eV and 0.7 eV acceptor-like levels due to respectively missing As and Ga.(b) Actual band profile dictated by the Fermi level pinning. Surface Fermi level is pinned at the midst of the acceptor trap level. The acceptor-like traps have partially emptied to the level at which the positive surface state charge equals the negative surface depletion charge. (c) The depletion layer (thickness d_{dep}) of a GaAs photonic wire is illustrated for the band bending caused by Fermi level pinning at surface.

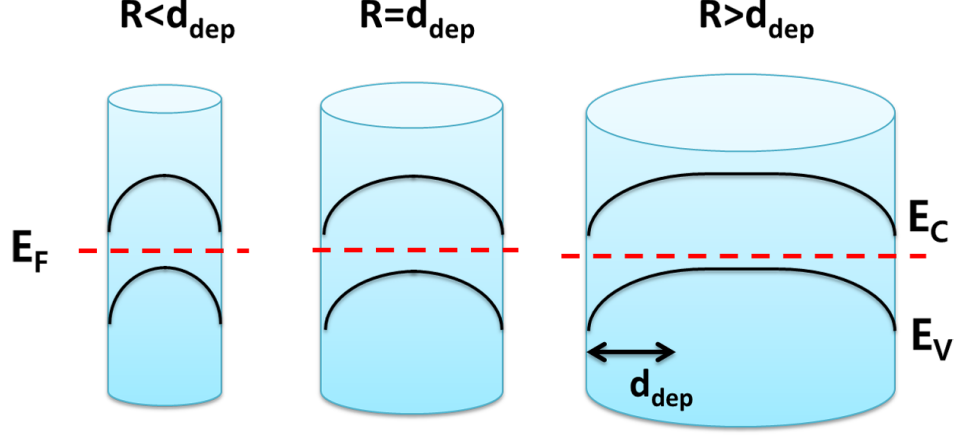


Figure 4.2: Schematic of a band bending profiles in p-type photonic wires with different radii R . - The dependence of valence (E_V) and conduction (E_C) band profiles are depicted with different diameters d of photonic wires. The surface states cause the Fermi level (E_F) to be pinned at the middle of the band gap and induce a band bending. Below the depletion width d_{dep} in bulk, the photonic wire is depleted throughout the entire wire. For larger diameters, the wire is depleted up to the depletion depth d_{dep} from the surface.

Recalling the Fermi level pinning at the middle of the gap, $\Delta V = \Phi \equiv E_{\text{trap}} - E_{\text{VB}} = 0.7 \text{ eV}$ (85) with relative permittivity $\epsilon_r \sim 12.9$. For $p = 10^{22} \text{ m}^{-3}$, this results in a depletion layer of about 340 nm or about 680 lattice constants. In our study, the radius of the photonic wire containing InAs dots is varied from 200 nm up to few μm for systematic studies. Hence, photonic wires are fully depleted at the dot location and the surface built-in electric field is then present over its entire cross-section. For a radius comparable or larger than 340 nm, the surface charge is about $n_s \gtrsim N_D d_{\text{dep}} = 3.4 \times 10^{15} \text{ m}^{-2}$. Since the total surface density of states is about $\sim 2/a_0^2 \sim 6 \times 10^{18} \text{ atoms} \times \text{m}^{-2}$, the surface chemical potential is effectively fixed by pinning of the Fermi level.

Clearly, as the radius is reduced further, the surface effect alters significantly the electrical properties of photonic wire due to the band bending extending deep inside the wire. (see Fig. 4.2) Numerical calculations for GaAs photonic wires have confirmed that a photonic wire of small diameters $D_{\text{QD}} = 250 \text{ nm}$ ($< 340 \text{ nm}$) results in full-depletion of the wires. Here, D_{QD} denotes the diameter of the photonic wire at the dot location. Simulation using the silvaco program shows that the field inside the wire is proportional

4. SURFACE EFFECTS IN A SEMICONDUCTING PHOTONIC WIRE; SPECTRAL STABILITY OF AN EMBEDDED SINGLE QD

to the surface charge. Due to the conical shape of the photonic wire a small and almost constant $F_{\parallel} = 1.4$ kV/cm component of the electric field exists along the vertical axis of the wire. The radial electric field F_{\perp} ranges from 0 kV/cm on the photonic wire axis to -26 kV/cm at the surface. As shown in Fig. 4.3 (b), the Fermi level is situated in the center of the photonic wire away from the edges of band-gap. The surface built-in electric field F resides even in the center due to the band bending extension deep inside the wire.

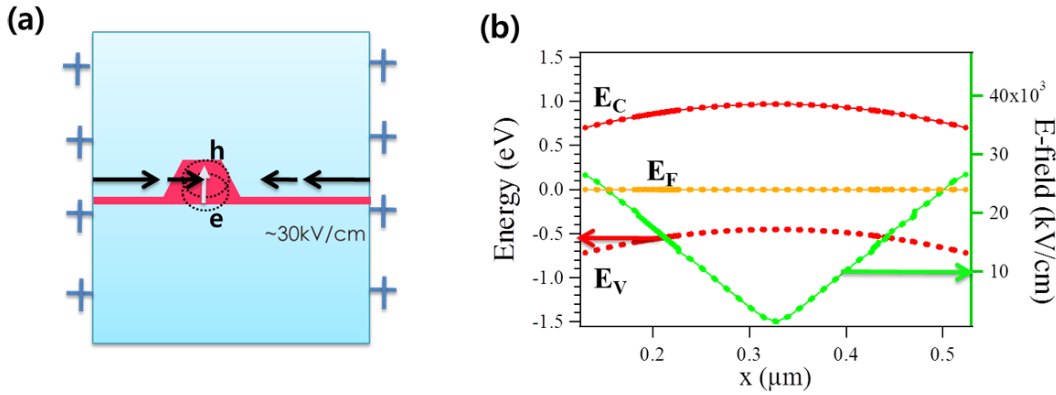


Figure 4.3: Schematic diagram for the Fermi-level pinning mechanism in p-type GaAs semiconductor - (a) Schematic of a p-doped GaAs photonic wire is shown near the QD plane. White arrow indicates the dipole moment of QD. Black arrows denote the surface built-in electric field. At surface, the calculated surface electric field is about 30 kV/cm. (b) Numerical calculation of band profiles and surface built-in electric field for $p = 10^{22}$ m $^{-3}$ GaAs photonic wire of $D_{\text{QD}} = 250$ nm

4.3 Emission Energy Drift of an Embedded Single QD

The band bending due to the surface states of photonic wires is responsible for a number of effects on photoluminescence measurements of an embedded single InAs QD. An initial photoluminescence spectrum from a single selected QD in a $D_{\text{QD}} = 370$ nm bare photonic wire is shown in Fig. 4.4(a) with 0.1 s integration time at 3.5 K. The quantum dot is excited by pumping of the wetting layer (825 nm) at a low power ($P/P_{\text{sat}} = 0.2$, where P_{sat} is the saturation power of the QD). Figure 4.4(b) presents the photoluminescence peak position E_{PL} versus time for the same single QD. photonic wire at 3.5 K. Each photoluminescence peak position is extracted by fitting a Lorentzian

4.3 Emission Energy Drift of an Embedded Single QD

to the QD spectrum at each time. A regular drift \dot{E}_{PL} of the emission energy towards higher frequencies is observed (blue-drift), $\dot{E}_{\text{PL}} > 0$.

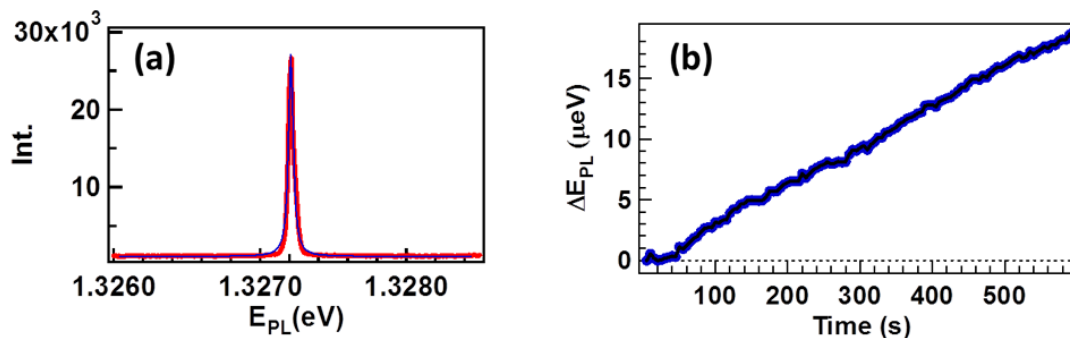


Figure 4.4: Photoluminescence spectra and blue-drift for a single InAs QD in a GaAs photonic wire - (a) Measured photoluminescence spectrum is shown with a Lorentzian fit at 3.5 K. (b) Photoluminescence peak position versus time is shown for the integration time 5 s.

A linear fit of the data of Fig. 4.4(a) gives a drift of about 30 neV/s. At 3.5 K, \dot{E}_{PL} remains constant over 8 hours. Over this period of time, photoluminescence intensity does not change significantly, its linewidth remains limited by the resolution of the spectrometer, and lifetime measurements show a small decrease from 1.65 to 1.58 ns. Warming up to room temperature and pumping on the cryostat resets the emission energy to its initial lower value. A systematic study of many photonic wires with different diameters (check Fig. 4.5(b)) reveals that all QDs are affected by a blue-drift whose amplitude decreases with increasing diameter. Finally, the same experiment with QDs in capped photonic wires shows no drift (Fig. 4.5(a), $\dot{E}_{\text{PL}} \leq 0.7$ neV/s). The wire surface is pretreated by wet chemical etching and the sulfur passivation. Then the wire is capped with a 20 nm Si_3N_4 layer and is protected from GaAs-surface oxidation.

Previous observations clearly point towards surface effects. Since the photonic wires are etched during their fabrication, there is a large density of surface traps for carriers (82) $n_s \gtrsim 10^{12} \text{ cm}^{-2}$. As mentioned above, the region of the photonic wire containing the dots is fully depleted and an electric field is present over its entire cross-section, explaining why all studied QDs experience a drift. An embedded InAs QD subjected to such a field experiences a Stark energy shift (86, 87) $\Delta E_{\text{Stark}} \approx -d_{\parallel} F_{\parallel} - \alpha_{\perp} F_{\perp}^2$, with $d_{\parallel} \approx 40 \text{ } \mu\text{eV} \cdot \text{kV}^{-1} \text{ cm}$ and $\alpha_{\perp} \approx 4 \text{ } \mu\text{eV} \cdot \text{kV}^{-2} \text{ cm}^2$. Here, F_{\parallel} and F_{\perp} denote the electric

4. SURFACE EFFECTS IN A SEMICONDUCTING PHOTONIC WIRE; SPECTRAL STABILITY OF AN EMBEDDED SINGLE QD

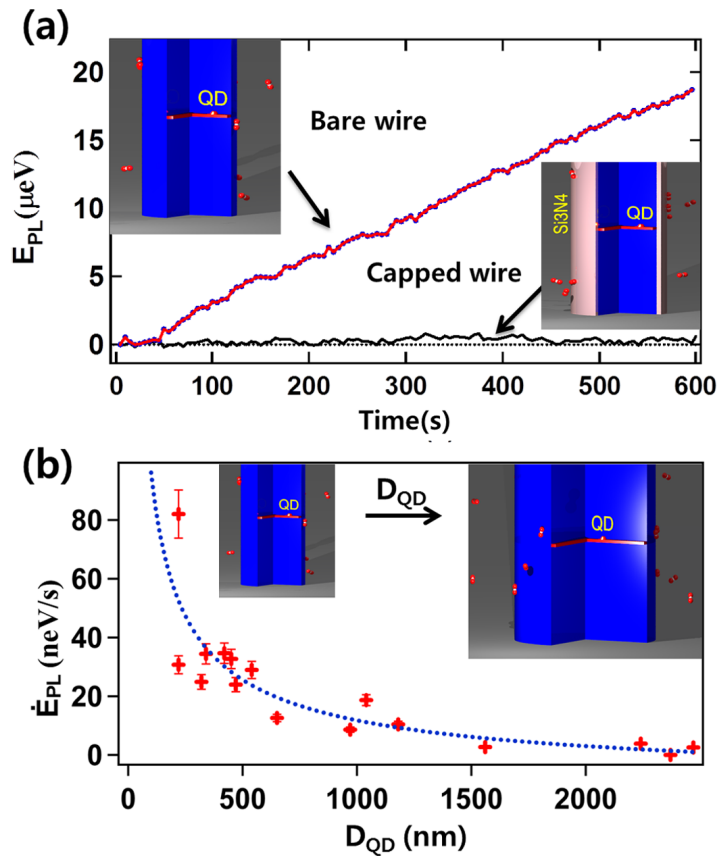


Figure 4.5: Blue drift in a bare photonic wire - (a) Emission energy E_{PL} as a function of time for a QD in a bare photonic wire (blue line) and in a capped photonic wire (black line). (b) Measured drift \dot{E}_{PL} for an ensemble of QDs in bare photonic wires as a function of the diameter. Schematics of bare and capped photonic wires are shown, where blue corresponds to GaAs and pink to Si_3N_4 materials.

4.3 Emission Energy Drift of an Embedded Single QD

fields parallel and vertical to the wire axis respectively. We note that a blue-drift implies a reduction of the electric field hence a diminution of the positive net charge at the surface of the photonic wire.

We attribute this effect to the physisorption of O_2 onto the wire surface (88, 89, 90). The reset of E_{PL} to a low value after warming up to room temperature implies a reversible physical phenomenon and not an irreversible chemical surface reaction. Figure 4.6 illustrates the physical mechanism of surface potential change via oxygen adsorption, which reduces the surface electric field. As discussed previously, the GaAs photonic wire surface carries huge positive charges as shown in Fig. 4.6 on top-left. Even in the vacuum cryostat, there is residual gas which interacts with these surfaces. Oxygen in the vicinity of surface can easily stick to the photonic wire surface attracting bulk electrons due to the high negative electron affinity GaAs surface. Thus, oxygen can be trapped in the surface states ($[O_2 + e^- \rightarrow O_2^-]$) and neutralize the surface, thereby diminishing positive net charges at the surface of photonic wires. The corresponding electric field reduction by the physisorption of oxygen is described under the diagram of GaAs photonic wire in Fig. 4.6.

In addition to this O_2 physisorption mechanism, another important issue is a surface barrier of electrons needed to release (capture) into (from) the air. This barrier is, by definition, the electron affinity level. Since the electron affinity level mainly determines the reaction rate of O_2 adsorption, the surface barrier informs the corresponding electric field reduction rate via the oxygen physisorption. Figure 4.7 shows the energy level diagram for physisorbed O_2 on GaAs surface. The electron affinity level E_a drawn in Fig. 4.7 for isolated O_2 is initially 0.45 eV below the vacuum level. Once O_2 atom approaches the surface, the O_2 affinity level drops and is broadened by its image charge in the dielectric. The appreciable downward-shift of O_2 affinity level has been observed around $2 \sim 3$ eV (88, 91, 92). Consequently, electrons must overcome the potential barrier still far away in order to bring O_2 atoms closer to the wire surface. Despite the out-of-resonance affinity level, O_2 interactions are still possible due to a tail of the Lorentzian affinity level possibly resulting in a partial wave function overlap. The local electron affinity level indicates that the O_2 adsorption to the wire surface happens in long time scale. Note that the surface carrier dynamics, such as the oxygen trapping, are resolved in photoluminescence measurements (E_{PL}) over several seconds. The surface dynamics reflected in the E_{PL} at 3.5 K, remains constant over 8 hours. In accordance,

4. SURFACE EFFECTS IN A SEMICONDUCTING PHOTONIC WIRE; SPECTRAL STABILITY OF AN EMBEDDED SINGLE QD

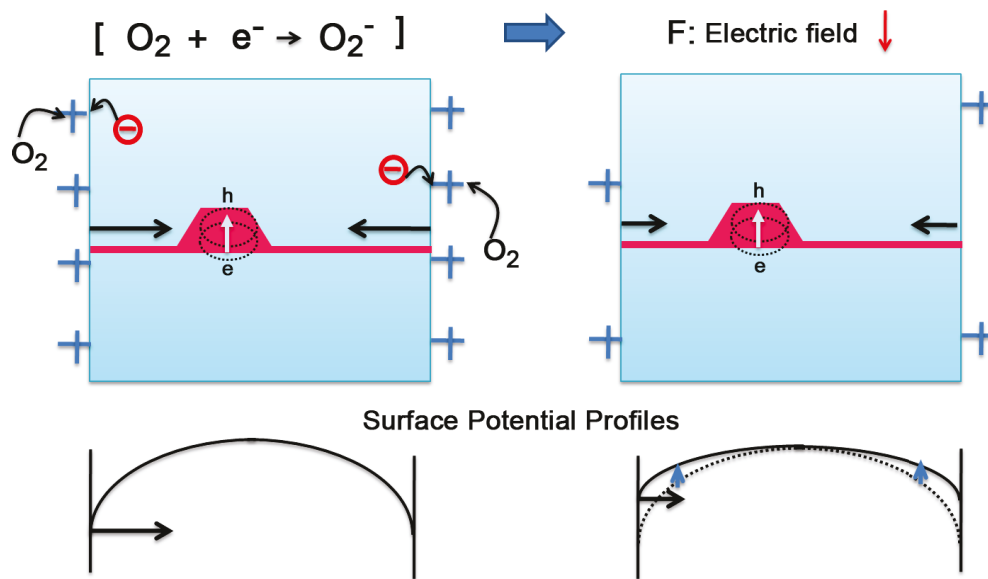


Figure 4.6: Schematics of oxygen physisorption process for p-doped GaAs photonic wire surface at the QD level - The top drawing shows the temporal evolution of the carrier density via O_2 adsorption at GaAs photonic wire surface. Left drawing shows physisorbed O_2 molecules that attract the free electron in the p-type GaAs photonic wire near the surface. In the right drawing, the surface positive charges are then reduced by an amount of hole neutralization process. The bottom drawing shows the schematic of energy band-bending diagrams of a photonic wire respectively corresponding to top surface trap states. The surface neutralization results in flattening of the energy band bending.

4.3 Emission Energy Drift of an Embedded Single QD

the O_2 physisorption to the photonic wire surface in vacuum cryostat requires a long time, suggesting that the oxygen molecules still remain in close proximity to the surface over the order of hours. Moreover, the energy matching condition could significantly change via the temperature and the excitation laser energy.

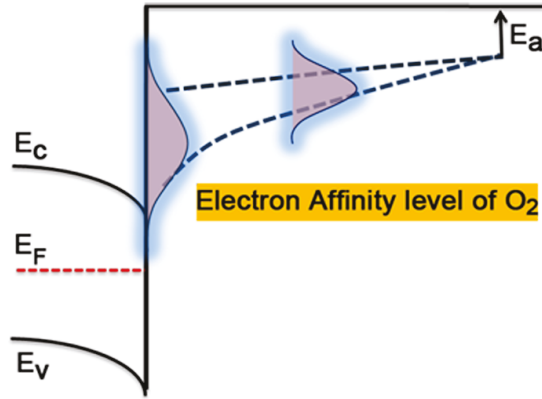


Figure 4.7: The electronic energy level diagram of physisorbed O_2 for p-doped GaAs photonic wire surface at the QD level - The O_2 electron-affinity level E_a is the required energy relative to bulk photoelectron energy level when an electron is added to the oxygen molecule. As O_2 approaches to the surface, the O_2 electron-affinity level shifts to the lower energy and its width is broadened.

The full circles on Fig. 4.8 represent the dependence of \dot{E}_{PL} as a function of T between 4 and 45 K in the same excitation conditions as in Fig. 4.4(b). A ten-fold increase is occurring from 4 to 20 K before the drift dramatically drops to values very close to 0 above 30 K. This observation is in good agreement with previous studies on the adsorption of O_2 on GaAs, which evidenced an adsorption peak around 20 K (90, 93). The same experiment for a capped photonic wire (full squares in Fig. 4.8) shows that \dot{E}_{PL} remains below $|4|$ neV/s over the whole temperature range, proving the drift cancellation by the capping. It demonstrates the efficiency of the capping for reducing the drift.

The temperature dependence of \dot{E}_{PL} under high excitation power ($P/P_{sat} = 3.8$; open circles in Fig. 4.8) exhibits the same characteristic peak. Its maximum value is however shifted to lower temperature at ~ 14 K and is dramatically smaller than for low power excitation. The pump laser can affect the photonic wire in different ways: it can locally warm up the photonic wire (explaining in particular the shift toward the low

4. SURFACE EFFECTS IN A SEMICONDUCTING PHOTONIC WIRE; SPECTRAL STABILITY OF AN EMBEDDED SINGLE QD

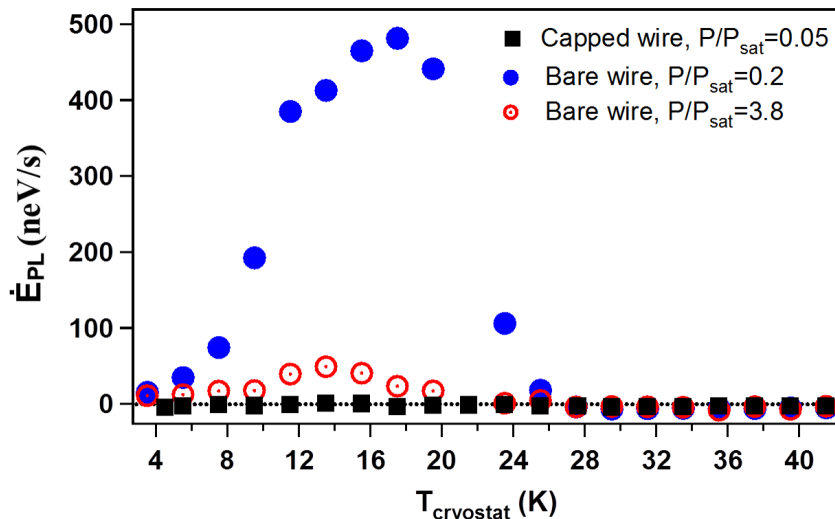


Figure 4.8: Temperature dependence of the temporal drift - \dot{E}_{PL} as a function of T for excitation power $P/P_{\text{sat}} = 0.2$ (full circles) and $P/P_{\text{sat}} = 3.8$ (open circles) in a bare photonic wire and for $P/P_{\text{sat}} = 0.05$ in a capped photonic wire (squares).

temperature of the peak at high power in Fig. 4.8), photocreated carriers can screen the electric field (85) or change the adsorption rate of O_2 .

To better understand the phenomenon, we have conducted systematic power studies at a fixed cryostat temperature $T = 4$ K. Figure 4.9(a) presents a typical experimental run: the drift \dot{E}_{PL} is determined from measurement of the emission energy over 5 min at different power values. Here, we also observe sudden shifts of the emission energy $\Delta E_{\text{PL}} < 0$ when the power is increased. We attribute it to a local warming of the photonic wire ($T_{\text{PW}} \geq T$) leading to the usual quadratic shift of the bandgap. For p-shell excitation, the amplitude of ΔE_{PL} is below the fitting uncertainty on the peak position ($0.1 \mu\text{eV}$). In the other two cases, there exists a linear increase of $|\Delta E_{\text{PL}}|$ with power. Its magnitude is hundred times larger for the GaAs band-gap excitation compared to the wetting layer excitation. All the concepts and techniques of laser excitations were already discussed in previous Chapters 2 and 3. Similar values have been observed for many QDs in photonic wires of similar size, capped or not.

The influence of power on \dot{E}_{PL} crucially depends on the excitation conditions (see Fig. 4.9(b)). For p-shell excitation, where no free carrier is injected in the bulk photonic wire and no heating is generated, it remains constant. In the case of the wetting layer excitation, where the local temperature T_{PW} remains below 6 K, one observes a

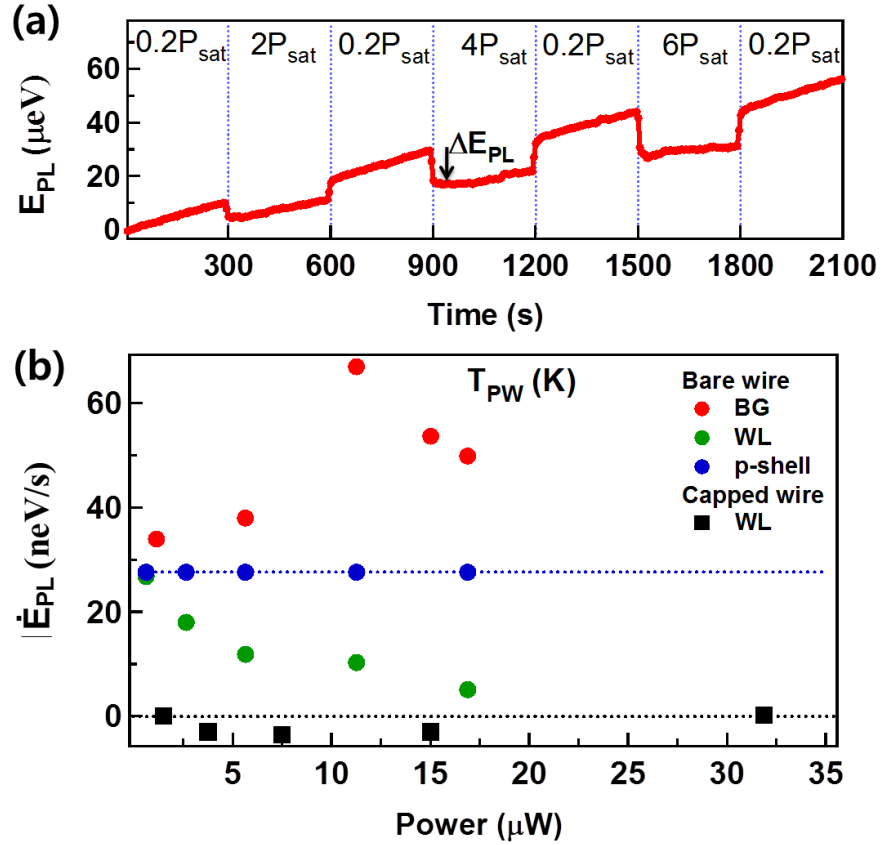


Figure 4.9: Power dependence of the blue-drift - (a) Excitation-intensity-dependent evolution of photoluminescence peak position for a QD in a bare photonic wire with time under the wetting layer excitation at $T = 3.5 \text{ K}$ (b) \dot{E}_{PL} versus laser power for a bare photonic wire under three different laser excitation energy: $E_{BG} = 1.52 \text{ eV}$ (red circles), $E_{WL} = 1.49 \text{ eV}$ (green circles) and $E_{p\text{-shell}} = 1.42 \text{ eV}$ (blue circles), and for a capped photonic wire (the wetting later excitation, black squares). The local temperature T_{PW} deduced from the sudden shift ΔE_{PL} is indicated next to some points.

4. SURFACE EFFECTS IN A SEMICONDUCTING PHOTONIC WIRE; SPECTRAL STABILITY OF AN EMBEDDED SINGLE QD

significant decrease of \dot{E}_{PL} . On the other hand for bandgap excitation, T_{PW} at high power is close to the maximum drift temperature of Fig. 4.8. This explains why we observe an increase of \dot{E}_{PL} , which is dominated by temperature effect. However, it is worth noting that its maximum value is 7 times lower than the one predicted by the low excitation results of Fig. 4.8. Hence, it is legitimate to think that, as in the case of the wetting layer excitation, the effect of temperature is strongly inhibited by an increase of excitation power. A possible explanation for our observations is the presence of photocreated carriers that screen the surface built-in electric field. This phenomenon should lead to a dramatic reduction of the electric field seen by the QD and hence induce a blue shift of its emission energy. This is in direct contradiction with the results of Fig. 4.9(a). Another explanation that remains to be confirmed could be a direct influence of the carriers or excitation light on the dynamics of adsorption and desorption of O_2 or on its capture of an electron.

Measurements of E_{PL} for many QDs in capped photonic wires showed no blue drift. The power dependence of \dot{E}_{PL} is given in Fig. 4.9(b) and is consistent with a complete suppression of the drift. We note that the sulfur passivation saturates GaAs dangling bonds at the surface by $(\text{NH}_4)_2\text{S}$, thereby reducing the density of surface traps. Although there may still exist a static electric field inside the photonic wire due to surface states at the GaAs/ Si_3N_4 interface, its value is frozen thanks to a 20nm - Si_3N_4 insulating layer. Therefore, the surface electric field no longer depends on the adsorption of molecules on the device. The frequency stability of the emission of a single QD is crucial if one wants to perform high precision resonant spectroscopic studies of a single emitter. In our device, the QD behaves now as a stable two-level system embedded into an optical waveguide made by the photonic wire. It is an ideal situation for studying non-linear effects at the single photon level and implementing simple quantum information operation between light and a solid state emitter(5).

4.4 Spectral Tuning of QDs

In this section, we present an alternative use of the surface effect. While this continuous spectral shift becomes a significant obstacle for high resolution resonant spectroscopy, the spectral shift can be used for tuning in resonance two QDs in the same wire. Individual QDs being in resonance has been a critical issue due to their interesting collective

behaviors, Dicke sub- and superradiances (94, 95). Unfortunately, conventional tuning techniques generally makes it very difficult to tune independently two QD emission energies into resonance. As we already discussed in Chapter 3, the temperature tunes identically all QD photoluminescence energies. In comparison to conventional tuning methods, resonance of two single QDs is given for free via its drift in our study. Once the spectral matching of individual QDs is achieved in one-dimensional geometries, it provides an opportunity for studying collective emission effects (95). In this context, we will show a simple trick to tune two QDs into resonance in this section.

4.4.1 Two QD Crossing: Continuous Tuning

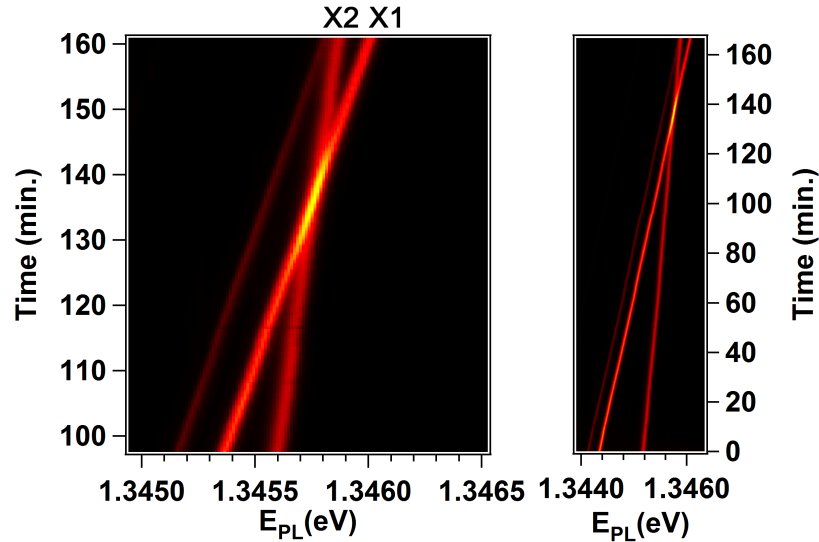


Figure 4.10: Time dependence of QD detuning in a GaAs photonic wire with a diameter of 370 nm. - A color scale of the mapping indicates the intensity of photoluminescence spectra taken as a function of time. Left: Time-dependent detuning of two QDs are plotted during 3 hours at 4 K under the wetting layer excitation. Right: A zoom-in on the region of interest from the left figure. The spectral matching is shown between two QDs emissions.

In this section, we show the precise wavelength matching of two individual QDs in the same wire by controlling their different drift rates in a reproducible way.

Here, the key is to play with the different drift rates of two QDs. Note that the QD blue-drift depends on its position from the surface as shown in Fig. 4.9(b). In a photonic wire embedding few QDs, a QD closer to the surface displays faster blue-drift.

4. SURFACE EFFECTS IN A SEMICONDUCTING PHOTONIC WIRE; SPECTRAL STABILITY OF AN EMBEDDED SINGLE QD

By performing blue-drift measurements in a 15 meV spectral range, two QDs are found to be spectrally matched in time. A single QD *X1* has an observed drift of 190 neV/s four times faster than that of QD *X2* in a GaAs photonic wire containing both QDs. Due to different evolutions of QD emission energies, we can scan a “fast” QD across the other “slow” QD.

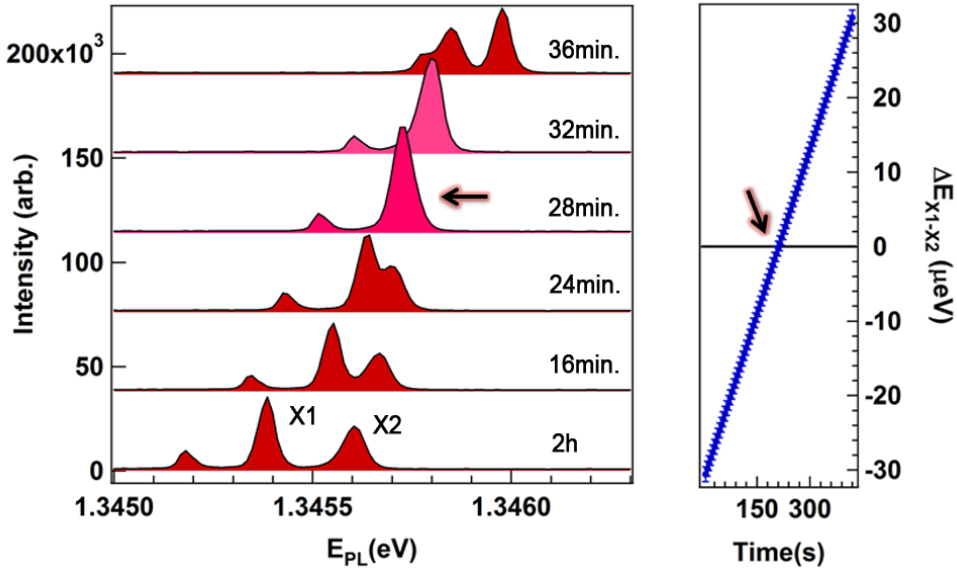


Figure 4.11: Time dependence of photoluminescence spectra in a GaAs photonic wire with a diameter of 370 nm. - (a) A set of photoluminescence spectra are taken at different time under the wetting layer excitation. Starting from red-detuned *X1* line from *X2* emission, the continuous fast blue-drift of *X1* line brings into the resonance with relatively slow *X2* emission. Corresponding times that took photoluminescence spectra are marked in the right hand side. (b) Relative detuning, extracted by fitting a Lorentzian function to photoluminescence spectra, are plotted versus time.

The selected QD *X1* emission is initially initially red-shifted by about 5.6 meV from the QD *X2* emission. Figure 4.10 shows a mapping of the emission of the selected QDs versus the time, measured well below the saturation. Selected QD emissions are around the spectral range of 1.3456 eV. The right side of Fig. 4.10 shows a mapping in long time-scale. Both QD emission energies vary linearly with time. As shown in Fig. 4.10, spectral matching is achieved at 4K after about 28 min (marked with arrows) as intended, while all other QDs are detuned. Further drift after resonance, the two QD lines are detuned and well resolved. To get the spectral matching of two QDs for

a well chosen time, one just needs to let two different QDs drift until the resonance under the same excitation power and the temperature. Note that the blue-drift highly depends on the power and temperature. Typically, our technique retains two QDs on resonance less than 1 min. The duration is not ideal for quantifying their cooperative effect in a statistical measurement (ex., the cross-correlation measurement). Still we could perform the QD life-time measurement to check the cooperative radiation.

To get a better insight, the photoluminescence spectra is plotted versus time in Fig. 4.11. Parallel to the detuning of two QDs, their emission intensities are need to be concerned. Comparing the photoluminescence spectra versus the time, a clear enhancement of $X1$ line is shown at resonance with $X2$ emission. Each peak position is extracted from a Lorentzian fitting function. Figure 4.11 (b) shows the relative detuning of $X1$ emission to $X2$ line. The resonance of two QDs possibly points toward a cooperative effect as all QDs couple to a single mode of photonic wire. To further investigate the QD talking at resonance, the cross-correlation measurement is mandatory.

4.4.2 Giant Blue Shift

Since $X1$ and $X2$ emissions are rather far away with an initial spectral distance of about 5.6 meV, waiting two QDs into resonance for several hours is quite time consuming. Here, the photoluminescence spectra shown in Fig. 4.12 were measured when their relative distance was rather close. Moreover, we have to warm up the cryostat to room temperature and cool down again to repeat this experiment, which requires several hours. As a better way to shorten the redundant time, we use a special technique to bring them closer with several giant steps in a deterministic manners. To reduce the spectral detuning between two QD emission lines in a controlled way, we cycle the cryostat temperature by warming-up to 20 K and cooling-down to 4 K. Figure 4.12 (a) shows QD line shifted of 170 μeV for each temperature cycle. As noted in previous sections, QD emission lines shown in Fig. 4.12(a) are governed by the blue-drift through surface electric field reduction. The main idea of Fig. 4.12 is to accumulate physisorbed O_2 on the surface with the maximal rate at 20 K and, return to 4 K. Note that the blue-drift significantly enhances around 20 K. By increasing the temperature up to 20 K, the QD line of Fig. 4.12(a) first shifts rapidly to the low energy-side due to the band-gap reduction (96). Soon after the reset to 4K, the QD line drift goes back

4. SURFACE EFFECTS IN A SEMICONDUCTING PHOTONIC WIRE; SPECTRAL STABILITY OF AN EMBEDDED SINGLE QD

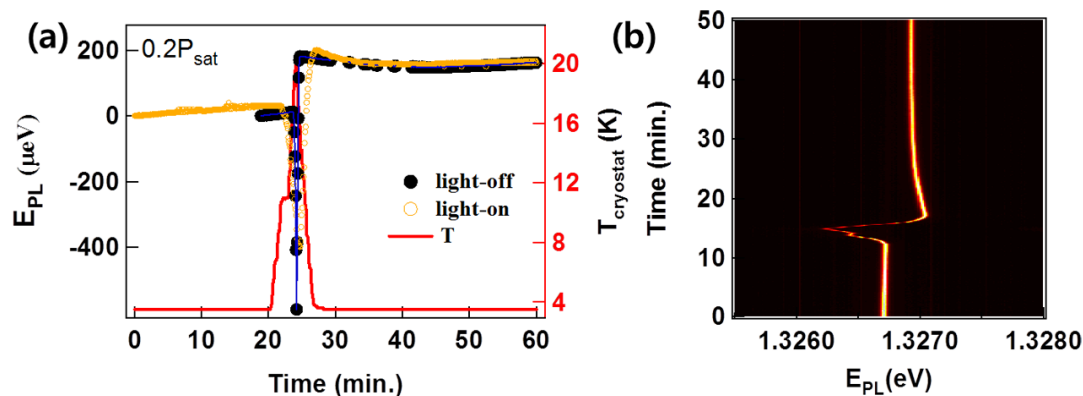


Figure 4.12: Spectral tuning of a single QD with 20 K temperature cycle - (a) Performing a 20 K temperature cycle, the dependence of photoluminescence peak position is plotted in the dark and under illumination. After 20 K thermal cycle, the photoluminescence emission line shifts by $170 \mu\text{eV}$ toward the high energy-side. (b) Collective photoluminescence spectra are plotted as a function of time. QD lines first drift towards high energy-side through the surface electric field reduction. After, QD lines shift rapidly to low energy-side induced by increasing temperature. After a warm-up and cool-down cycle, the QD line reaches a stationary state and stays there for 30 min.

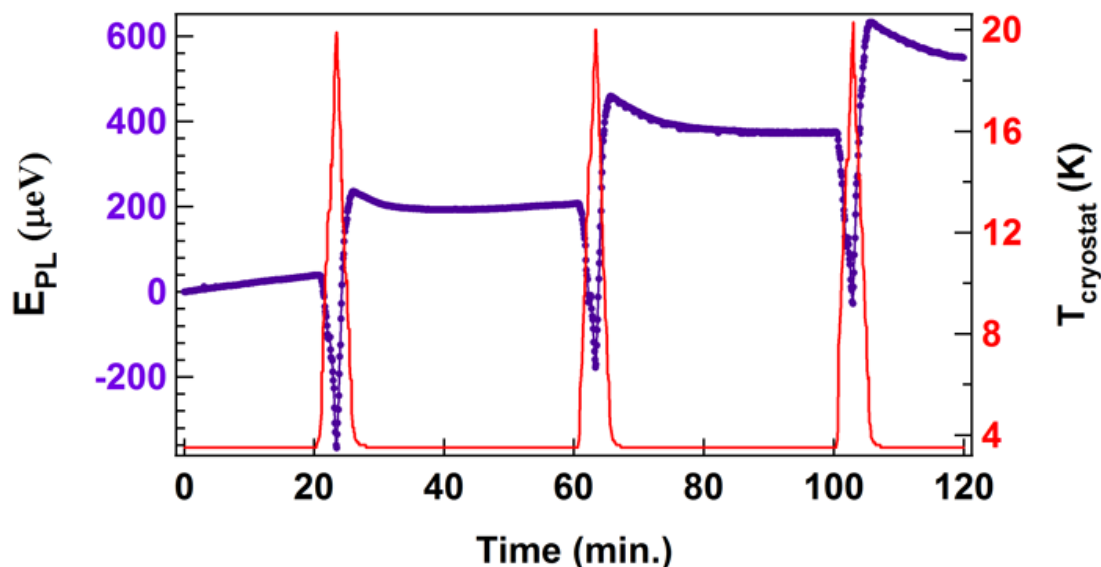


Figure 4.13: Reproducible blue shift after several 20 K temperature cycles - Photoluminescence peak energy is plotted during three 20 K thermal cycles. Blue shift of about $170 \mu\text{eV}$ is induced every after 20 K cycles in a reproducible manner.

to the high energy-side but with a significant offset. The dramatic blue shift of the photoluminescence peak energy is about $170 \mu\text{eV}$, while the QD linewidth keeps the same value. Over several thermal cycles, this blue shift is induced by the same amount (see Fig. 4.13).

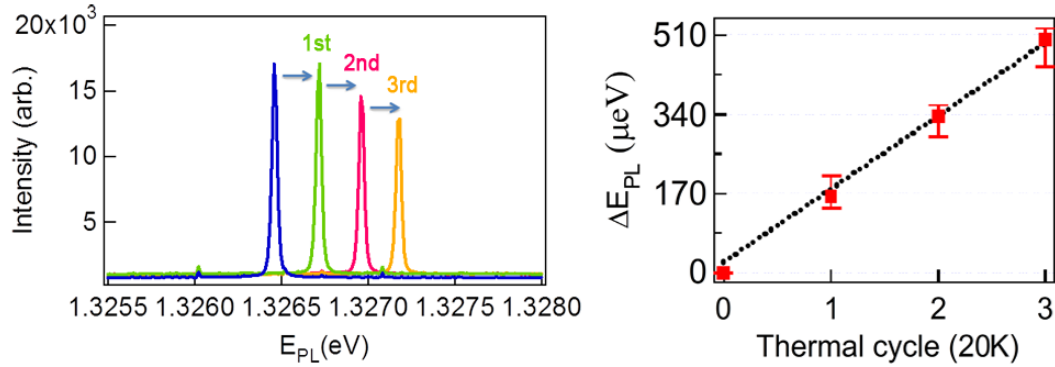


Figure 4.14: ΔE_{PL} versus time and 20 K temperature cycle for excitation power $P/P_{\text{sat}} = 0.2$ in a bare photonic wire - (a) Reproducible tuning scheme is presented for a single QD. Here, the integration time is 5 s. The QD is detuned by $170 \mu\text{eV}$ using 20 K thermal cycle. (b) QD shifts are displayed every after 20 K thermal cycles.

Here, the photoluminescence peak shows an overshoot (red shift) right after the recoiling process. About 5 min after the cycle, the photoluminescence peak settles to a certain emission energy. Indeed, the recovery requires a time for full thermalization of the environment around a wire as the sample is recooled to 4 K. After the full recovery, the QD emission energy keeps a stationary state during 20 min (see the plateau of E_{PL} in Fig. 4.12). This means that the diffusion of O_2 molecules reaches an equilibrium during this time. This stationary condition is independent of the laser illumination as shown in Fig. 4.12(a). Black circle denotes the photoluminescence peak positions measured with the laser illumination only before the data acquisition. With the comparison of the photoluminescence spectra under the continuous illumination (yellow trace), the black circle follows almost the same traces of the photoluminescence peak position. About the 30 min stationary condition after the 20 K cycle, the QD emission line starts to drift again.

The point here is that this process shows energetically reproducible change of spectral QD lines. Figure 4.13 plots the QD emission energy during several 20 K temperature cycles. As summarized in Fig. 4.14, almost the same blue shift of about $170 \mu\text{eV}$

4. SURFACE EFFECTS IN A SEMICONDUCTING PHOTONIC WIRE; SPECTRAL STABILITY OF AN EMBEDDED SINGLE QD

are observed by repeating four times of 20 K cycles. To get a better insight, Fig. 4.14(a) presents four photoluminescence spectra taken 5 min after each 20 K cycle. Almost the same linewidth and intensity in the QD emission line are observed with the repetitive blue shift of $170 \mu\text{eV}$. The reproducible giant blue shift tells us that the physisorption process during 20 K cycle dose not change the surface reaction dynamics on the photonic wire.

4.5 Chapter Summary

In this Chapter, we evidenced the influence of surface effects for InAs QDs embedded into trumpet-like GaAs photonic nanowires. A continuous temporal drift of the emission energy was observed and characterized in terms of excitation laser power and temperature. The temperature study revealed an adsorption peak of oxygen molecules on GaAs around 20 K (90, 93). We then attributed the drift to the sticking of oxygen molecules onto the wire, which modified the surface charge and hence the electric field seen by the quantum dot. We demonstrated a proper treatment of the nanowire surface to suppress the drift. After the surface passivation, the QD behaved as a stable two-level system embedded into an optical waveguide made by the photonic wire. The frequency stability of the emission of a single QD is crucial to perform high precision resonant spectroscopic studies. As an alternative approach, we utilized the position-dependent temporal drift to tune into resonance two different single QDs in a same bare photonic wire. In an one-dimensional waveguide, the resonance of two QDs is very promising for studying their cooperative effects as all QDs couple to a single mode of photonic wire. In the following Chapter 5, different strategy of QD tuning will also be discussed with the resonance of two different single QDs in a same wire.

5

Strain-induced optomechanical coupling for quantum dots in photonic wires

Nanomechanics requires very sensitive probing of the position. Hybrid system in which mechanical parameters are coupled to other degrees of freedom of the system such as electrical (97, 98), magnetic (99, 100, 101) or optical (102) are very promising devices towards the goal of sensing and controlling quantum motion. Moreover interfacing a mechanical oscillator with a single quantum object (97, 99, 103, 104) could open an avenue for the storage and/or processing of quantum information.

In this work, we have observed a spectral modulation of the photoluminescence of individual InAs quantum dots (QDs) embedded in an oscillating GaAs photonic wire. Strain-induced tuning of the excitonic transition and of the fine structure splitting of QDs has already been observed in a static way by stretching a thin membrane of semi-conductor directly glued on a piezoelectric transducer (105, 106, 107, 108) or dynamically with surface acoustic waves (109, 110). Our results show strain-mediated coupling between a nanomechanical oscillator and a single light emitter. This effect offers the possibility of stroboscopic QD tuning (109). In particular, we were able to bring in resonance two QDs located in the same wire. Additionally, the strength and the phase of this coupling allow the extraction of the QD location within the photonic wire with a sub-wavelength accuracy.

In fact, the GaAs photonic wire used in this work has been designed for efficient

5. STRAIN-INDUCED OPTOMECHANICAL COUPLING FOR QUANTUM DOTS IN PHOTONIC WIRES

single photon production (38). A large β -factor exceeding 90% has been achieved in this one-dimensional geometry over a broad wavelength range 70 nm centered at $\lambda = 950$ nm). As shown in Fig. 5.1, it is an inverted truncated cone with bottom and top diameters of 0.7 and 2.0 μm respectively, and a height of 18 μm . This geometry ensures an adiabatic broadening of the fundamental guided mode of the wire, and a highly directive radiation pattern on the purpose of the far-field optimization. Self-assembled InAs QDs (marked with yellow triangle) are located close to the bottom of the photonic nanowire, where the dynamical strain is rather large for the first flexural mode of the wire.

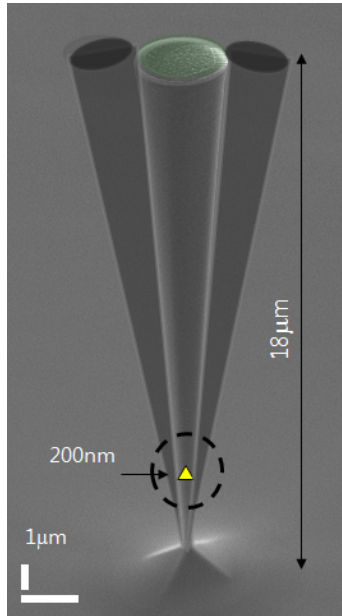


Figure 5.1: Dynamics of trumpet-like GaAs photonic wire embedding self-assembled InAs QDs - Schematics of oscillating wire is shown in an exaggerated way. The yellow triangles illustrate the InAs QDs. Self-assembled InAs QDs are embedded 3 μm above the bottom of the wire.

The mechanical oscillation is driven by a piezoelectric transducer attached at the back of the sample holder. The first flexural mode of the wire has a resonance frequency around 500 kHz and a quality factor of 870 at 4 K in vacuum. This oscillation induces a large dynamical stress on the QD, which modulates in turn the emitted photons energy.

In this Chapter, we will present a spectral broadening of the QD photoluminescence in the vertical photonic nanowires undergoing mechanical oscillations. We will show

how to tune the QD emission energy stroboscopically over a several hundred μeV range by varying the phase between the optical and mechanical excitations. The full time-dependent spectral lineshape will be reconstructed with a careful phase adjustment. In particular, we will dynamically bring two individual QDs into resonance, which are located in the same photonic wire but experiencing different strains. Additionally, the amplitude and phase dependence of the spectral oscillations allow inferring the position of the quantum dot within the photonic nanowire along the direction of the polarization of the mechanical mode. We will evidence a lifting of the two fold polarization degeneracy of the first flexural mode, due to a slight ellipticity of the photonic wire. Successive studies at the two resonance mechanical frequencies therefore allow us to obtain the complete two-dimensional position of embedded QDs.

5.1 Band Structure of InAs/GaAs System

To begin with, we describe a self-assembled InAs QD band structure. As discussed in Chapter 2, the formation of the self-assembled InAs QD structures is driven by an intrinsic elastic strain field arising from the lattice mismatch between the bulk lattice parameters of InAs (6.0584 Å) and GaAs (5.6533 Å). Electronic properties of the InAs QD are known to depend on the intrinsic strain field. In addition to the natural distortion, variable external stresses modify InAs band structures and thereby shift QD emission energies. This Chapter describes the external strain effects on QD emission properties and their usefulness for various purposes. To estimate the influence of the strain on QD emission properties, this section starts with describing the band structure of the InAs/GaAs system and outlines the phenomenological view of the strained band-gap deformation.

The InAs is a direct band-gap material whose conduction band minimum and valence band maximum are aligned at the Γ point ($k = 0$) in the first Brillouin zone. A schematic band diagram of bulk InAs is shown in Fig. 5.2(a) near the Γ point. Close to the band edges, the dispersion of the valence and conduction bands can be approximated by $E_V = E_V(\Gamma) - \hbar^2 k^2 / 2m_h^*$ and $E_C = E_C(\Gamma) + \hbar^2 k^2 / 2m_e^*$, where $m_{h(e)}^*$ can be either the effective mass of the heavy-hole (HH), light hole (LH) or electron. Their name comes from the difference in their effective masses. The effective mass of HH of $m_{HH}^* = 0.5m_0$ is indeed six times heavier than that of LH of $m_{LH}^* = 0.08m_0$. The

5. STRAIN-INDUCED OPTOMECHANICAL COUPLING FOR QUANTUM DOTS IN PHOTONIC WIRES

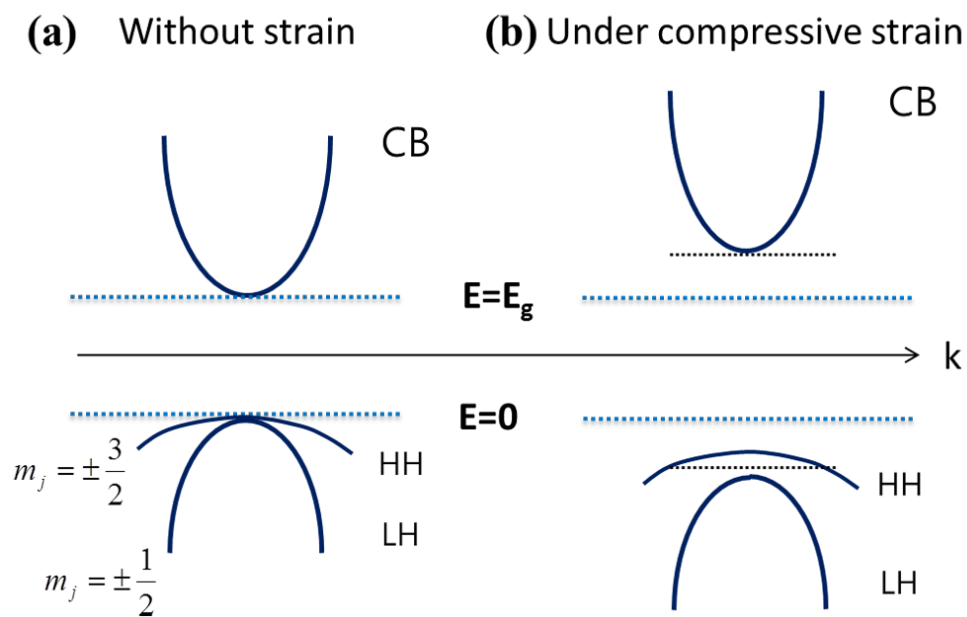


Figure 5.2: Strain effects on InAs system - Sketch shows the strain-induced band-edge deformation for (a) the unstrained InAs to (b) compressively strained InAs band structures in the momentum space \mathbf{k} . For unstrained bulk InAs band structures, valence bands of heavy hole (HH) and light hole (LH) are degenerate at the Γ point. The reference $E = 0$ is taken at the maximum of degenerate valence bands and the band-gap is denoted as E_g . Under an intrinsic compressive strain, two valence bands split apart so that the transition energy from the conduction band (CB) to the HH band corresponds to the fundamental band-gap.

5.1 Band Structure of InAs/GaAs System

two valence bands are energetically well-separated from the lowest conduction band by E_g at the Γ point. HH and LH bands exhibit p -like symmetry whose hole states are respectively $|\frac{3}{2}, \pm\frac{3}{2}\rangle$ and $|\frac{3}{2}, \pm\frac{1}{2}\rangle$ with the total angular momentum of $J = 3/2$. At Γ point, the conduction band has s-like states of $|\frac{1}{2}, \pm\frac{1}{2}\rangle$ with the total angular momentum of $J = 1/2$. The conduction band can occupy spin states of $|\pm\frac{1}{2}\rangle$. For a strain-free case of InAs semiconductor, Fig. 5.2(a) illustrates the two-fold degenerate s-like states of $|\frac{1}{2}, \pm\frac{1}{2}\rangle$ in the conduction band minimum, and the four-fold degenerate p-like states of $|\frac{3}{2}, \pm\frac{3}{2}\rangle$ and $|\frac{3}{2}, \pm\frac{1}{2}\rangle$ in the valence band structures.

Let's here speak first about the strain state of a two-dimensional layer of InAs (or InGaAs), pseudomorphically grown on GaAs (= no dislocation). For the QDs, the strain state depends on the QD shape and is much more complex in the general case. For InAs QDs, the shape is very flat, so it is reasonable, as a first approximation, to mimic the strain as biaxial (at least close to the center of the QD where the exciton is localized). Figure 5.2.(b) illustrates the strain-induced band-gap deformation of InAs under a compressive strain in InAs/GaAs system. Here, strain has two major effects on the InAs band-gap structure, shifting the band-gap energy and lifting the degeneracy of valence bands. Note that the InAs/GaAs system studied in this work is under an intrinsic in-plane compressive strain field owing to the InAs-GaAs lattice mismatch of 7%. This intrinsic compressive strain leads to a tensile strain along the [001] direction. Since the bulk lattice constant of InAs is larger than the one of GaAs, the InAs wetting layer is under the compression in the (001) direction. The intrinsic compressive strain is decomposed into a hydrostatic strain of $\epsilon_{uni} = -0.0611$ and a shear strain of $\epsilon_{sh} = 0.1396$ at the InAs/GaAs boundary (111). The shear component splits HH and LH valence bands by lifting the HH band and lowering the LH band. The HH state is, therefore, the highest valence band at the Γ point. The valence band splitting of HH and LH is seen by Fig. 5.2(b). Excitonic transitions are then dominated by the transition between the conduction band and the HH valence band. Turning to the hydrostatic component, the compressive hydrostatic strain increases the band-gap energy. The details of band-gap deformations are quantitatively described in the following section. 5.1.2.

5. STRAIN-INDUCED OPTOMECHANICAL COUPLING FOR QUANTUM DOTS IN PHOTONIC WIRES

5.1.1 $\mathbf{k} \cdot \mathbf{p}$ theory

To quantify the band line-up in strained-InAs structures, the $\mathbf{k} \cdot \mathbf{p}$ Hamiltonian (68, 112) is typically employed to calculate the electronic band structure in the vicinity of the Γ -point. The $\mathbf{k} \cdot \mathbf{p}$ perturbation theory is based on so-called ‘‘Bloch theorem’’. In the Bloch theorem, a particle is assumed to move in a periodic lattice potential $V(\mathbf{r}) = V(\mathbf{r} + \mathbf{R})$. The lattice periodicity is expressed in terms of a translational period $\mathbf{R}(= n_i a_i)$ with a set of primitive lattice vectors of a_i . Its wavefunction $\Psi(\mathbf{r})$ satisfies the *Schrödinger* equation of

$$H\Psi(\mathbf{r}) = \left(\frac{\hbar^2}{2m_0} \nabla^2 + V(\mathbf{r}) \right) \Psi(\mathbf{r}) = E(\mathbf{k})\Psi(\mathbf{r}). \quad (5.1)$$

The wavefunction referred to as Bloch function can be expressed in a form of

$$\Psi(\mathbf{r})_{nk} = \exp(i\mathbf{k} \cdot \mathbf{r})u(\mathbf{k}, \mathbf{r}) \quad (5.2)$$

where $u(\mathbf{k}, \mathbf{r})$ is the Bloch lattice function and the integer n denotes the band. The Bloch lattice functions $u(\mathbf{k}, \mathbf{r}) = u(\mathbf{k}, \mathbf{r}) + u(\mathbf{k}, \mathbf{R})$ are invariant under the translational period by \mathbf{R} . The periodic Bloch function $u(\mathbf{k}, \mathbf{r})$ satisfies the *Schrödinger*-like equation of

$$\left(\frac{p^2}{2m_0} + V(\mathbf{r}) + \frac{\hbar\mathbf{k} \cdot \mathbf{p}}{m_0} \right) u_{n,\mathbf{k}}(\mathbf{r}) = \left(E_{n,\mathbf{k}} - \frac{\hbar^2\mathbf{k}^2}{2m_0} \right) u_{n,\mathbf{k}}(\mathbf{r}). \quad (5.3)$$

Here, the term of $H' = \frac{\hbar^2\mathbf{k}^2}{2m} + \frac{\hbar\mathbf{k} \cdot \mathbf{p}}{m}$ corresponds to the perturbation.

Near the Γ -point, the $\mathbf{k} \cdot \mathbf{p}$ perturbation theory results in

$$u_{n,\mathbf{k}}(\mathbf{r}) = u_{n,\mathbf{0}}(\mathbf{r}) + \frac{\hbar}{m_0} \sum_{n' \neq n} \frac{\langle u_{n,\mathbf{0}} | \mathbf{k} \cdot \mathbf{p} | u_{n',\mathbf{0}} \rangle}{E_{n,\mathbf{0}}(\mathbf{r}) - E_{n',\mathbf{0}}(\mathbf{r})} u_{n',\mathbf{0}}(\mathbf{r}) \quad (5.4)$$

$$E_n(\mathbf{k}) = E_n(0) + \frac{\hbar^2}{m_0^2} \sum_{n' \neq n} \frac{|\langle u_{n,\mathbf{0}} | \mathbf{k} \cdot \mathbf{p} | u_{n',\mathbf{0}} \rangle|^2}{E_{n,\mathbf{0}}(\mathbf{r}) - E_{n',\mathbf{0}}(\mathbf{r})}. \quad (5.5)$$

Equation (5.5) is an introductory example for describing a Bloch state and its energy in a single band. For multiple band structure study, the Pikus-Bir Hamiltonian based on the $\mathbf{k} \cdot \mathbf{p}$ perturbation theory will be taken into account in the following section. By diagonalizing the matrix obtained with the six-band $\mathbf{k} \cdot \mathbf{p}$ perturbation theory, we can calculate the strain-induced spectral shift of InAs QD excitons in a GaAs photonic wire.

5.1.2 Influence of Stress on InAs/GaAs Structures

Modeling of elastic solid bodies is a branch of mechanics that deals with the stress σ on a deformed body and its strain ε based on the Hooke's law (Force=spring constant \times displacement). In this work dealing with a GaAs photonic wire, stress σ can be defined as the force per unit cross-sectional area of the photonic wire. Strain is then defined as the relative change of the lattice parameters x by an amount of $\varepsilon = \frac{\delta x}{x}$ induced by the stress σ .

Figure 5.3 illustrates an arbitrary deformation of a cubic lattice due to the strain. As illustrated in Fig. 5.3, the unstrained unit cell with a unit vector \mathbf{r} transforms to a strained unit cell with strained lattice vector \mathbf{r}' . The strained lattice vector \mathbf{r}' can be written in terms of unstrained lattice unit vectors $\mathbf{r}(x, y, z)$ and the strain tensor ε_{ij} of the crystal:

$$\begin{pmatrix} x' \\ y' \\ z' \end{pmatrix} = \begin{pmatrix} 1 + \varepsilon_{xx} & \varepsilon_{xy} & \varepsilon_{xz} \\ \varepsilon_{yx} & 1 + \varepsilon_{yy} & \varepsilon_{yz} \\ \varepsilon_{zx} & \varepsilon_{zy} & 1 + \varepsilon_{zz} \end{pmatrix} \begin{pmatrix} x \\ y \\ z \end{pmatrix}.$$

Here, the strain tensor ε_{ij} can be decomposed into the sum of two matrices, the hydrostatic strain and the distortion term:

$$\varepsilon = \underbrace{\frac{1}{3} \begin{pmatrix} \Delta & 0 & 0 \\ 0 & \Delta & 0 \\ 0 & 0 & \Delta \end{pmatrix}}_{\text{Hydrostatic strain}} + \underbrace{\begin{pmatrix} \varepsilon_{xx} - \frac{\Delta}{3} & \varepsilon_{xy} & \varepsilon_{xz} \\ \varepsilon_{xy} & 1 + \varepsilon_{yy} - \frac{\Delta}{3} & \varepsilon_{yz} \\ \varepsilon_{xz} & \varepsilon_{yz} & 1 + \varepsilon_{zz} - \frac{\Delta}{3} \end{pmatrix}}_{\text{Distortion strain}}$$

where $\Delta = \varepsilon_{xx} + \varepsilon_{yy} + \varepsilon_{zz}$ is the trace of the strain tensor. Here, the first hydrostatic part describes the fractional change of volume ($\delta V/V$) under the uniform deformation. The second matrix, so-called the distortion strain term, describes the shear deformation of the medium. Such strains in a crystal can induce a considerable modification in the energy levels of conduction and valence bands. The hydrostatic strain is known to add an offset to a conventional band-gap, while the shear strain lifts the degeneracy of HH and LH bands.

5.1.2.1 Pikus-Bir Hamiltonian for Bulk Semiconductors

The effect of strain on the electronic band structure has been comprehensively studied by Bir and Pikus (113). The strain-induced shift in the energy levels of the conduction

5. STRAIN-INDUCED OPTOMECHANICAL COUPLING FOR QUANTUM DOTS IN PHOTONIC WIRES

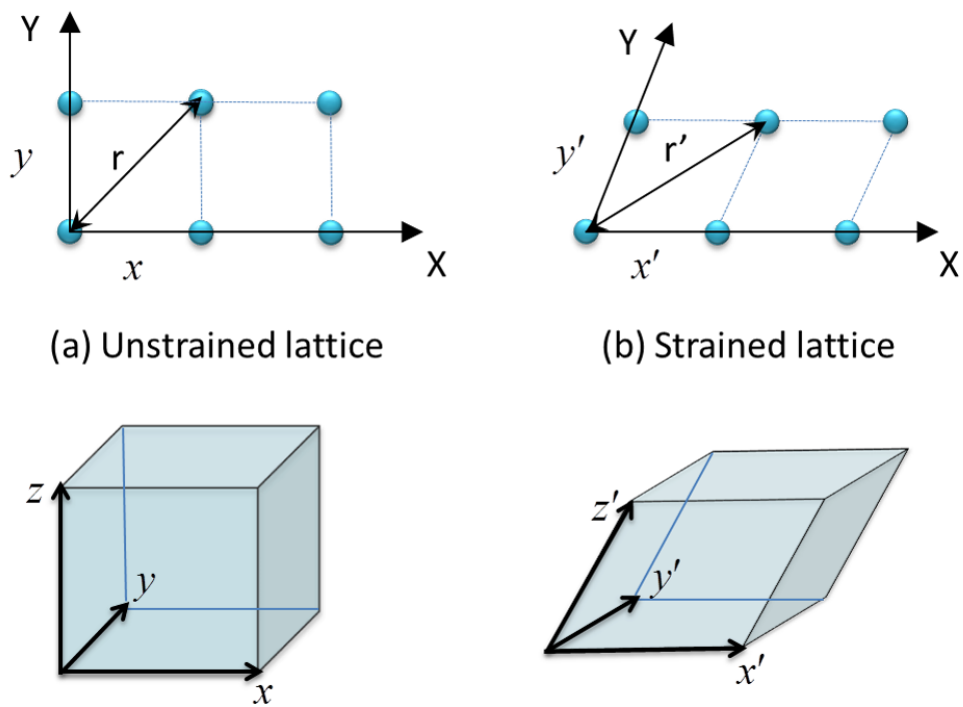


Figure 5.3: Deformation of crystal from the unstrained lattice (a) to the strained lattice (b) - When the strain is applied, the unstrained lattice vectors x, y, z transform to the strained lattice vectors x', y', z' .

5.1 Band Structure of InAs/GaAs System

and valence bands is incorporated into band structure calculations using the $\mathbf{k} \cdot \mathbf{p}$ Pikus-Bir Hamiltonian. The Pikus-Bir effective strain Hamiltonian for the $J = 3/2$ valence bands in zinc-blende semiconductors is given by (68, 113, 114)

$$\mathbf{H}_{\text{PB}} = \overbrace{\begin{pmatrix} P_k + Q_k & -S_k & R_k & 0 \\ -S_k^* & P_k - Q_k & 0 & R_k \\ R_k^* & 0 & P_k - Q_k & S_k \\ 0 & R_k^* & S_k^* & P_k + Q_k \end{pmatrix}}^{\text{Kinetic energy}} + \overbrace{\begin{pmatrix} P_\varepsilon + Q_\varepsilon & -S_\varepsilon & R_\varepsilon & 0 \\ -S_\varepsilon^* & P_\varepsilon - Q_\varepsilon & 0 & R_\varepsilon \\ R_\varepsilon^* & 0 & P_\varepsilon - Q_\varepsilon & S_\varepsilon \\ 0 & R_\varepsilon^* & S_\varepsilon^* & P_\varepsilon + Q_\varepsilon \end{pmatrix}}^{\text{Strain contribution}}$$

in the basis states of HH and LH $|\frac{3}{2}, \frac{3}{2}\rangle, |\frac{3}{2}, \frac{1}{2}\rangle, |\frac{3}{2}, -\frac{1}{2}\rangle, |\frac{3}{2}, -\frac{3}{2}\rangle$.

The kinetic energy is characterized in the first matrix with elements of

$$P_k = \frac{\hbar^2 \gamma_1}{2m_0} \mathbf{k}^2, \quad Q_k = \frac{\hbar^2 \gamma_2}{2m_0} (k_y^2 + k_y^2 - 2k_z^2), \quad (5.6)$$

$$R_k = \frac{\hbar^2}{2m_0} \left[-\sqrt{3} \gamma_2 (k_x^2 - k_y^2) + i2\sqrt{3} \gamma_2 k_x k_y \right], \quad \text{and} \quad S_k = \frac{\hbar^2 \gamma_3}{m_0} \sqrt{3} (k_x - ik_y) k_z. \quad (5.7)$$

Here, γ_1 , γ_2 and γ_3 are material dependent constants.

The second matrix characterizes the influence of an arbitrary strain on HH and LH valence band structures with elements of

$$P_\varepsilon = -a_\varepsilon (\varepsilon_{xx} + \varepsilon_{yy} + \varepsilon_{zz}), \quad (5.8)$$

$$Q_\varepsilon = -\frac{b}{2} (\varepsilon_{xx} + \varepsilon_{yy} - 2\varepsilon_{zz}), \quad (5.9)$$

$$R_\varepsilon = \frac{\sqrt{3}b}{2} (\varepsilon_{xx} - \varepsilon_{yy}) - id\varepsilon_{xy}, \quad \text{and} \quad (5.10)$$

$$S_\varepsilon = -d(\varepsilon_{xz} - i\varepsilon_{yz}). \quad (5.11)$$

Here, there is a one-to-one correspondence between elements in two matrices (115);

$$\frac{\hbar^2 \gamma_1}{2m_0} \leftrightarrow -a_\varepsilon, \quad \frac{\hbar^2 \gamma_2}{2m_0} \leftrightarrow -\frac{b}{2}, \quad \frac{\hbar^2 \gamma_3}{2m_0} \leftrightarrow d, \quad (5.12)$$

$$k_i k_j \leftrightarrow \varepsilon_{ij}, \quad i, j = x, y, z. \quad (5.13)$$

In this work, the major direction is to characterize a self-assembled InAs QD grown on [001] GaAs substrate under an external uniaxial stress along the [001]-direction. In the following subsection, we will first describe the influence of intrinsic stress on InAs band structures.

5. STRAIN-INDUCED OPTOMECHANICAL COUPLING FOR QUANTUM DOTS IN PHOTONIC WIRES

5.1.2.2 Influence of Intrinsic Stress on InAs/GaAs Structure

As we mentioned before, the strain tensor for InAs QDs can be approximated by a special case of biaxial strain. For the intrinsic lattice mismatched strain (116), the strain tensor is simplified as

$$\begin{aligned}\varepsilon_{xx} = \varepsilon_{yy} &= \frac{\Delta a (= a_0 - a)}{a} \\ \varepsilon_{zz} &= -\frac{2C_{12}}{C_{11}}\varepsilon_{xx} \\ \varepsilon_{xy} = \varepsilon_{yz} = \varepsilon_{zx} &= 0.\end{aligned}$$

Here, a_0 and a denote the lattice constants respectively of GaAs and InAs materials and C_{11} and C_{12} are elastic coefficients. Therefore, R_ε and S_ε go to zero.

Since the InAs/GaAs QD is a direct bandgap semiconductor system, here we only focus on the band edge dispersion at the Γ point. When $\mathbf{k} = 0$ (Γ point), energies of strained valence bands from the Pikus-Bir Hamiltonian H_{PB} are reduced into simple forms of

$$\begin{aligned}E_{HH}(k=0) &= -(P_\varepsilon + Q_\varepsilon) = a_\nu(\varepsilon_{xx} + \varepsilon_{yy} + \varepsilon_{zz}) + \frac{b}{2}(\varepsilon_{xx} + \varepsilon_{yy} - 2\varepsilon_{zz}) \\ E_{LH}(k=0) &= -(P_\varepsilon - Q_\varepsilon) = a_\nu(\varepsilon_{xx} + \varepsilon_{yy} + \varepsilon_{zz}) - \frac{b}{2}(\varepsilon_{xx} + \varepsilon_{yy} - 2\varepsilon_{zz}).\end{aligned}\quad (5.14)$$

Energy of the conduction band is also given by the diagonalization of the Pikus-Bir effective Hamiltonian in basis states of $|\frac{1}{2}, \pm\frac{1}{2}\rangle$. The strained energy in the conduction band read as

$$E_c = E_g + a_c(\varepsilon_{xx} + \varepsilon_{yy} + \varepsilon_{zz}) \quad (5.15)$$

with the deformation potential of the conduction band $a_c (= \hbar^2/2m_{e^*})$ and the band-gap energy E_g . Setting the hydrostatic deformation potential as $a = a_c - a_\nu$, strain-induced energy shifts at the Γ point can then be given by

$$\begin{aligned}E_{C-HH}(k=0) &= E_g + a(\varepsilon_{xx} + \varepsilon_{yy} + \varepsilon_{zz}) - \frac{b}{2}(\varepsilon_{xx} + \varepsilon_{yy} - 2\varepsilon_{zz}) \\ &= E_g - \delta E_{hy} + \frac{1}{2}\delta E_{sh}\end{aligned}\quad (5.16)$$

$$\begin{aligned}E_{C-LH}(k=0) &= E_g + a(\varepsilon_{xx} + \varepsilon_{yy} + \varepsilon_{zz}) + \frac{b}{2}(\varepsilon_{xx} + \varepsilon_{yy} - 2\varepsilon_{zz}), \\ &= E_g - \delta E_{hy} - \frac{1}{2}\delta E_{sh}.\end{aligned}\quad (5.17)$$

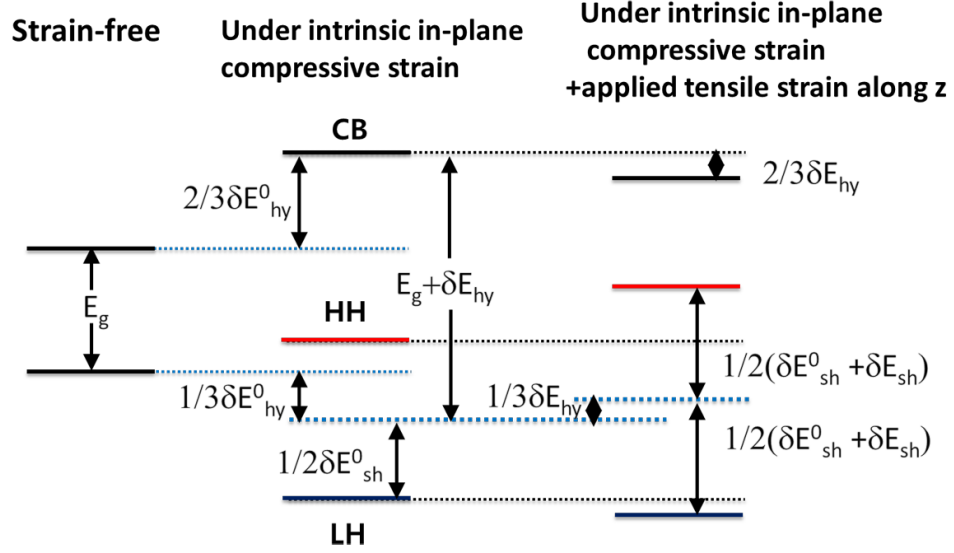


Figure 5.4: Strain-induced modification in InAs band structures - Simplified level scheme of Zinc Blende crystal structure semiconductor is shown for an unstrained, an intrinsically strained (compressive in plans and therefore tensile along z), and an extrinsically strained lattice (under tensile strain in the z direction).

From Eqs.(5.16) and (5.17), the hydrostatic strain shifts all the valleys of conduction and valence bands, which leads to increase the band-gap energy by $\delta E_{hy} [= -a(\varepsilon_{xx} + \varepsilon_{yy} + \varepsilon_{zz})]$. Shear strain splits the HH and LH bands by $\delta E_{sh} [= -b(\varepsilon_{xx} + \varepsilon_{yy} - 2\varepsilon_{zz})]$.

Concerning the relevant case of an InAs/GaAs matrix, our InAs QDs are under the compressive strain owing to the InAs-GaAs lattice mismatch. Figure 5.4 illustrates how hydrostatic and shear stresses shift energy levels in the InAs band structure. Followed by the partition rule for the deformation potential (117, 118), the hydrostatic energy is distributed by the upward shift of the conduction band by $\frac{2}{3}\delta E_{hy}$ and the downward shift of the HH band by $\frac{1}{3}\delta E_{hy}$. Then, the lowest energy hole state is the HH state.

5.1.2.3 Influence of an Applied Uniaxial Stress on InAs/GaAs Structure

In addition to the intrinsic strain, we calculate the influence of an external uniaxial stress on InAs band structures. We assume an applied uniaxial stress \mathbf{X} along the [001]-direction. The strain components parallel to [001] are then given by

$$\varepsilon_{xx} = \varepsilon_{yy} = S_{12}X, \quad \varepsilon_{zz} = S_{11}X, \quad \varepsilon_{xy} = \varepsilon_{xz} = \varepsilon_{yz} = 0. \quad (5.18)$$

5. STRAIN-INDUCED OPTOMECHANICAL COUPLING FOR QUANTUM DOTS IN PHOTONIC WIRES

In the case of a InAs QD embedded in a GaAs matrix, the strain experienced by the QD is imposed by the GaAs matrix so we should therefore use the S_{11} and S_{12} mechanical parameters of GaAs. We give below the transition energy shifts δE_{C-HH} (resp. δE_{C-LH}) from heavy hole (resp. light hole) to the conduction band for InAs:

$$\delta E_{C-HH} = a(S_{11} + 2S_{12})\mathbf{X} + b(S_{11} - S_{12})\mathbf{X} \quad (5.19)$$

$$= -5.32\text{meV/kbar} \times \mathbf{X} \quad \text{and} \quad (5.20)$$

$$\delta E_{C-LH} = a(S_{11} + 2S_{12})\mathbf{X} - b(S_{11} - S_{12})\mathbf{X} \quad (5.21)$$

$$= 0.04\text{meV/kbar} \times \mathbf{X} \quad (5.22)$$

and for GaAs

$$\delta E_{C-HH} = a(S_{11} + 2S_{12})\mathbf{X} + b(S_{11} - S_{12})\mathbf{X} \quad (5.23)$$

$$= -6.94\text{meV/kbar} \times \mathbf{X} \quad \text{and} \quad (5.24)$$

$$\delta E_{C-LH} = a(S_{11} + 2S_{12})\mathbf{X} - b(S_{11} - S_{12})\mathbf{X} \quad (5.25)$$

$$= 0.98\text{meV/kbar} \times \mathbf{X} \quad (5.26)$$

with coefficients of the four-rank strain tensor $S_{11} = \frac{C_{11}+C_{12}}{(C_{11}-C_{12})(C_{11}+2C_{12})}$ and $S_{12} = -\frac{C_{12}}{(C_{11}-C_{12})(C_{11}+2C_{12})}$. Note that positive values for stress (strain) correspond to tensile stress (strain). Material parameters used in this calculation are tabulated in Table 5.1. The relevant transition for the photoluminescence experiment carried out in this work is that of the lowest energy involving the heavy hole (C-HH). This means that an additional tensile strain of 1 kbar along the z direction leads to a InAs band gap reduction with a shift 5.32 meV/kbar. Strain-dependent shift of δE_{C-LH} is also given by 0.04 meV/kbar under an additional compressive strain. In the following sections, we will disregard the shift δE_{C-LH} in the LH valence band since the LH valence band is a higher state.

5.1.2.4 Other Effects of Strain on QD Confinement Potential Well

In addition to hydrostatic and biaxial strains, a change of the QD height and the depth of the confinement potential affect the QD excitonic energy. As a relevant case in our work, a single QD undergoes an external uniaxial stress along the z-direction. Under the stress, the QD confinement potential will change accompanied by a change in the height of QD. More precisely, if the uniaxial compressive stress pushes down a dot,

5.1 Band Structure of InAs/GaAs System

InAs material parameters (T=5K)	value	Unit
a	-6	eV
b	-1.8	eV
GaAs material parameters		
a	-9	eV
b	-2	eV
GaAs mechanical parameters		
C_{11}	833	$kbar$
C_{12}	453	$kbar$
S_{11}	1.14×10^{-3}	$kbar^{-1}$
S_{12}	-0.35×10^{-3}	$kbar^{-1}$

Table 5.1: InAs material parameters used in calculations

the QD height decreases resulting in the increase of the confinement energy. The QD excitonic energy is then blue-shifted. When the uniaxial tensile stress pulls up the dot, increasing height of the dot reduces the confinement energy, thereby a red-shifted excitonic energy.

In order to estimate the strain effect in the simplest way, we approximate the real confinement potential in InAs QDs as an infinite rectangular potential well. Figure 5.5 describes an infinite potential well for InAs QD having the height of L_z . The first state of the potential well corresponds to the confinement energy $E_c^0 = 945$ meV in our InAs/GaAs QD system. In real life, the QD potential well is finite but our assumption is still available to give a rough order of the magnitude. The simple approximation and its relevance have already been discussed in Chapter 2. Here, the photoluminescence excitonic energy E_{PL} is at around 1360 meV and the InAs band-gap energy E_g is 415 meV at 4 K. Strain-dependent confinement energy is then simply derived by

$$\delta E_c = -2E_c^0 \times S_{11} \times \mathbf{X} = -2.2meV/kbar \times \mathbf{X}. \quad (5.27)$$

With this choice of parameters, a compressive stress will increase the confinement energy by 2.2 meV/kbar.

In reality, the depth of the confinement potential, however, strongly depends on the composition of each single QD. In fact, there is a composition gradient in our

5. STRAIN-INDUCED OPTOMECHANICAL COUPLING FOR QUANTUM DOTS IN PHOTONIC WIRES

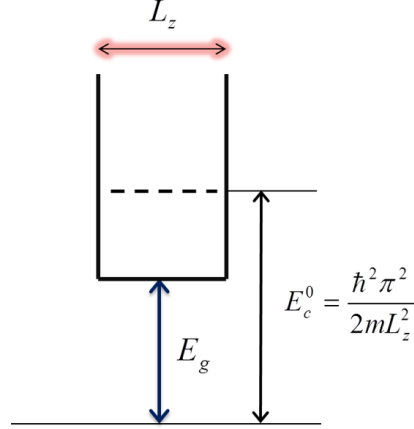


Figure 5.5: Schematic diagram of an infinite QD potential well - Infinite potential well is illustrated with the confinement energy E_c^0 of the fundamental state and the band-gap E_g of InAs QD of the height L_z .

system, with a higher *In* composition at the top of the QD. The bulk alloy is defined by $Ga_xIn_{1-x}As$ with the Ga mole fraction x . In our structure, the *In* composition is found to be smaller than 100%, but is still larger than 50 ~ 60% ($x \lesssim 0.5$) (119, 120, 121). Due to the intermixing of Ga into the InAs QD, the depth of the confinement potential well is rewritten for $Ga_xIn_{1-x}As$ by

$$\delta E_c = -2S_{11} \times [1360 - (410 + 634 \times x + 450x^2)]meV/kbar \times \mathbf{X}. \quad (5.28)$$

Since the percentage of a Ga intermixing into the InAs is maximally about 50% ($x=0.5$), we can simply compare the pressure dependence of the confinement potential between InAs and $Ga_{0.5}In_{0.5}As$ QDs. For a mixed structure $Ga_{0.5}In_{0.5}As$ ($x=0.5$), the well depth is reduced as 514 meV and its pressure dependence follows 1.21 meV/kbar. To give an order of magnitude, there is 55% reduction in its pressure dependence comparing to that of the pure InAs.

Here, the *In* composition profile is specific to each individual QD and a precise quantitative computation of the spectral shift caused by an applied stress is therefore not possible. However, the *In* composition profile is expected to depend only on the size of the island or capped QD for given growth conditions. The composition profile seems to be uniform from dot to dot since the island buildup and intermixing are driven by the quest for minimization of the free energy in the system.

5.1 Band Structure of InAs/GaAs System

In fact, we may too simplify the above calculation by neglecting a strain-induced effective mass change. When we have a large confinement, the strain-induced change in the effective mass is probably not negligible. By solving Eq. 5.5, the tensor of the reciprocal effective mass can be given by

$$E_n(\mathbf{k}) - E_n(0) = \frac{\hbar^2}{2} \sum_{\alpha,\beta} \left(\frac{1}{m^*} \right)_{\alpha,\beta} k_\alpha k_\beta \quad (5.29)$$

As seen in Eq.(5.29), the effective mass depends on a strain-induced shift of the band edge energy. For zinc-blende-type bulk semiconductors, the effective mass can be approximated by (68)

$$\frac{m_e}{m_e^*} = \frac{2}{m_e E_c} \left(\frac{2\pi\hbar}{a_0} \right)^2. \quad (5.30)$$

Concerning the realistic value of strain ($\Delta a/a$) not more than 8.8×10^{-6} for a 1 nm top displacement in our system, we can approximate the variation of the effective mass as

$$dm_e^* = \frac{\Delta E_c}{E_c} m_e^* \quad (5.31)$$

where the band-gap is shifted by ΔE_c under an additional uniaxial stress. As a first estimate, a strain-mediated QD energy shift of few hundred μeV would induce less than 1% change in the effective mass, which leads to not more than 1% change in our numerical calculation. Certainly, this discussion just gives a very rough estimation. As shown in the previous calculation using Eq.(5.28), we didn't even consider the strain modified InAs effective masses under an intrinsic strain field.

To summarize discussions of the section 5.1.2, InAs band-gap is modified by following parameters

- Uniaxial compressive stress : $\kappa_{uni}=5.32$ meV/kbar
- Effect of a compressive stress on QD Confinement Potential Well : $\kappa_{con}=2.2$ meV/kbar
- InAs QD with an intermixing of Ga atoms can give an error bar of κ_{mixing} up to 55% in κ_{con} : 1.21 meV/kbar $\leq \kappa_{con} \leq 2.2$ meV/kbar.

In total, the InAs band-gap increases by

$$\Delta E_{InAs}/\mathbf{X} = 6.5 \sim 7.5 \text{ meV/kbar} \quad (5.32)$$

5. STRAIN-INDUCED OPTOMECHANICAL COUPLING FOR QUANTUM DOTS IN PHOTONIC WIRES

under an additional compressive strain. In a pure InAs QD, an additional compressive stress modifies the band-gap by 7.5 meV/kbar. Yet there is an uncertainty of QD height ($2 \sim 3nm$). Here, we have to admit that the strain effect on the band-gap deformation estimated here is relatively rough. The relevant shift for the band gap is somewhere between the InAs and the GaAs bandgap shift. Moreover the position between these two values depend also on a eventual intermixing of Ga in the QD. From the literature, the composition of the QD is rather $Ga_xIn_{1-x}As$ with $x \sim 0.5$. So we can take $\delta E_{C-HH}/\mathbf{X} = -6.5$ meV/kbar. We are aware that the calculated shift due to the change of the QD height is a rather rough approximation and is probably overestimated, since the real potential is not squared and far from being infinite. We can take $\delta E_c/\mathbf{X} \sim -1$ meV/kbar. It will be seen later that the total shift we obtain from these theoretical considerations is around $\delta E_{QD}/\mathbf{X} = 7.5$ meV/kbar compared to an experimental value of ~ 16 meV/kbar.

5.2 Strain Effect on Oscillating GaAs Photonic Wires Embedding InAs QDs

Based on previous calculations of GaAs band structures, this section describes more relevant cases of vibrating GaAs photonic wires embedding InAs QDs.

5.2.1 Flexural Eigenmodes

As shown in Chapter 2, the geometry considered here for the opto-mechanical resonator is the vertical GaAs photonic nanowire. The photonic wire can act as a simply clamped nano-sized mechanical oscillator, since the GaAs photonic nanowire is sufficiently long of length $17 \mu m$ over diameter of few hundred nanometer. Its dynamics can thus be modeled by the Euler-Bernoulli equation, simulating the wire as a simple Euler rod. Shear deformation and rotation are then negligible within the bending wire. Here, we assume a perfectly cylindrical wire. Considering only transverse deformations of a photonic wire, Euler-Bernoulli equation is given by (122, 123)

$$-YI \frac{\partial^4 U(z, t)}{\partial z^4} = \rho A \frac{\partial^2 U(z, t)}{\partial t^2} \quad (5.33)$$

5.2 Strain Effect on Oscillating GaAs Photonic Wires Embedding InAs QDs

with the Young modulus Y , the area moment of inertia I , the mass density ρ and the cross-sectional area of the wire A . Here, $U(z)$ denotes the deflection of a vibrating wire from the equilibrium axis z along the wire.

The stationary solution of this fourth-order partial differential equation can be written by

$$U(z) = A_n \cos(k_n z) + B_n \sin(k_n z) + C_n \cosh(k_n z) + D_n \sinh(k_n z). \quad (5.34)$$

Here, the stationary solution must satisfy following boundary conditions:

- $U(0) = 0, U'(0) = 0$ no deflection and slope at the fixed end ($z = 0$) due to the clamping
- $U''(L) = 0, U'''(L) = 0$ no bending moment and shearing force at the free end ($z = L$)

Then, the wavenumber k_n takes particular values only if $\cos(k_n L) \cosh(k_n L) = -1$ is satisfied.

Supplemented by these boundary conditions at wire ends, resonant frequencies of all mechanical eigenmodes of the cylindrical photonic wire are given by

$$\omega = k_n^2 \sqrt{\frac{YI}{\rho A}} = k_n^2 \sqrt{\frac{Y A^2}{12\rho(1-p^2)}}. \quad (5.35)$$

From this Eq.(5.35), the resonant frequency of a GaAs photonic wire can be estimated, for typical dimensions $L = 17.2 \mu\text{m}$ for the height and $D_{QD} = 720 \text{ nm}$ for the diameter. Here, the Young modulus Y is 85.5 GPa, Poisson's ratio p is 0.31 and the density ρ is 5320 kgm^{-3} .

To get a rough estimate, we first calculate the mechanical eigenmodes of a cylindrical wire. Using the Mathematica program, we get 499 kHz eigenfrequency of the wire having $D_{QD} = 720 \text{ nm}$ for the mechanical eigenvalue $k_n L$ of 1726. As discussed in Chapter 2, a non-isotropic dry etching would induce an asymmetry in the wire's diameter. For the same eigenmode $k_n L = 1726$, we compare two different wires having 672 nm and 720 nm radii. Reducing the radius from 720 nm by 24 nm induces a eigenfrequency shift from 498.99 kHz to 435 kHz. It means that a slight change in the etching angle by 0.1° and thereby the reduction of 24 nm in radius at the QD level

5. STRAIN-INDUCED OPTOMECHANICAL COUPLING FOR QUANTUM DOTS IN PHOTONIC WIRES

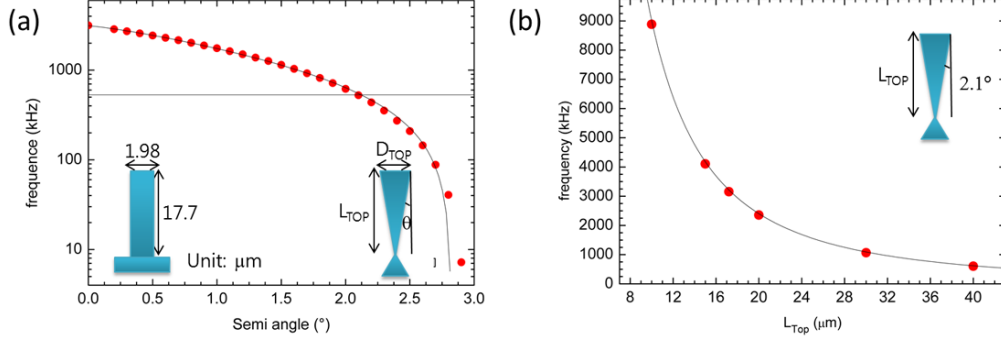


Figure 5.6: Simulated eigenfrequency of GaAs photonic wires - (a) Dependence of the resonance frequency of the wire on its geometry for a trumpet-like photonic wire defined by the etching angle θ . (b) Mechanical resonance frequency as a function of the wire height L_{Top} for an etching angle of 2.1° .

could shift the mechanical eigenfrequency by nearly 68 kHz. We will encounter the value of mechanical frequency in our experimental data later on.

Using a finite element simulation software, the comsol multiphysics program, we numerically calculate more realistic mechanical values for trumpet-like photonic wires. Figure 5.6 shows the trumpet angle dependence of simulated eigenfrequency on a GaAs photonic wire based on its designed size of $D_{Top} \sim 1.98 \mu\text{m}$. The etching angle is varied from 0° to 3° by providing a symmetrical cylinder as well as an inverted conical shape with $L_{Top} = 17.7 \mu\text{m}$ and $D_{Top} \sim 1.98 \mu\text{m}$. Here, L_{Top} denotes the distance from the top to the joint. The dependence of eigenfrequencies on wire's geometry and shape is shown in Fig. 5.6(a). Increasing the etching angle θ up to 3° , the resonant frequency reads as

$$f_{res} = -791 + \frac{3340}{1 + (\theta[^\circ]/2)^{2.5}} \quad (5.36)$$

for the wire of $D_{Top} \sim 1.98 \mu\text{m}$. While the cylindrical wire has its resonance at 3 MHz, the inverted GaAs photonic wires have their mechanical resonances in the $429 \sim 513 \text{ kHz}$ of range for etching angles varying between $2.35 \sim 2.5$.

As will be shown later, fundamental flexural modes of the wire are experimentally found to be 435 and 503 kHz for an etching angle of around 2.1° for a wire of $D_{Top} \sim 1.98 \mu\text{m}$. Our numerical calculation estimates the eigenfrequencies of 429 and 513 kHz respectively for etching angles 2.5° and 2.4° . Concerning the fact that the

5.2 Strain Effect on Oscillating GaAs Photonic Wires Embedding InAs QDs

dry etching process can easily be non-isotropic, we can have a slight ellipticity of the photonic wire. Therefore nondegenerate eigenfrequencies of the wire with 90 kHz spacing can be induced by non-isotropic etching within 0.1° error bar. Here, we don't really attack to match the realistic trumpet angle with 0.1° accuracy since there are uncertainties in their dimensions, for example L_{Top} and the vertical position of the QD plane. To get a rough estimate of the uncertainty in L_{Top} , we first simulate the resonant frequency by varying L_{Top} for the etching angle 2.1° as given in Fig. 5.6. The higher the wire, the faster its vibration. The vibrational mode is analytically expressed by $f_{res} = -235 + \frac{6883}{1+(L_{Top}[\mu\text{m}]/11)^4}$. If the wire height is lower by $0.2 \mu\text{m}$ from $17.7 \mu\text{m}$, the resonance frequency is higher by 35 kHz.

5.2.2 Strain-field Coupling Strength with QDs

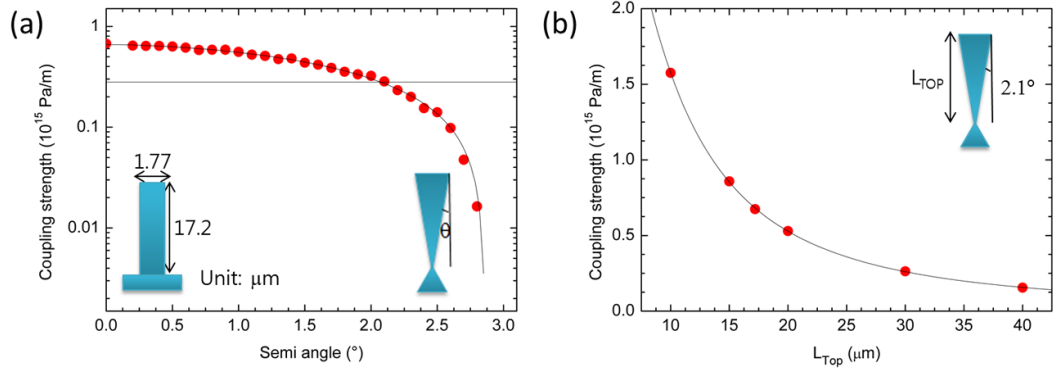


Figure 5.7: Simulated eigenfrequency of GaAs photonic wires - (a) Coupling strength parameter as a function of the etching angle θ for a photonic wire having $L_{Top} = 17.2 \mu\text{m}$ and $D_{Top} \sim 1.77 \mu\text{m}$ and (b) the height of the wire L_{Top} for a wire etched with a fixed angle 2.1° .

The mechanical excitation frequency has been studied for realistic wire parameters in the previous section. Still the coupling strength is required to describe the influence of strain-field on QDs embedded in the vibrating GaAs photonic wire. More precisely, the coupling strength informs us about the maximum stress in the QD plane when the wire moves laterally by x in meter scales. Figure 5.7 shows that the coupling strength between QDs and the strain-field depends on the shape and size of the trumpet-like photonic wire. The maximum coupling strength C_{st} of the QDs reads in terms of

5. STRAIN-INDUCED OPTOMECHANICAL COUPLING FOR QUANTUM DOTS IN PHOTONIC WIRES

etching angle θ as $C_{st}(10^{15} Pa/m) = -37.9 + \frac{38.6}{1+(\theta[^\circ]/30)^{1.7}}$. At the trumpet etching angle 2.1° , the coupling strength of the QDs can further be stronger in a shorter wire, followed by the relation $C_{st}(10^{15} Pa/m) = 0.009 + \frac{5.9}{1+(L_{Top}[\mu m]/5.9)^2}$.

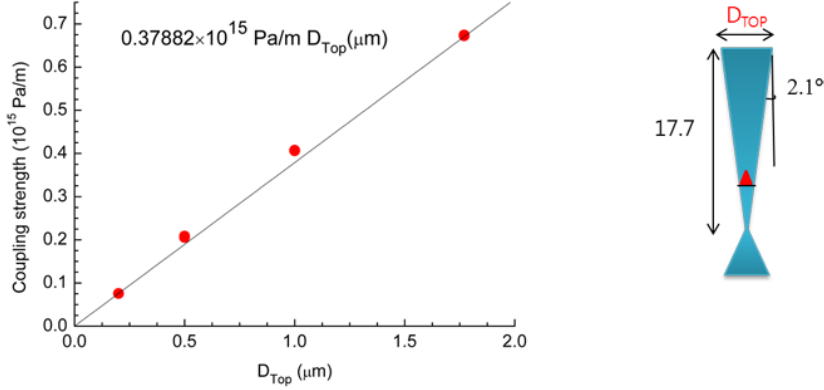


Figure 5.8: Simulated coupling strength of GaAs photonic wires - Variation of the coupling strength of the wire as a function of its top diameter. The fitting curve is given by $C_{st}(10^{15} Pa/m) = 0.37882 \times D_{Top}[\mu m]$.

In our experiments, we have GaAs photonic wires whose diameters vary from 200 nm up to few μm for systematic studies. Figure 5.8 summarizes the diameter dependence of the coupling strength with the simple analytical relation

$$C_{st}(10^{15} Pa/m) = 0.37882 \times D_{Top}(\mu m). \quad (5.37)$$

Choosing the realistic parameters of $D_{Top} \sim 1.98 \mu m$ and $L_{Top} = 17.7 \mu m$ with the etching angle 2.1° leads to the coupling strength $7.5 \times 10^{14} Pa/m$.

5.2.3 QD Response to Mechanical Strain

When the GaAs photonic wire is driven close to a fundamental eigenfrequency, the wire vibrates resonantly in a linearly polarized mechanical mode. In reaction to the wire bending to one side, QDs located on its side is under compression while the other side is dilated. Figure 5.9 describes the change of a small volume embedding a QD under hydrostatic compressive and tensile stresses. As a consequence for the bending of the wire, an uniaxial stress is applied on the QDs along the z -direction. For a nanometer displacement at the top in a linearly polarized mode, we found that a dot experiences

5.2 Strain Effect on Oscillating GaAs Photonic Wires Embedding InAs QDs

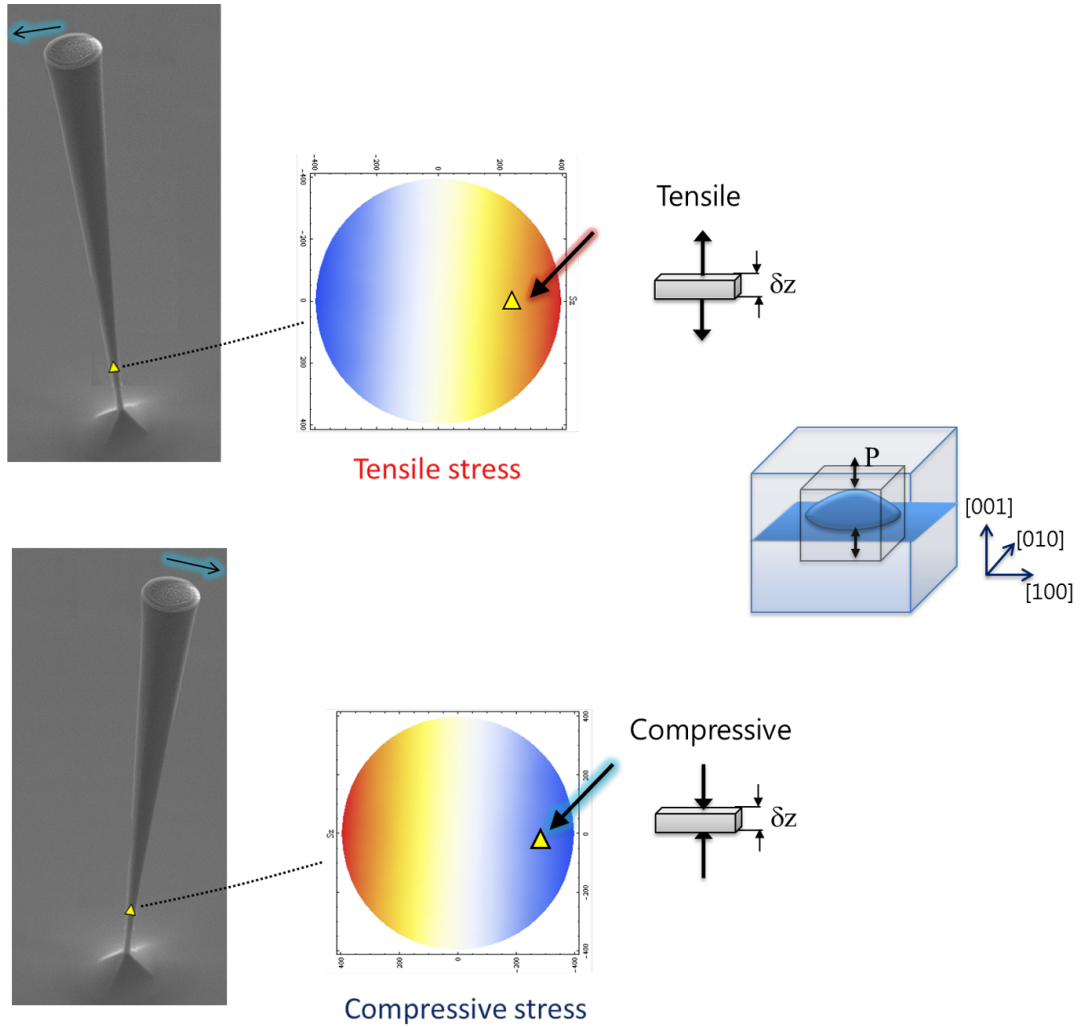


Figure 5.9: Mechanical effects on InAs quantum dots embedded in a resonantly oscillating GaAs photonic wire - GaAs photonic wire is fixed at one end and driven mechanically with a piezoelectric transducer. The QD plane is located $3 \mu\text{m}$ above the bottom of the wire, where induced strains is considerable for the first flexural mode of the wire. As the wire vibrates inducing tensions at the top, the pressure P is applied on a cubic cell including InAs QDs. Zooming in this region of an InAs QD is depicted on a color coded simulated strain map and shows how the axial stress varies as oscillating wire pulls up and pushes down the QD region. The wire oscillation induces a fractional change of δz at a cubic cell including QDs in a linearly polarized mechanical mode.

5. STRAIN-INDUCED OPTOMECHANICAL COUPLING FOR QUANTUM DOTS IN PHOTONIC WIRES

the strain ($\Delta a/a$) not more than 8.8×10^{-6} for a wire $D_{Top} \sim 1.98 \mu\text{m}$. As a single InAs QD undergoes the compressive stress in the vibrating wire, the stress pushes down the height of the QD by increasing the confinement energy and thereby induces a blue shift of the QD transition energy. When the wire bends to the other side by pulling up the height of the QD, the QD transition energy is red-shifted. The strain-induced modifications in the QD transition energy are illustrated in Fig. 5.10.

Referring Eqs.(5.16) and (5.17), QD energy shifts δE_{shift} in a bent cylindrical wire can be simply derived by:

$$\delta E_{shift} = \frac{D_{QD}}{L^2} Y \kappa \delta x_{shift} \quad (5.38)$$

where D_{QD} denotes the diameter of the photonic wire at the level of QDs, L is the height of the wire, Y is the Young's modulus and δx_{shift} is the displacement at the top. Here, $\kappa (= \kappa_{uni} + \kappa_{con} + \kappa_{mixing})$ is decomposed by dependences of the GaAs band-gap on a tensile uniaxial stress $\kappa_{uni} = -5.32 \text{ meV/kbar}$ and the confinement potential $\kappa_{con} = -2.2 \text{ meV/kbar}$. In addition, the In composition gradient in QD can give an error bar in the $0 \leq \kappa_{mixing} \leq 1.2 \text{ meV/kbar}$ of range. Using this simple approximation for cylindrical wires, Eq.5.38 shows the general trend for the QD energy shifts, which scales as L^2 .

For a cylindrical wire, the total strain-induced modulation of the QD emission energy then reads as

$$\Delta E_{uni}^{Total} = 2\delta E_{shift} = 2 \frac{D_{QD} Y}{L^2} \kappa \delta x_{shift}. \quad (5.39)$$

This strain-induced shift of the QD emission energy during the vibration period tells us how much the QD emission energy can be controlled by mechanical strains. We will compare this estimate to our experimental results.

The strain-induced shifts of QD transition energies strongly depend on QD positions inside the wire. In fact, a strain-induced spectral shift can happen only when the QD is located aside from the neutral axis of a linearly polarized mechanical mode. For the fundamental flexural modes of the wire, the deformation due to the oscillation is vanishing at the neutral axis. As one can check on the strain map shown in Fig. 5.9, there is a strain gradient from the neutral axis to the edge of the wire when the wire vibrates. Depending on dot locations within the cross section of the wire, different QDs experience different shifts.

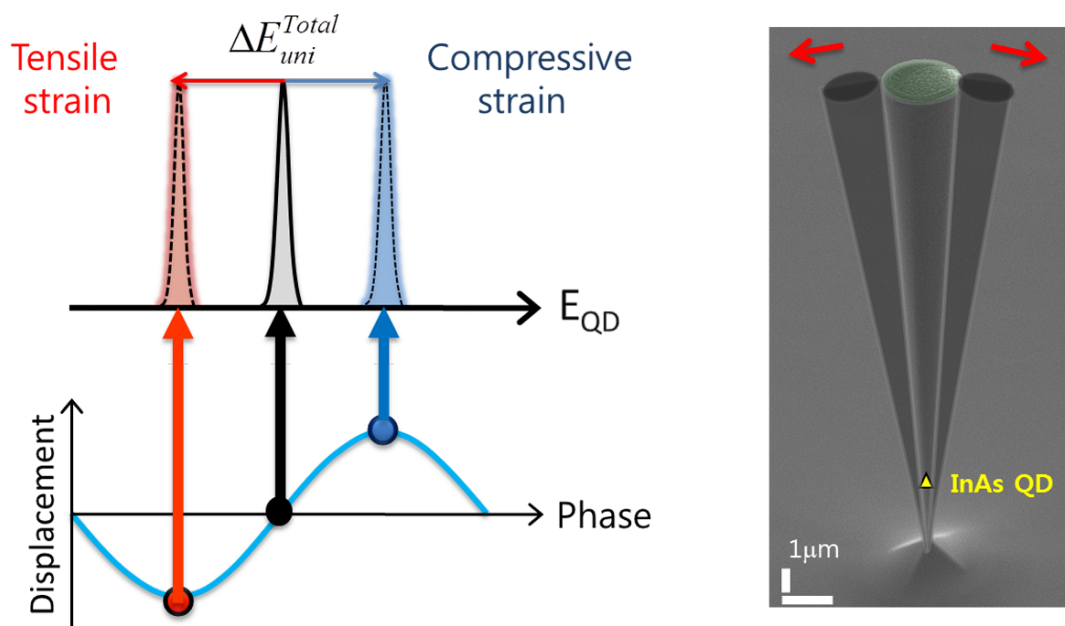


Figure 5.10: Oscillating vertical GaAs photonic wire embedding InAs QDs at its resonant frequency - Periodic displacement δx of a GaAs wire is schematically shown in the time-domain resulting in shifts of QD emission energies. The strain-induced shift $\Delta E_{uni} = 2\delta E_{shift}$ in QD emission energies can conversely probe the periodic motion of the wire.

5. STRAIN-INDUCED OPTOMECHANICAL COUPLING FOR QUANTUM DOTS IN PHOTONIC WIRES

Using a finite element software, we have computed a maximum coupling strength of $7.5 \times 10^{14} Pa/m$ at the edge of the wire of $D_{QD} \sim 720$ nm in the QD plane. In an unbent wire, our QDs are already under an in-plane intrinsic compressive strain owing to 7% percent InAs-GaAs lattice mismatch, as we mentioned before. For a 1 nm displacement at the top, QDs located close to the sidewall undergo an uniaxial stress of $0.75 MPa$.

5.3 Optomechanical Characterization of GaAs Photonic Wires

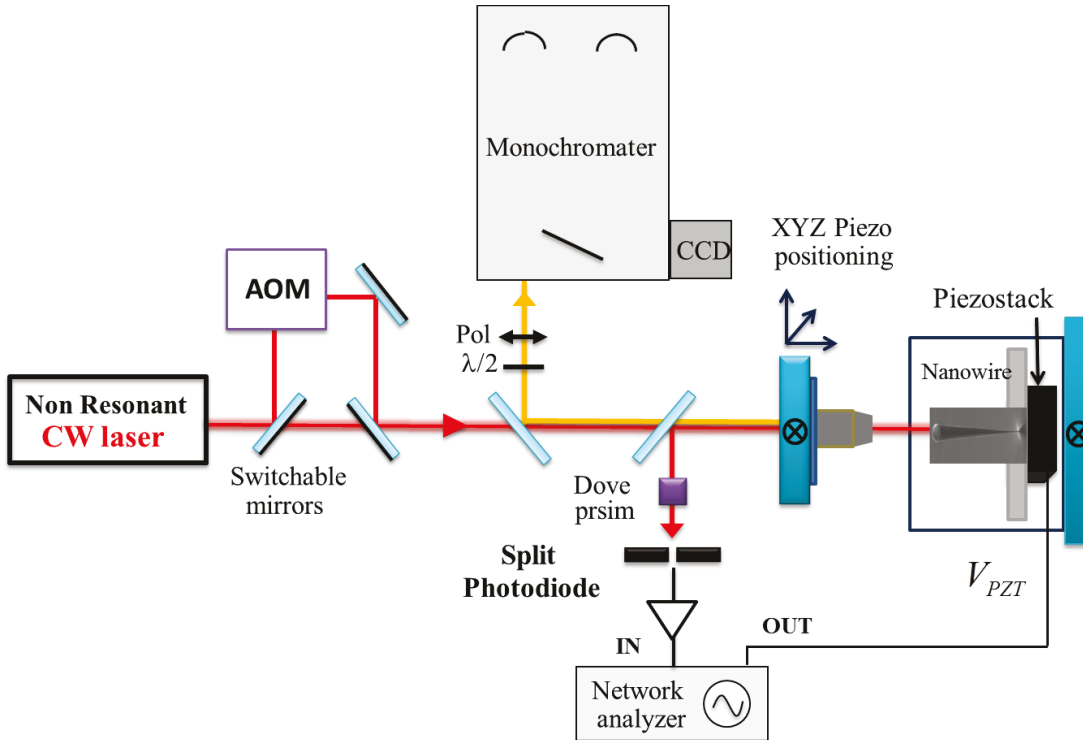


Figure 5.11: Experimental setup for the nano-optomechanical characterization of a GaAs photonic wire - Schematics of the optomechanical setup used to actuate and detect wire oscillations. A CW nonresonant laser beam (825 nm) is incident on a vertical GaAs photonic wire, which is mounted on the helium flow cryostat. The outgoing laser beam is directed either toward the split-photodiode or the spectrometer. When the reflected laser beam is sent into the split-photodiode, its output signal is displayed with the network analyzer. Using a high-bandwidth acousto-optic modulator (AOM), the stroboscopic experiment can be done. A detailed view of the stroboscopic setup will be schematically presented in Fig. 5.20.

5.3 Optomechanical Characterization of GaAs Photonic Wires

This section first gives an overview of experimental techniques used to probe and control the strain-induced optomechanical coupling of InAs dots embedded in a resonantly vibrating GaAs photonic wire. The optomechanical setup has been significantly modified with respect to the optical setup presented in Chapter 3.

5.3.1 Optomechanical Setup

A schematic of the optomechanical setup used to characterize vibrating photonic wires is shown in Fig. 5.11. The sample is located in vacuum on a cold finger helium flow cryostat at temperature of $T=5$ K. It is mechanically excited with a piezo electrical transducer glued at the back of the sample holder. It is illuminated by a continuous wave laser diode via a microscope objective having a numerical aperture $NA=0.4$. The laser diode is emitting at 1.503 eV (825 nm) and excites the wetting layer which is below the GaAs gap at 5 K so that the light can propagate with low absorption along the photonic wire. This was already discussed in Chapter 3. The illumination laser is guided through a microscope objective and is focused on its top facet, with a spot size of 2.4 μm . The wire mechanical oscillations are characterized by analyzing the light beam that is reflected from its top facet on a split-photodetector (100, 124). The split photodiode is positioned at the back focal plane. The photocurrent difference is amplified and sent to the network analyzer. A Dove prism is placed in front of the split-photodiode for the rotation of the image onto the split-photodiode. A prism rotation by an angle θ leads to an image rotation by twice the angular displacement 2θ . As the prism is rotated, the image projected onto the split-photodiode changes. Starting from the maximum signal in a linearly polarized mode, a 45° rotation of the prism results in complete extinction of the output signal while the split-photodiode is blind to a 90° rotated image. The concept of the wire detection is schematically illustrated in Fig. 5.12. More technical details of the detection part will be discussed in the following section. Still we can switch to the typical photoluminescence setup. The QD photoluminescence spectrum (around 1.35 eV) is acquired on a charge coupled device (CCD) at the output of a 1.5 m focal length spectrometer operating with a 1200 *grooves/mm* grating. The overall spectral resolution is around 12 μeV .

5. STRAIN-INDUCED OPTOMECHANICAL COUPLING FOR QUANTUM DOTS IN PHOTONIC WIRES

- **Imaging of vibrating wire**

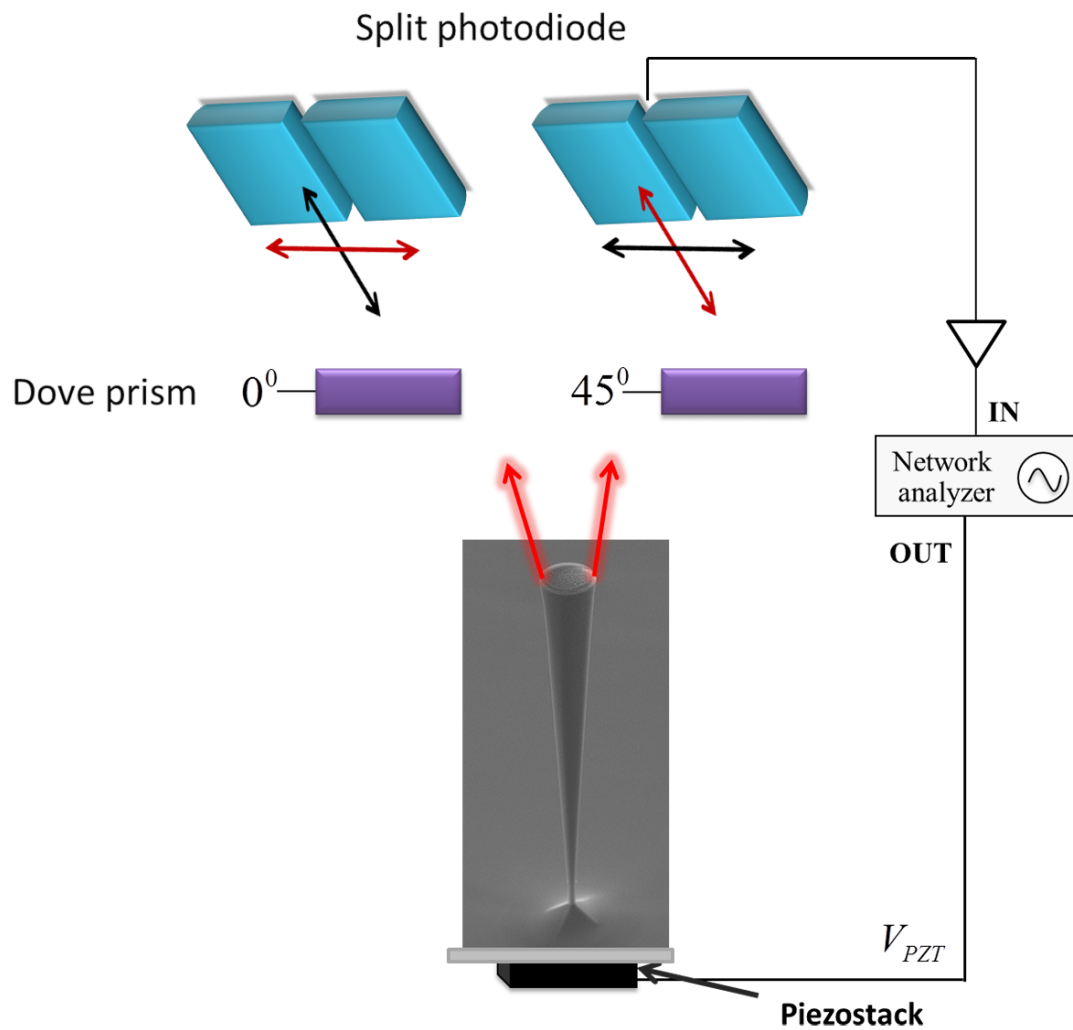


Figure 5.12: Schematics of the detection setup for imaging vibrating wires - When the piezoelectric transducer (PZT) is used to drive the wire with the voltage V_{PZT} , the vibrating wire generates a sinusoidal signal in the split-photodiode detector. The signal can be maximized by rotating the output signal image via a rotation of the Dove prism.

5.3.1.1 Optical Detection: Split-photodiode

Since our experiment needs to optically detect the in-plane vibrations of wires, signals are taken using a split-photodiode detector was developed by D. Lepoittevin and O. Arcizet (100, 125) using Hamamatsu *S4349* photodiode, providing a large bandwidth of 20 MHz. The split-photodiode is placed on the reflected laser beam path. The incident laser beam is parallel to the longitudinal axis of the vertical GaAs photonic wire. When the laser beam is focused on the top of the wire with a Gaussian beam waist of about 2.4 μm comparable to its top diameter, a part of the laser beam is reflected off by the top facet and sent to the split-photodiode. As the wire vibrates, resonant features can then be detected by monitoring the change in the relative intensity between the two halves of the split-photodiode. Thus, amplitudes of the AC output of the split-photodiode mainly features the resonant motion of a photonic wire.

5.3.1.2 Micro-positioning of Photonic Wire in Optical Waist

In order to properly measure the dynamics of a vibrating wire, a key requirement is to position the optical beam waist on the micron-scale top facet of the wire. To do that, a labview program developed by A. Gloppe and O. Arcizet (125) is used to scan and control the laser beam position of all three axes with respect to static photonic wires. Positioning and scanning ranges are of up to 30 μm along x and y in the horizontal plane, and 10 μm along z with 20 nm positioning accuracy. The 12 bit DAC card is then used to ask the piezostage to move, and the DC voltage spent on the split-photodiode is synchronously acquired. The DAC card has a maximum spatial resolution of about 7.3 nm along x and y and 2.4 nm along z .

Our strategy is then to measure a two-dimensional map of the wire in terms of DC voltage using the automatic program of the laser beam positioning. In our experiment, two types of two-dimensional maps were used to optimize the optical waist on the top facet of a wire. The two types of maps are XY and XZ cartographies in reflection;

- XY map: Two dimensional positioning of the laser beam for a particular focus
- XZ map: Optimizing the focus

When we measure two cartographies, the first requirement is to choose a beam waist comparable to the top diameter of a vibrating wire. In comparison with wire's top

5. STRAIN-INDUCED OPTOMECHANICAL COUPLING FOR QUANTUM DOTS IN PHOTONIC WIRES

diameter, a significantly smaller laser spot makes the device blind to wire's vibrations while a too large laser spot vagues the dynamic features by reducing the intensity of the backscattered light from the wire. In this work, the laser has a spot size of $2.4 \mu\text{m}$, comparable to wire's top diameter of $1.98 \mu\text{m}$.

Let's first discuss about the XY map. Figure 5.13 shows the measured XY cartography in reflection of a wire ($D_{Top}=1.98 \mu\text{m}$). The purpose of the XY map is to position the laser beam at the center of a static wire. In Fig. 5.13, one can easily check if the beam position is precisely centered on the top facet of the wire. For example, Fig. 5.13 reveals maximum voltage signal once the beam is centered on the wire's top facet. As the laser beam is precisely scanned across the radial axis, the strongest voltage gradient is observed.

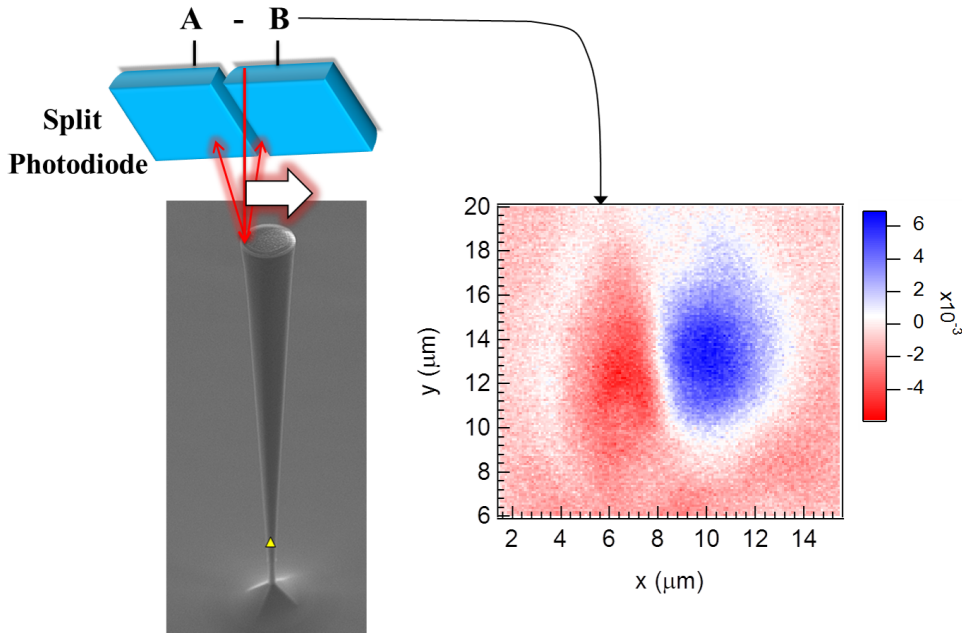


Figure 5.13: Static 2D map - Contour color coded map of the laser reflection by the wire ($D_{Top}=1.98 \mu\text{m}$) as a function of the lateral positions x and y .

Once the laser scanning is well-adjusted across the radial axis of the wire in this way (strongest voltage gradient), the focus should be optimized with the XZ map. Figure 5.14 shows a typical two-dimensional XZ map. As displayed in Fig. 5.14, the voltage gradient across the radial axis of the wire are measured for several focuses. It seems that the laser beam waist is optimized at the junction of blue and red lines.

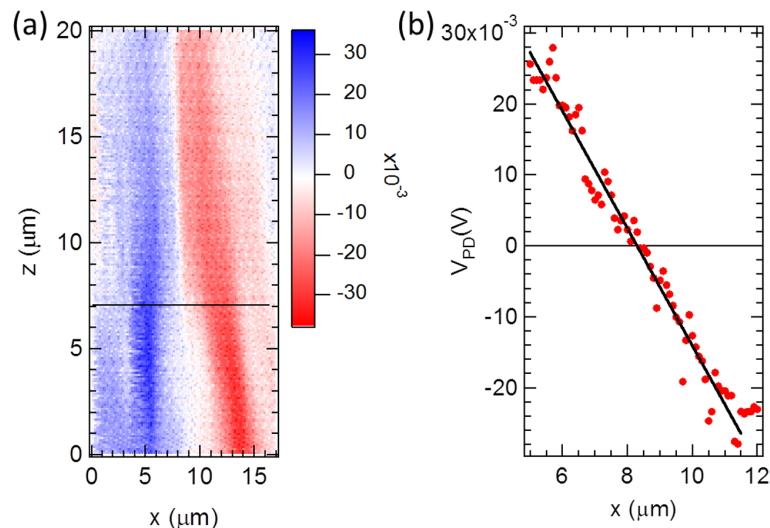


Figure 5.14: Static 2D map - (a) XZ map of the reflection is obtained as a function of the horizontal scan across the wire relative to several laser focuses. (b) At the junction of blue and red lines, the voltage signal $V_{PD}(x, z = 7)$ is sliced and plotted as a function of the laser beam position x .

In summary, XY scan first allows to position the laser beam at the center of wire's top facet in sub-micron scales. With XZ scan, the beam waist is localized on its top facet. In this way, we can maximize the detection signal in the split-photodiode. The voltage reference is also provided by the XZ map for the wire displacement calibration.

5.3.1.3 Displacement Calibration

In the optimum detection scheme configured with two maps, we can effectively characterize the dynamic motion of wires with the AC output of the split-photodiode. To study qualitatively the vibration of wires and its influence on embedded QDs, the AC voltage signal has to be converted to a real wire's displacement in a nanometer scale. As a way to get the voltage-displacement reference, we can measure the difference in the voltage signal by displacing the laser beam by a calibrated distance in nanometer scales onto the static wire. Since the two-dimensional XY and XZ cartographies include all these informations as shown in Figs. 5.13 and 5.14, we can just slice the typical XZ map at the y junction and fit the voltage slope. A linear fit gives the reference voltage

5. STRAIN-INDUCED OPTOMECHANICAL COUPLING FOR QUANTUM DOTS IN PHOTONIC WIRES

slope of

$$\frac{V_{PD}}{x} = -8.2 \times 10^3 \frac{[V]}{[m]} \quad (5.40)$$

for the wire of $D_{Top} = 1.98 \mu\text{m}$. Since the reference DC voltage/displacement slope is quantified, now we can convert the AC output signal in a real displacement in nanometer scales.

In the following, we can write down the top displacement δx of an oscillating photonic nanowire from the equilibrium position as

$$\delta x[m] = C \times 10^{(P_{dBm}-10)/20} S_{21} \times \frac{1}{8.2 \times 10^3}, \quad (5.41)$$

where C denotes the ratio of AC and DC gains and S_{21} denotes the peak value of the AC signal measured in the network analyzer. Here, the power P_{dBm} used to drive the piezoelectric transducer is configured in units of dBm in the network analyzer. With the conversion factor $10^{(P_{dBm}-10)/20}$, the P_{dBm} is converted in voltage scales. The ratio C is found to be 3.75 in our experimental circuits.

5.3.1.4 Ratio of AC and DC Gains

Since the DC voltage signal is used as a reference for the displacement calibration, we need to clarify the ratio C between DC and AC gains. In our experimental configuration, AC and DC circuits are independently amplified and filtered, thereby their electronic gains could be different. In order to check the ratio between AC and DC circuits, the modulated laser beam is illuminated on one of the quadrants. The laser beam is chopped with a period of 500 kHz with a duty cycle of 50%. In this way, the laser illumination goes from approximately zero to a maximal value, and the average intensity corresponds to half the maximum value. Voltages generated on the DC and AC outputs of the photodiode circuit read as

$$\begin{aligned} V_{DC} &= G_{DC} \times v^P \\ V_{AC} &= G_{AC} \times v^P \times sq(\omega) \end{aligned} \quad (5.42)$$

where $sq(\omega)$ is a square wave that goes from -1 to $+1$, and v^P denotes the peak value of the ‘‘preamplified’’ AC signal. The ratio between the DC gain G_{DC} and the AC gain G_{AC} was found to be 2 (125) in measurements with two ports of the oscilloscope.

5.3 Optomechanical Characterization of GaAs Photonic Wires

In our data acquisitions during the experiment, DC and AC signals are however measured with different impedance devices. The DC output voltage signal is taken by PC through a NI PCI 6023e board configured as high impedance input and output. On the other hand, the AC signal is measured with a different high-impedance device, an Agilent *E5061B* network analyzer with port impedances of 50Ω . The network analyzer displays the S_{21} scattering parameter which corresponds to V_{Port2}/V_{Port1} .

To check the effective ratio of $G_{DC}^{eff}/G_{AC}^{eff}$ in our experimental circuit, the DC voltage signal should accordingly be measured with a 50Ω load in one port. In this way, we can compare the DC output signal with that of AC taken in another port using the oscilloscope. From this comparison, the conversion factor of $G_{DC}^{eff}/G_{AC}^{eff}(=^{HZ}V_{DC}/^{50\Omega}V_{AC})$ is found to be 3.75. Here, V_{DC}^{HZ} denotes the voltage measured respectively with a high impedance device and $V_{AC}^{50\Omega}$ is the voltage measured on a device with a 50Ω impedance.

5.3.2 Measured Mechanical Response: Q Factor

We characterize the resonant behaviors of GaAs photonic wires via mechanical response spectra at 4.5 K in a residual atmosphere of 10^{-5} Pa. Figure 5.15 displays the resonant features of wires of $D_{Top} = 1.98$ nm for voltages driving the piezoelectric transducer in the mV range. The wire's motion is driven by the piezoelectric transducer while the frequency is swept forward around the resonance frequency of its fundamental flexural modes. The fundamental response is then read by the network analyzer. The fundamental resonance frequencies are clearly seen at around 435 and 503 kHz with the same quality factor of 870 at $V_{PZT}^{PP} = 50$ mV. Note that the mechanical quality factor Q is given by $Q = f_{res}/\Delta f$ where f_{res} and Δf are the resonance frequency and the full width at half maximum of the resonant peak, respectively. The Δf is obtained by fitting with a Lorentzian function.

The measured first flexural modes are in good qualitative agreement with numerical calculations in the context of the non-isotropic etching. Note that the fundamental flexural eigenmode has a twofold mechanical polarization degeneracy for perfectly circular wires. As discussed in previous sections 5.2.1 and 5.2.2, the mechanical resonant frequencies strongly depend on the dimensions and geometry of the conical wire, and on the possible presence of the asymmetry in its diameter after the non-isotropic etching. As seen in previous section 5.2.1, using the finite element software, numerical calculations estimated eigenfrequencies of 429 and 517 kHz respectively for etching angles of

5. STRAIN-INDUCED OPTOMECHANICAL COUPLING FOR QUANTUM DOTS IN PHOTONIC WIRES

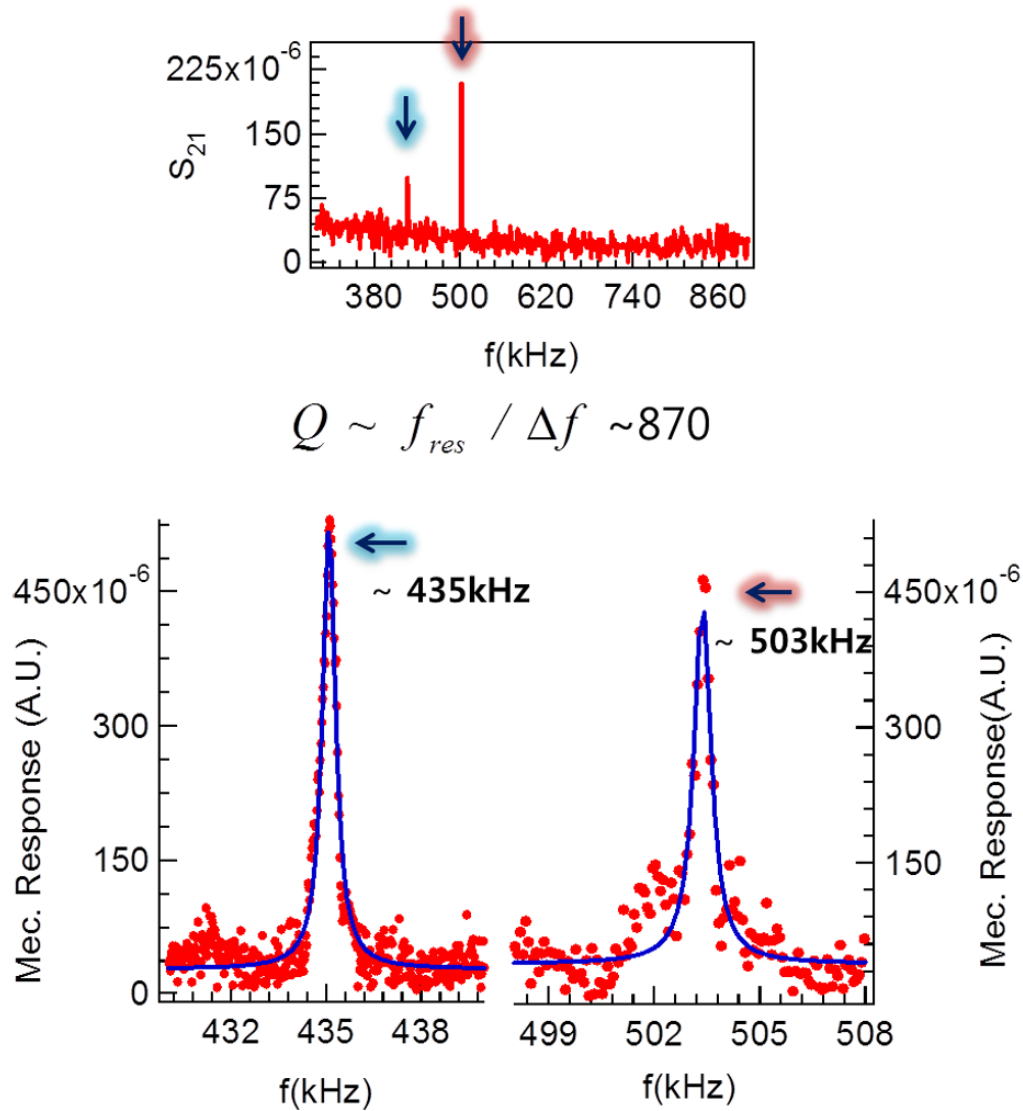


Figure 5.15: Mechanical resonance characteristics of a GaAs photonic wire of diameter $D_{Top} = 1.98 \mu\text{m}$ - Mechanical frequency response of GaAs nano-optomechanical photonic wire is optically measured from 300 kHz up to 1 MHz at 4K with the driving voltage of 50 mV. Two arrows indicate the fundamental flexural modes of the photonic wire.

5.3 Optomechanical Characterization of GaAs Photonic Wires

2.5° and 2.4°. In fact, it is not so surprising that the etching angle is not perfectly isotropic since the GaAs crystal itself is not isotropic (126). Due to the non-uniform distribution of atoms at their interior, a non-isotropic etching occurs at different rates for different crystalline directions. The etching direction can easily be changed by the wire position, for example, in a certain array. From one wire to another, we observe sometimes almost degenerate eigenmodes, and sometimes almost ~ 100 kHz splitting between the two fundamental eigenmode. In a random manner, the splitting was found to vary from zero up to ~ 100 kHz for several wires. Therefore, the non-degenerate fundamental modes of the GaAs photonic wire come from the non-isotropic etching.

Experiment with a rotating Dove prism was then conducted to investigate the mechanical polarization of the two fundamental flexural modes. As mentioned in section 5.3.1, by rotating the dove prism by θ around its own long axis, the output image of mechanical modes is rotated by twice the angle (2θ). The explicit angle dependence of mechanical response amplitudes is given in Fig. 5.16 with a conceptual diagram of the polarization experiment. The fundamental modes exhibit two orthogonal directions for their mechanical polarizations. At a 90° relative rotation of image outputs, one signal vanishes completely while the other is maximized. Here, we have difficulty to recover the same maximum intensity in X and Y mechanical polarizations by rotating Dove prism angle. This is due to an unexpected noise which sometimes appeared in the high frequency side near Y polarization.

At the two mechanical resonances, the oscillation amplitude of the wire at the top is calibrated in a nanometer scale using the DC voltage reference, as discussed in section 5.3.1.3. For a driving voltage $V_{PZT}^{PP} = 50$ mV, the peak to peak amplitudes of A_X^{PP} and A_Y^{PP} respectively correspond to $2A_X^P = 12$ nm and $2A_Y^P = 10$ nm. In other words, the maximum top displacements of the wire are ± 6 nm along X polarization mode and ± 5 nm along Y polarization mode, respectively.

5.3.3 Strain Effects on QD Emission Energy

In the previous section, we have identified mechanical resonance behaviors of GaAs photonic wires. At one step further, we now investigate the effect of the wire oscillation on the photoluminescence spectrum of several QDs embedded in the wire. The typical photoluminescence spectra of single InAs dots is shown by the black line in Fig. 5.17(b). There are eighteen QD lines in this photoluminescence spectrum. As

5. STRAIN-INDUCED OPTOMECHANICAL COUPLING FOR QUANTUM DOTS IN PHOTONIC WIRES

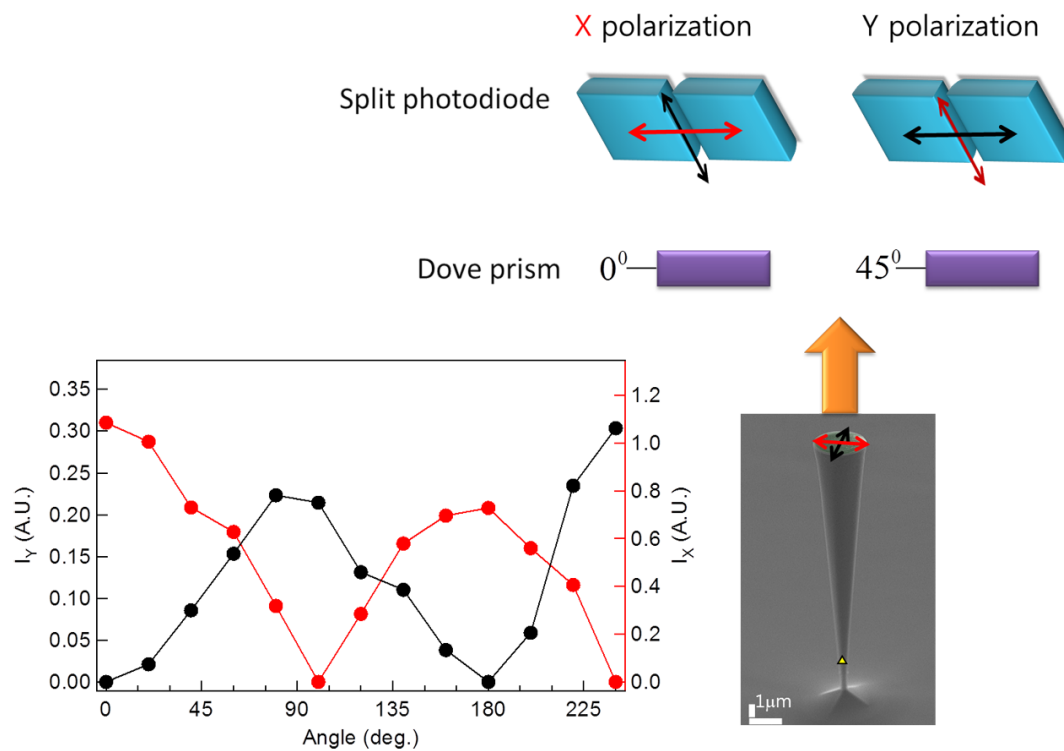


Figure 5.16: Two orthogonally polarized mechanical modes of a GaAs photonic wire - As the Dove prism is rotated by 45° , the output images from orthogonally polarized modes are rotated by 90° and projected onto the split-photodiode. By rotating the angle of the Dove prism, the mechanical response is measured for the two fundamental modes of the wire and their maximum intensities are respectively plotted with black and orange dots as a function of the rotation angle.

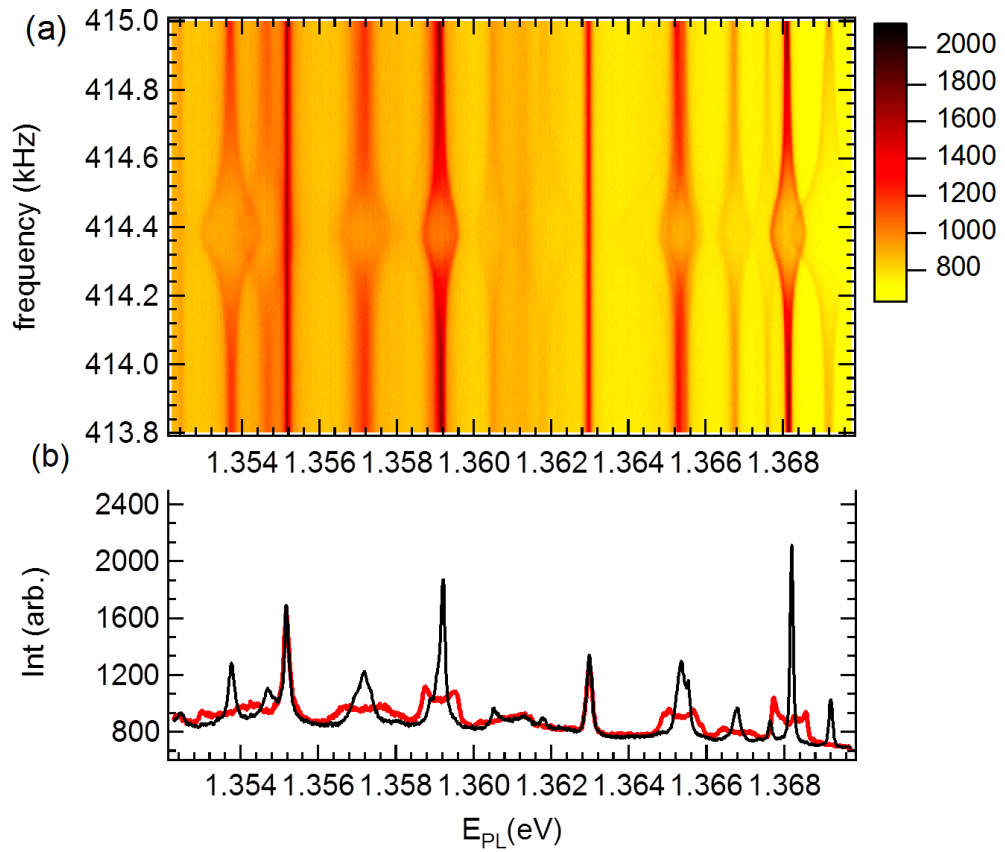


Figure 5.17: Mechanical resonance characteristics on QD photoluminescence spectra - (a) Strain-induced spectral shifts of several QDs embedded in a photonic wire are measured as a function of the mechanical frequency. Closer to the mechanical resonance, the initially narrow linewidths of QDs broaden due to the sinusoidal oscillation of the wire. (b) On- and off-resonance photoluminescence spectra are plotted respectively with red and black lines.

5. STRAIN-INDUCED OPTOMECHANICAL COUPLING FOR QUANTUM DOTS IN PHOTONIC WIRES

already investigated in Chapter 3, a single QD exhibits two or three lines corresponding to the exciton, biexciton or charged exciton states. In fact, there are only twelve QDs. The QD families will be identified later on by their power dependence and the QD spatial mapping. The mechanical frequency is then swept downward across the resonance while we check the influence of strain on photoluminescence spectra. Figure 5.17(a) presents a view of collective photoluminescence spectra as a function of the mechanical driving frequency. The photoluminescence spectrum is measured by applying an AC voltage of $V_{AC}^{PP}=200$ mV to the piezoactuator. As seen in Fig. 5.17, the photoluminescence lines are significantly modulated as the mechanical frequency is closer to resonance. On resonance, photoluminescence lines exhibit a characteristic “camel back” shape that corresponds to the integrated spectrum of a line undergoing a sinusoidal oscillation around its equilibrium energy. For several QD emission lines, one can clearly see the different amounts of broadening, which is expected for QDs of different locations. This phenomenon is the signature of the strain-induced tuning of QD transitions at mechanical resonances.

As expected, all lines are maximally broadened at the same frequency. When the photoluminescence is maximally broadened, we cut the slice and plot with the off-resonance photoluminescence in Fig. 5.17(b). The camel back shapes are seen in most of time-averaged photoluminescence lines (red curve). Different excitonic lines experience different shifts since the strain-induced spectral shift is proportional to the distance from the neutral axis where the deformation due to the oscillation is vanishing.

We have fitted these lines to extract the strain-induced spectral shift. Experimentally, we find the maximum peak to peak spectral amplitudes to be $193 \mu\text{eV}$ and $169 \mu\text{eV}$ respectively for two orthogonal motion amplitudes of $A_X^P = 6$ nm and $A_Y^P = 5$ nm at $V_{PZT}^{PP}=50$ mV. Using a finite element software, we have computed maximum stresses of 5 MPa and 4 MPa respectively at the wire edge, for X and Y mechanical polarizations in the QD plane.

5.3.4 Mechanical Resonance Effects on Collected Photoluminescence

Figures 5.18 present the normalized integrated intensity of a single QD (marked with black arrow) vs the down-sweep frequency with the waterfall plot of the photoluminescence spectra at 200 mV. Clearly, a dip is shown in the integrated photoluminescence intensity by around 2%. This is one of hallmarks of the mechanical vibration of the wire.

5.3 Optomechanical Characterization of GaAs Photonic Wires

As the driving voltage increases, the dip becomes deeper in the normalized integrated intensity (see, Fig.5.19).

This can be understood by noting the detection scheme of QD signals. Looking back at the discussion of Chapter 2, the QD signal was recollected within a fixed optical detection volume defined by wire geometries and the numerical aperture of the objective lens. If the maximum displacement of a vibrating wire is farther away from the fixed optical volume at high driving powers, the number of photon collected within this volume will be reduced. In this context, the dips in the normalized intensity of QD emissions truly confirms the top displacement of a vibrating wire in a fundamental flexural mode. Although the contrast of the observed dip is not better than 3%, it still reflects the influence of the wire's dynamics on the light collection part.

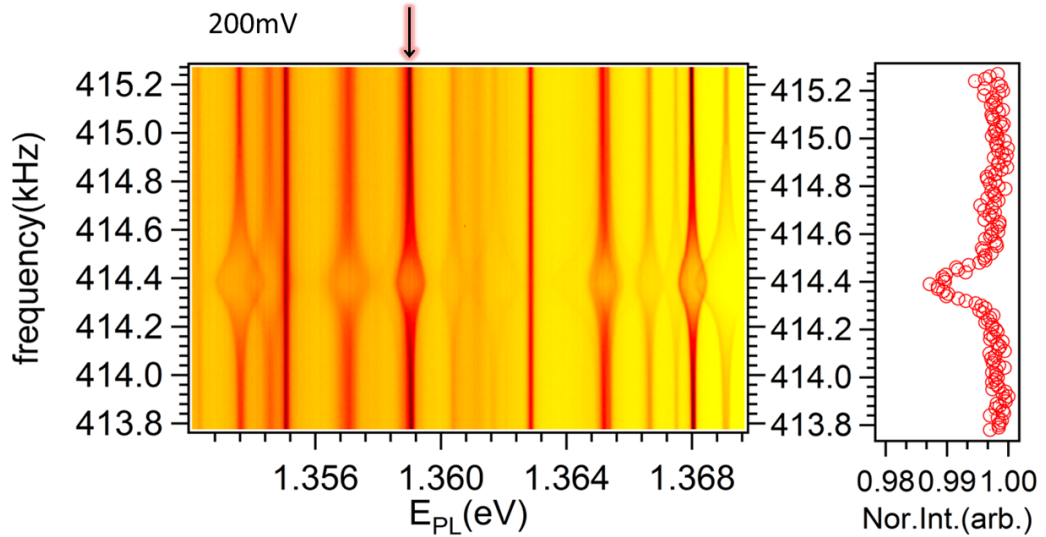


Figure 5.18: Signatures of wire dynamics - The strain-induced spectral broadening is shown with the two-dimensional collective photoluminescence spectra. Corresponding to the A^{PP} , the normalized integrated intensity is plotted in the right side by analyzing a single QD line marked by the arrow. As the wire is brought into the resonance, the reduction of the QD emission rate reflects the spatial variation of the wire across the optical spot.

5.3.5 Stroboscopic Illumination

In the previous section, QD emission energies are tuned over a range of few hundred μeV due to the sinusoidal oscillation of the wire. Having done all this, one can naturally

5. STRAIN-INDUCED OPTOMECHANICAL COUPLING FOR QUANTUM DOTS IN PHOTONIC WIRES

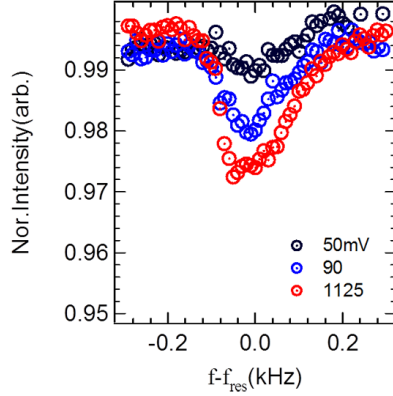


Figure 5.19: The normalized integrated intensity of the single QD embedded in a photonic wire by increasing the driving the piezo voltage - During a downward frequency sweep, the integrated intensity of the single QD is monitored from the photoluminescence spectra measured at low laser power 830 nW with the integration time 10s. The normalized integrated intensity from photoluminescence time series shows a 3% dip at the fundamental resonance frequency. QD photoluminescence signal is reduced due to the spatial deviation from the optical detection volume.

ask the possibility of choosing a specific value of the QD tuning in a vibrating wire. A possible technique to define a particular QD emission wavelength is the stroboscopic illumination on this wire for an acquisition time which is short compared to its oscillation period. Stroboscopic illumination is a well-known technique to measure temporal sequences of moving objects during the flash of the stroboscopic light to the object. The way the technique works is to synchronize a strobe light flash with a moving object. Quantitative estimates of motions can be obtained from taken snapshots, which can be played back at any desired speed.

In our experiment, the light source flashes are supplied by the first-order diffracted laser beam taken out of an AOM (AOM-1250C – 848, Isomet). The laser light is chopped once per the vibration period of a GaAs photonic wire. The RIGOL DG1022 dual-channel function generator provides the synchronization of light flashes with wire excitation signals. As sketched in Fig. 5.20, both outputs of a dual output low frequency generator have the same frequency and are mutually coherent. One of the output provides a stimulus sine-waveform used to drive the piezoelectric transducer. The second output modulates an illumination waveform with the AOM driven by a $d\%$ duty cycle rectangular wave. Note that the stroboscopic illumination duty cycle $d\%$

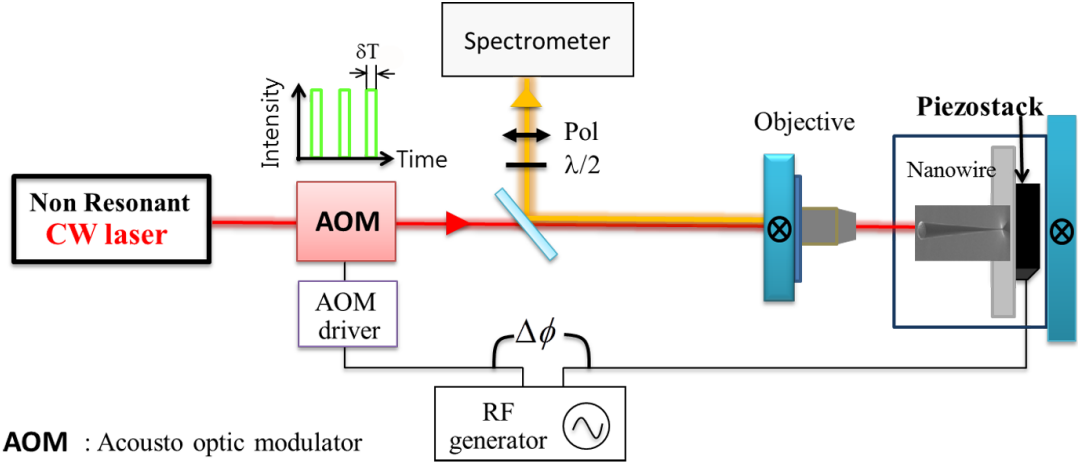


Figure 5.20: Stroboscopic setup - A detailed overview of our measurement setup is schematically shown for the stroboscopic experiment. A dual output low frequency generator is used for capturing the dynamic motion of a photonic nanowire. The dual-channel function generator synchronizes two outputs and changes their phase differences by $\Delta\phi$. Acousto-optic modulator is labeled AOM.

is given by the ratio $\delta T/T(= \delta T \times f_{res}) \times 100\%$ between the exposure time δT and the period T of the reference excitation. By changing the phase $\Delta\phi$ between the two signals (see Fig. 5.20), the vibrating wire is frozen at a selected phase which fixes QD emission lines at a well-defined energy.

Figure 5.21 illustrates the temporal diagram of stroboscopic light flashes for several phases. Just to give an example, phase selective motions of a GaAs photonic wire are drawn in Fig. 5.21 in an exaggerated way. As the relative phase varies, flashing synchronous light source freezes different states of the vibrating wire. At a given phase of the vibrating wire, QD photoluminescence is also isolated at a specific QD emission energy. In this sense, we can choose the value of QD tuning in photoluminescence time-integrated spectra.

Figure 5.22 shows the experimental data, obtained using the stroboscopic technique. Here, the excitation laser beam was chopped with an AOM driven by the generator exciting the wire motion at the stroboscopic illumination duty cycle of 10%. By optically exciting the QD in a stroboscopic manner, snapshots of the QD spectrum were obtained for several chosen phases. As shown, the resultant phase map fully recovers a sinusoidal oscillation of QD emission energies with relative phase-shifts from 0 to

5. STRAIN-INDUCED OPTOMECHANICAL COUPLING FOR QUANTUM DOTS IN PHOTONIC WIRES

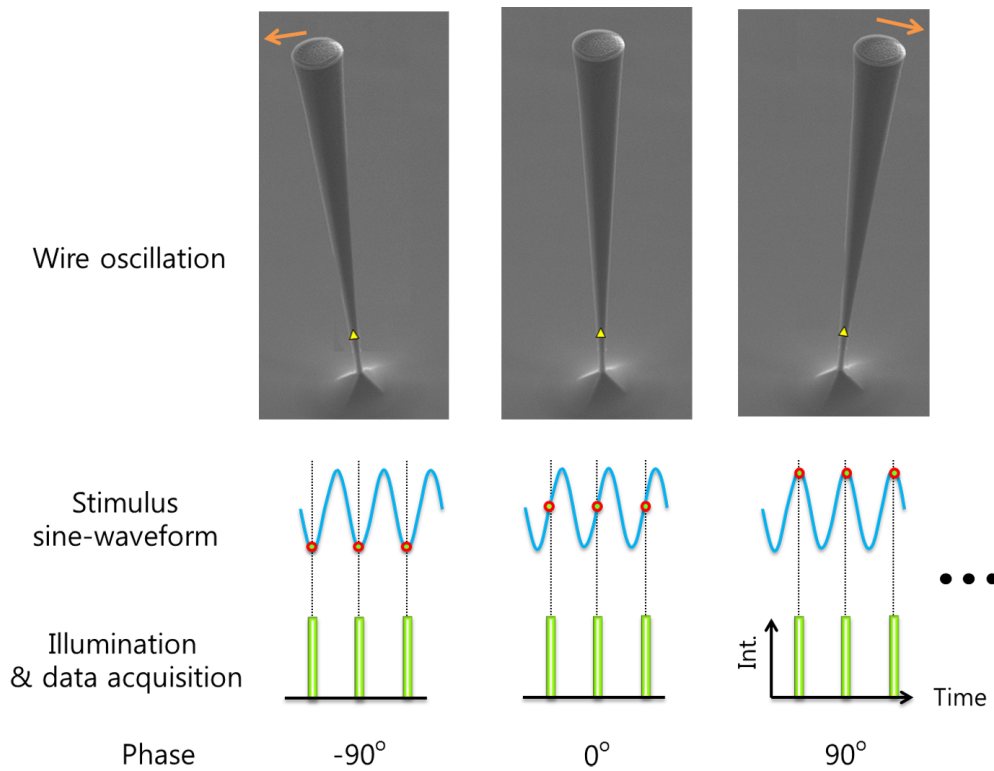


Figure 5.21: Stroboscopic illumination - SEM images of a GaAs photonic wire embedding a single InAs QD are shown with schematic diagrams of stroboscopic illuminations. Here, a yellow triangle represents an InAs QD. The illumination source is synchronized with the stimulus waveform used to excite the wire and varied for several phases. At specific phases of -90° , 0° and 90° , the motion of a wire is isolated at a chosen phase as presented on the top.

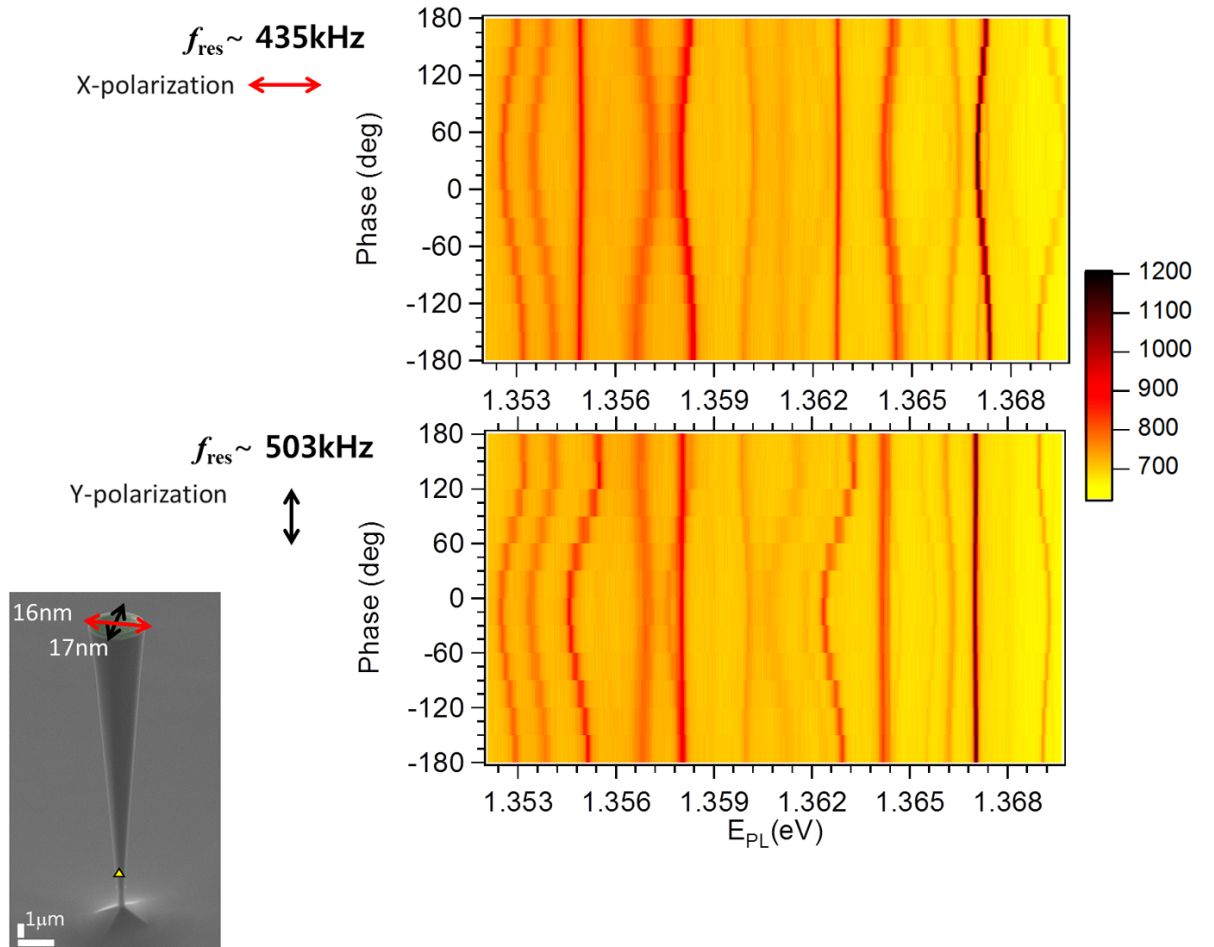


Figure 5.22: Stroboscopic photoluminescence measurement - Sinusoidal oscillations of photoluminescence lines are fully reconstructed by changing the relative phase from π to $-\pi$ at orthogonally polarized fundamental flexural modes. The AC voltage of $V_{AC}^{PP}=90 \text{ mV}$ is applied to the piezo actuator.

5. STRAIN-INDUCED OPTOMECHANICAL COUPLING FOR QUANTUM DOTS IN PHOTONIC WIRES

2π in steps of $\pi/6$. Photoluminescence spectra of selected phases each correspond to a specific position of the oscillating wire. A careful relative phase adjustment allows us to stroboscopically tune the photoluminescence emission energy of a QD over a 0.2 meV range at $V_{PZT}^{PP}=50$ mV. By fitting the central photoluminescence peak position with a sine function, the time-resolved QD shift and its amplitude give signatures of a local strain gauge of an oscillating photonic wire.

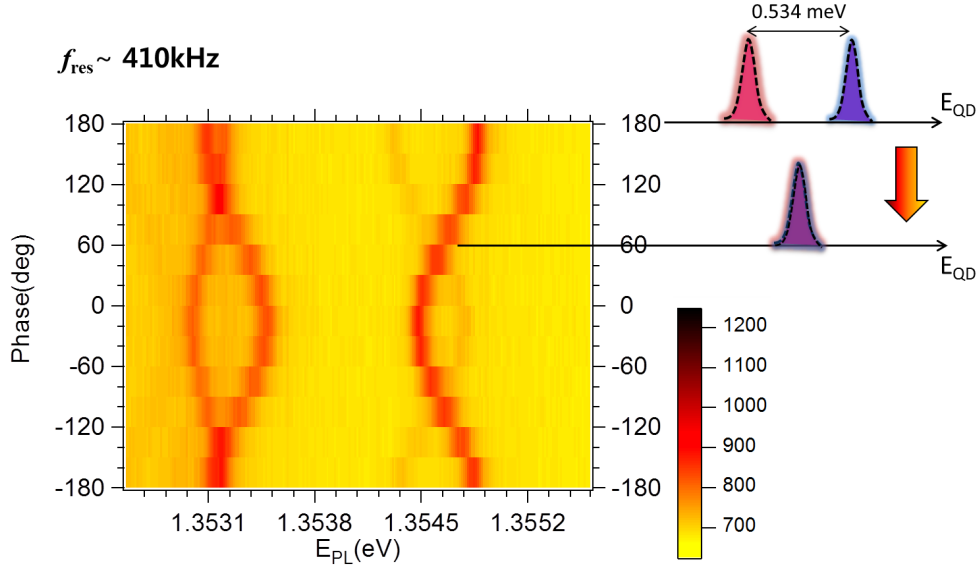


Figure 5.23: Stroboscopic tuning of two individual QDs - Two initially nonresonant QDs embedded in the same wire are brought into resonance with a careful phase tuning at around 60° and -90° . Another pair of QDs emitting at around 1.3532 eV also shows the resonance at relative phases around 90° and -150° . The GaAs photonic wire is driven at a fundamental flexural mode of 410 kHz with $V_{AC}^{PP}=90$ mV.

In addition, as seen in Fig. 5.23, we were able to dynamically bring into resonance two QDs, which are located in the same photonic wire but experience different strains. At chosen relative phases of 60° and -90° , two initially nonresonant QD lines are brought into resonance. The optical coupling provided by the one-dimensional photonic nanowire geometry opens a way to the observation of collective emission effects such as sub- or super-radiance (95).

5.3.6 QD Spatial Mapping

In the following section, we use the stroboscopic data to extract the spatial position of QDs embedded near the bottom of the trumpet-like photonic wire. As studied in the previous section, we succeeded to resolve the sinusoidal oscillations in QD emission lines stroboscopically. Since the oscillation amplitudes are directly linked to the position-dependent strain, we now go beyond tuning QD emission energies with the stroboscopic technique and draw the two-dimensional spatial map of embedded QDs in a wire. In this context, the center peak position of each QD line is fitted with a sine function in stroboscopic data. Resulting spectral amplitudes tells us how far are QDs from the neutral axis in a linearly polarized mode. This is performed in X - and Y - orthogonally polarized mechanical modes.

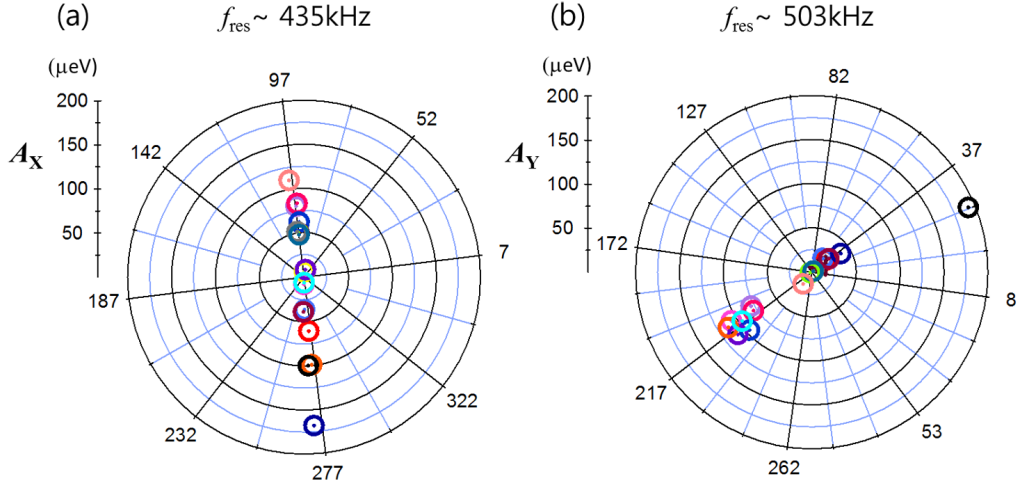


Figure 5.24: Phase-amplitude polar plots of embedded QDs in a vibrating GaAs photonic wire of diameter 720 nm - Phase-amplitude polar plots are displayed for two orthogonal linear polarizations of mechanical vibrations at around (a) 435 and (b) 503 kHz with the driving voltage $V_{PZT}^{PP} = 50 \text{ mV}$. Here, the spectral amplitude of $A_{X(Y)}$ is extracted by fitting the sinusoidal oscillation of each QD line with a sine function from the stroboscopic data performed along $X(Y)$ mechanical polarization.

The fitting results are summarized in phase-amplitude polar plots of X - and Y -polarized mechanical vibrations of the photonic wire, as seen in Fig. 5.24. The angle in this polar plot indicates the initial phase of a given QD modulation, and the radius denotes the spectral amplitude. First, one can notice that all QDs have relative phase

5. STRAIN-INDUCED OPTOMECHANICAL COUPLING FOR QUANTUM DOTS IN PHOTONIC WIRES

relation of 0 or π as shown in Fig. 5.24. It means that QDs are located either right or left hand side from the neutral axis at each fundamental flexural modes, confirming the linear polarization of each mechanical mode. In each polar plot, the amplitude informs us the relative distance from the neutral axis in each linearly polarized mode. Then, one polar graph gives us the x coordinates of the QDs in μeV energy scales, while the other gives the y coordinates. For two subsequent polar maps, full coordinates (x,y) are, therefore, given for individual QDs embedded in a wire.

Since we quantitatively know whether a shift of a given phase corresponds to the wire being bent towards one side or the other, we can distinguish between four equivalent positions (symmetric of one another with respect to the two orthogonal neutral vibration planes) for a given QD. Once the absolute position of a QD is chosen among these four possible ones, the positions of all other QDs are unambiguously defined, since the relative phases of their spectral oscillations are perfectly known.

To experimentally determine the position in an absolute manner, the network analyzer can give us access to the relative phase between the mechanical excitation and the wire position via the split photodiode AC signal. Therefore, for resonant mechanical excitation, there is an unambiguous correspondence between the spectral shift and the position of the wire.

Followed by the previous theoretical discussions in section 5.1.2, the calculated maximum shifts of about $320 \mu\text{eV}$ are estimated for InAs QD located respectively on the edge of X eigen-axis under an applied compressive stress of 5 MPa, while for a dot on the edge of Y eigen-axis, $260 \mu\text{eV}$ is estimated under 4 MPa. We can then compare the observed spectral shift for a QD line having largest amplitude in each polar plot. The calculated shifts overestimate observed maximum shifts of $169 \mu\text{eV}$ along X for the QD line 5 and $193 \mu\text{eV}$ along Y for the QD line 1. While the dots showing largest amplitude are not necessarily located at the edge of each eigen-axis of wire, we still don't know whether the mismatch comes from the position uncertainty of the dots or calculation errors. Since the quantitative computation is not accurate enough for determining the magnitude of the spectral shift, we then convert the radial coordinate in a nanometer scale by assuming a uniform distribution of QDs inside the wire. As mentioned in Chapter 2, self-assembled InAs QDs are randomly distributed inside the wire. In fact, there is a defective region near the surface of a wire where QDs do not luminescence. We will first of all estimate the width of the dead layer at the QD level.

5.3 Optomechanical Characterization of GaAs Photonic Wires

To first estimate the width of the dead layer, we performed a statistical measurement of the number of QD photoluminescence lines as a function of the wire diameter, as plotted in Fig. 5.25. The spectral window of about 17 meV centered at 1.36 eV is used for the statistical measurement. Recalling the non-isotropic etching angle, the cross sectional area A_{QD} in the QD plane is calibrated respectively for trumpet angles 2.1° and 2.2° . The data was then fitted using both a simple linear model and a piecewise non-linear model that is more closely related to the physical structure of the trumpet-like wire, assuming that there is a dead zone near the surface where QDs will not contribute to emit in the guided mode. Using a piecewise non-linear fit, we obtained the thicknesses of the dead layer of 73 nm for 2.1° , and 45 nm for 2.2° . This dead zone is assumed to be homogeneous and has the cylindrical symmetry. The statistical analysis also reveals the spatial homogeneity of the areal density of the QD ensemble as the size-dependent statistics on QD photoluminescence lines follows a linear curve. Therefore, the scaling of the map shown in Fig. 5.26 is done by choosing a circle, the area of which matches the QD surface density exhibited from Fig. 5.25.

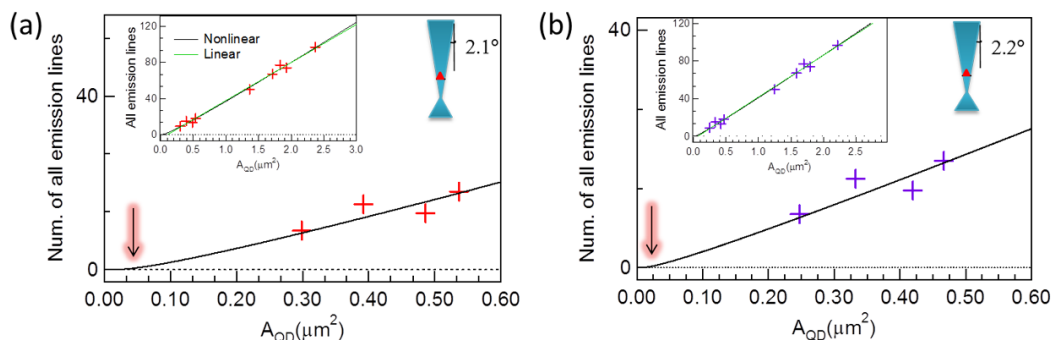


Figure 5.25: Statistics on single exciton emission lines obtained for several size of wires - Measured all lines (cross marks) are plotted with respect to the cross sectional area in the QD plane whose trumpet angles are respectively (a) 2.1° and (b) 2.2° . From nonlinear fits (black lines), emission lines are completely absence in its photoluminescence spectrum at $A_{QD} = 0.016\mu m^2$ for 2.1° and $A_{QD} = 0.006\mu m^2$ for 2.2° . The dead layers are found to have 73 nm and 45 nm thicknesses respectively for 2.1° and 2.2° etching angles. Inset shows a wide range of statistics on single exciton emission lines.

Figure 5.26 presents complete two-dimensional positioning of embedded QDs near the bottom of the wire. To illustrate how the spatial map works, one can check a QD indicated with yellow arrow that is near to the center. Yellow QD shows almost

5. STRAIN-INDUCED OPTOMECHANICAL COUPLING FOR QUANTUM DOTS IN PHOTONIC WIRES

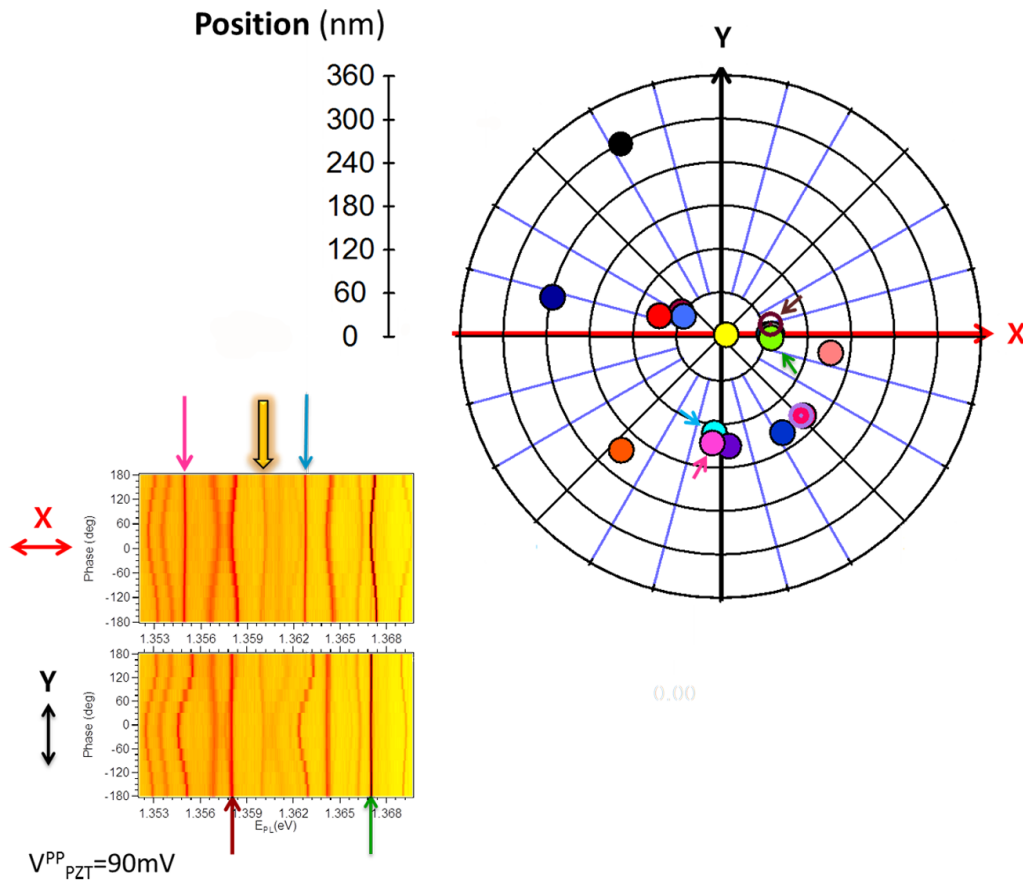


Figure 5.26: QD spatial mapping - Locations of all QDs are indicated by circles with corresponding colors on the cross sectional area of $\pi(360 \text{ nm} \times 360 \text{ nm})$ in the QD plane. We have analyzed 18 emission lines. A complete two-dimensional (x, y) spatial map is acquired in nanometer scales with the dead layer of 60 nm from phase-amplitude polar plots of orthogonally polarized mechanical modes. The stroboscopic data presented on the left side shows the corresponding configuration of QD responses along X - and Y -polarized modes. Here, each photoluminescence is taken with the integration time 10 s at $V_{PZT}^{PP}=90 \text{ mV}$.

5.3 Optomechanical Characterization of GaAs Photonic Wires

no modulation at both orthogonally polarized mechanical modes in stroboscopic data. Regarding the coupling efficiency of QDs in the guided mode, the yellow QD at center is an adequate candidate for QD-based single photon source. As similar examples, blue and pink arrows are marked in the stroboscopic data performed on the X -polarized mode. The emissions show almost no energy shift with the relative phases along the X mechanical polarization while they undergo significant modulations along the Y -polarization. This means that blue and pink QDs are located on the neutral axis of the X -polarization. Consistent with this, similar characteristics are also observed from QDs marked with light green and brown arrows, for example. This time, there are almost no modulations in QD emission lines for the Y polarization whereas the QD lines are modulated for the X polarized mode. Thus, the QDs marked with brown and light green are located on the Y neutral axis. In the following sense, all QDs shown in the photoluminescence spectra are completely positioned in the two-dimensional spatial map of Fig. 5.26.

The QD positions in Fig. 5.26 are all consistent with the identification of QD families followed by the power dependence. As mentioned before, this map also includes the spatial positioning of biexcitonic or charged excitonic states of the same QD. So far all calculations have been done for the QD exciton in previous sections. Then one might doubt about spatial positions of other QD transition (biexciton and charged exciton) in our QD spatial map. However, strain effects entail negligible modifications of the biexciton or charged exciton binding energies, so that X , XX and X^* experience the same shifts. For example, one can check a set of QD lines named 8, 10 and 16 in Fig. 5.27. In the power dependence, two of them show linear behaviors while the one named 10 shows a quadratic behavior. Note that the exciton and charged exciton are found to have linear dependence upon laser power, while for the biexciton it shows quadratic dependence (see Chapter 3). Their relation seems like exciton, biexciton and charged exciton of the same QD. Figure 5.26 shows that the QD family is nicely overlapped within the error bar of 11 nm. Figure 5.27 also shows sets of QD families and their laser power dependences. All other QD families identified in Fig.5.27 are also respectively overlapped within an error of 11 nm in Fig. 5.26. From this identification, the excitonic lines are found to be twelve among eighteen emission lines.

The two-dimensional spatial map allows the extraction of twelve QD locations within the photonic wire with a sub-wavelength accuracy with a scaling error of about

5. STRAIN-INDUCED OPTOMECHANICAL COUPLING FOR QUANTUM DOTS IN PHOTONIC WIRES

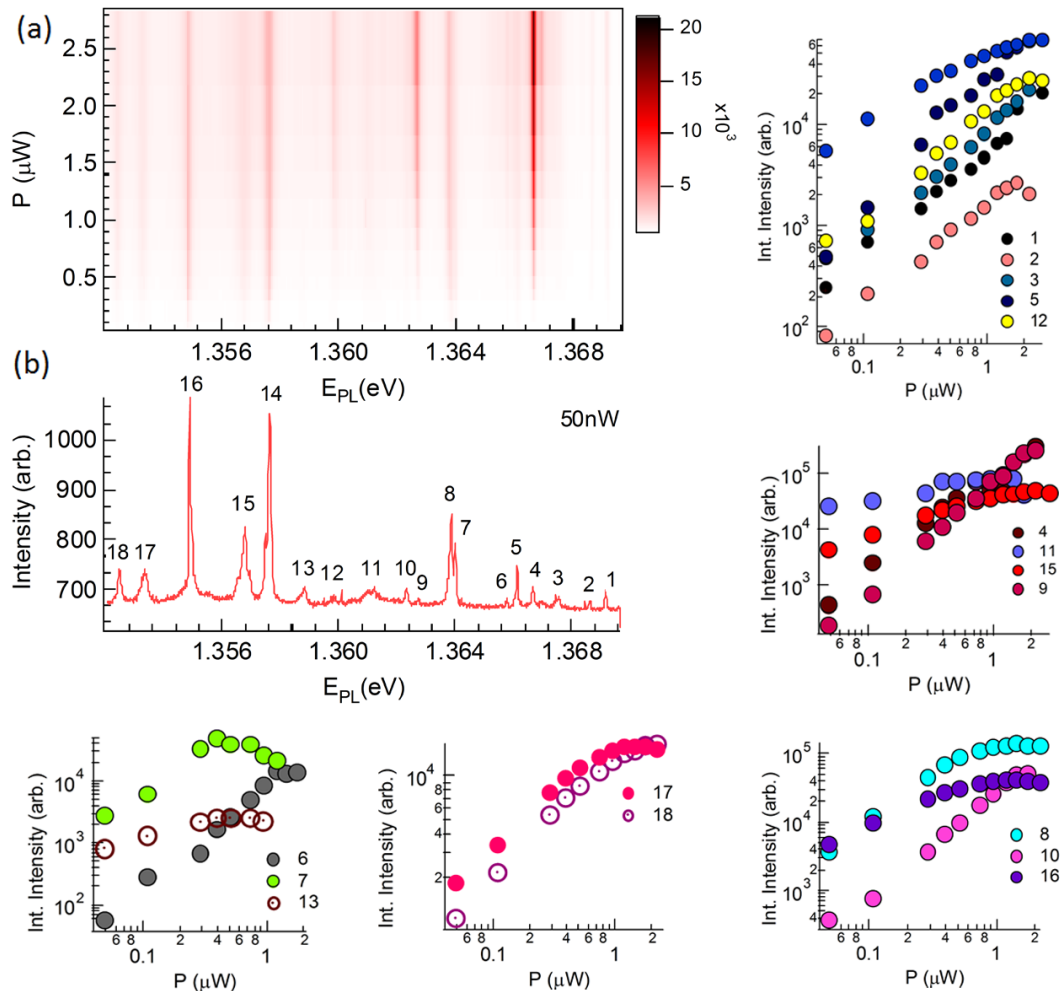


Figure 5.27: Power dependence of single QDs embedded in the GaAs photonic wire of top diameter 1.98 μm - (a) Waterfall graph of power-dependent photoluminescence spectra is plotted; (b) A typical photoluminescence spectrum measured at a low power (50 nW). All photoluminescence spectra are taken with the integration time 10 s under pumping of the InAs wetting layer. Surroundings of color coded plots present the integrated intensity of each QD line as a function of the excitation power.

5.3 Optomechanical Characterization of GaAs Photonic Wires

10%. With this map, one can check embedded QDs and their relative distances in a nanometer scale with an additional pointing error of about 11 nm without destroying the system. In particular, the spatial map can help for finding the best QD candidate to build a single photon source. As seen in Fig. 5.26, we find the QD marked with yellow nicely aligned along the guided optical mode of the wire.

5.3.7 Mechanical Bistability

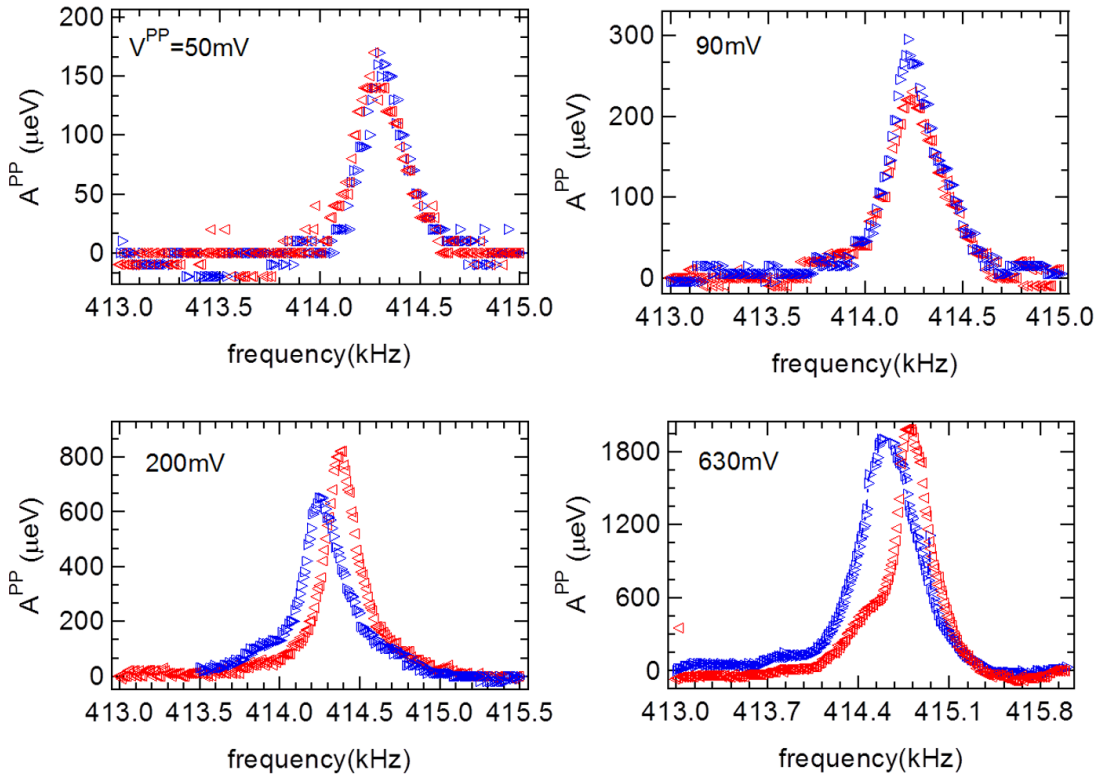


Figure 5.28: Hysteresis phenomenon in the nonlinear frequency response of GaAs photonic wire embedding InAs QDs - Measured peak-to-peak amplitude A_{QD}^{PP} taken from the photoluminescence data is plotted by sweeping the frequency upward (blue triangle) and downward (red triangle) across the first flexural mode of the photonic wire ($D_{Top}=1.98 \mu\text{m}$). The wire is excited by a sinusoidal source at several driving voltages 50mV , 90mV , 200mV and 630mV .

In the previous section, we were able to draw the two-dimensional map of embedded QDs for a wire $D_{Top}=1.98 \mu\text{m}$. A prerequisite for the QD spatial mapping is, that the wire should be accurately brought into a mechanical resonance. So far we found the

5. STRAIN-INDUCED OPTOMECHANICAL COUPLING FOR QUANTUM DOTS IN PHOTONIC WIRES

mechanical resonance in the context of a spectral shift in QD photoluminescence spectra while the driving frequency was swept forward or downward across resonance. As the driving power increases, however, we start to observe a bistable mechanical response of the photonic wire in sweep-up and -down photoluminescence measurements. More precisely, a shift in its resonance frequency is observed by reversing the direction of a frequency sweep. To satisfy the above prerequisite requirement, we need to clarify the driving conditions for which the nonlinear bistable effect is absent.

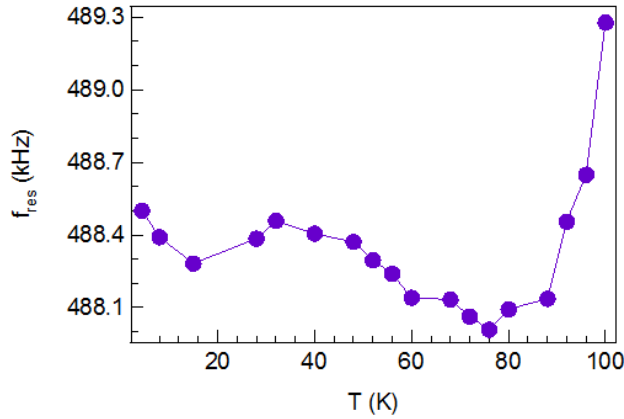


Figure 5.29: Temperature dependence of the mechanical resonance frequency for GaAs photonic wire of $D_{Top}=1.97 \mu\text{m}$ - The wire is excited at $V_{PZT}^{PP}=6 \text{ mV}$. This data was taken with the split-photodiode excited with the laser at 825 nm. The resonance frequency is measured for a fundamental flexural mode of the wire $D_{Top}=1.97 \mu\text{m}$. A central frequency is extracted by fitting the mechanical response with a mechanical lorentzian function.

Figure 5.28 shows the nonlinear bistable effects on the strain-induced spectral shift. The frequency is swept upwards and downwards for nonzero values of the driving voltage. Overview of the frequency responses is given by two-dimensional waterfall plots of photoluminescence spectra in Figs. 5.32, and 5.33. From the sweeping series at different voltages, the peak-to-peak amplitude A_{QD}^{PP} is extracted by fitting with a frequency modulated Lorentzian function. The fitting results are combined and presented in Figs. 5.28 and 5.31.

As seen in Fig.5.28, our system seems to be in the linear regime at around $V_{PZT}^{PP}=50 \text{ mV}$. A low driving voltage of $V_{PZT}^{PP}=50 \text{ mV}$ brings both of sweep-up and -down responses onto resonance at the same driving frequency. The A_{QD}^{PP} follows exactly the same curve

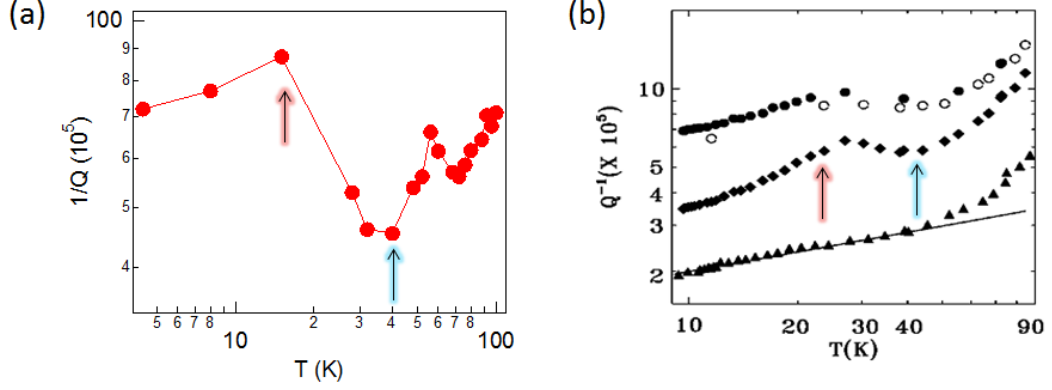


Figure 5.30: Temperature dependence of energy dissipation for GaAs photonic wire of $D_{Top}=1.97 \mu\text{m}$ - (a) Temperature dependence of energy dissipation $1/Q$. The system is driven at 6 mV. The energy dissipation $1/Q$ is extracted from a lorentzian fitting with the mechanical response for a fundamental flexural mode. (b) Typical temperature dependence of the dissipation for three normal mode of a GaAs resonator (127).

regardless of sweeping directions. On that account, the QD spatial map was drawn by analyzing the stroboscopic data measured at $V_{PZT}^{PP}=50$ mV in the previous section. By increasing the driving voltage, our technique to find the mechanical resonance becomes noticeably complicated. As shown in Fig.5.28, the frequency sweeps develop the hysteresis clearly splitting the mechanical resonance into two separate and distinct states at 200 mV. To be on the safe side, we excite the system with a driving voltage well below 200 mV on the purpose of the QD spatial mapping.

Here we will not go into details about the nonlinear bistable effects. Just to illustrate the underlying physics of the bistability, driving the wire to the resonance frequency heats up the wire, and the wire heating modifies the Young's modulus. As a consequence, the resonance frequency of the wire is shifted. As discussed in Chapter 3, the temperature heating shifts the QD emission line to the low energy side. We observed red-shifted photoluminescence lines at mechanical resonances corresponding to less than 2 K changes in temperature. Figure 5.29 plots the temperature-dependent shift in the resonance frequency. When the temperature increases from 4 up to 8 K, the resonance frequency shifts by 100 Hz. Figure 5.30(a) shows the temperature dependence of the energy dissipation $1/Q$ for a wire of $D_{Top}=1.97 \mu\text{m}$. The energy dissipation increases in the low temperature region below 20 K and the high temperature region higher than 40 K. Comparing to a previous characterization of GaAs resonators (127),

5. STRAIN-INDUCED OPTOMECHANICAL COUPLING FOR QUANTUM DOTS IN PHOTONIC WIRES

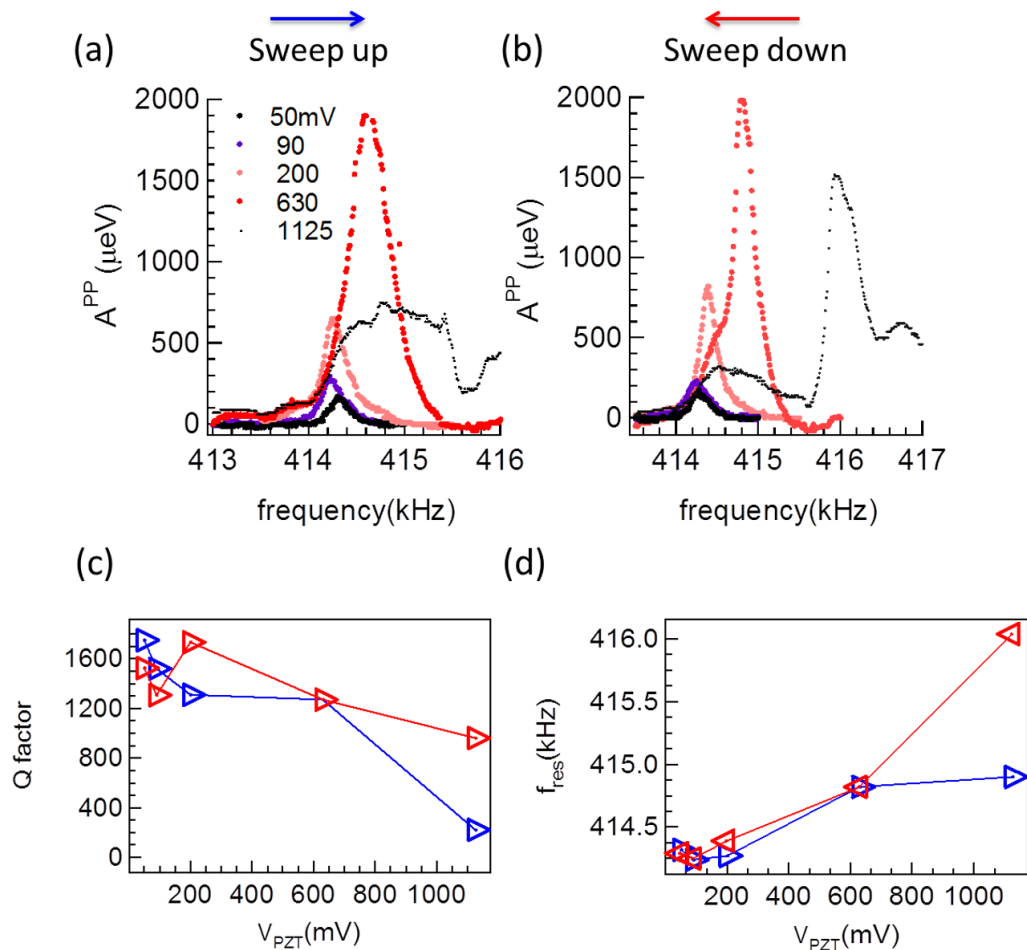


Figure 5.31: Comparison of the strain-induced spectral shift for up- and down-sweep experiments of Fig.5.28 - The strain-induced spectral shift A^{PP} is plotted respectively for the up-sweep (a) and the down-sweep (b) by varying amplitudes 50, 90, 200, 630 and 1125mV. By fitting the mechanical response with a Lorentzian function, (c) Q factor and (d) the resonance frequency shift are extracted versus the piezo driving voltage V_{PZT} . Blue and red triangles correspond to up- and down-sweep measurements respectively.

the overall trend observed in Fig. 5.30(a) is quite typical.

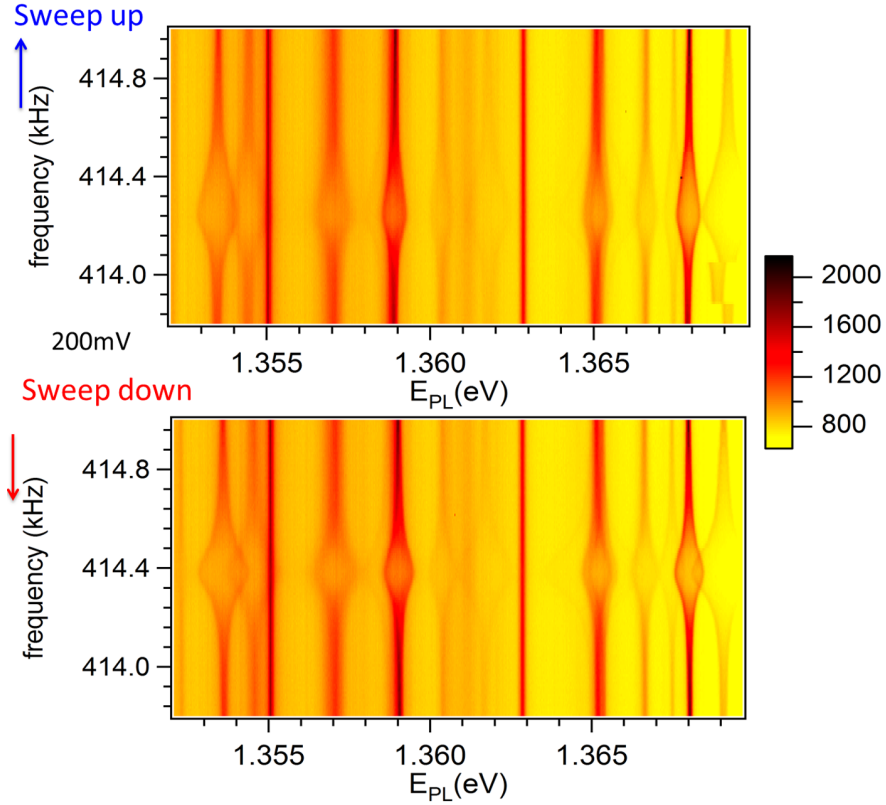


Figure 5.32: Color coded waterfall plot of the photoluminescence spectra for forward and reversed sweeping in the frequency domain. - The photonic wire is excited by a sinusoidal source of $V_{PZT}^{PP}=200$ mV. The photoluminescence spectra is taken for the integration time 10 s at low laser power 830 nW. The vibrational mode shows a relative good symmetry for both resonances.

Figures 5.31 (a) and (b) plot the driving voltage dependences of A_{QD}^{PP} respectively for upward and downward frequency scans. By fitting each resonance curve with a Lorentzian function, one can extract the Q -factor in terms of the resonance frequency f_{res} and its full width at half maximum Δf . Figure 5.31(c) plots the driving power dependence of Q -factor for sweep-up and -down measurements. As discussed in section 5.3.2, Q -factor was measured to be 870 at $V_{PZT}^{PP}=50$ mV for the first flexural modes of the wire using the network analyzer. At the same driving voltage, Q -factor of 1600 is extracted from the frequency-dependent photoluminescence data. The sweeping experiment enables us to measure the Q -factor improved by almost a factor of two. It could

5. STRAIN-INDUCED OPTOMECHANICAL COUPLING FOR QUANTUM DOTS IN PHOTONIC WIRES

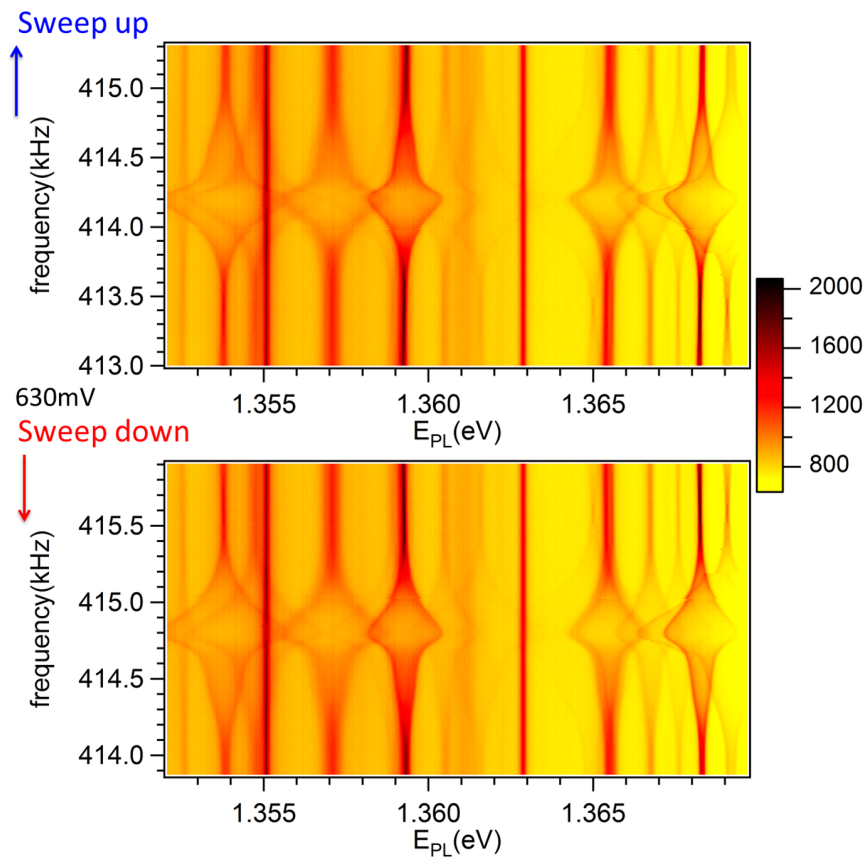


Figure 5.33: Strain effects on the QD emission lines at 630 mV - The photonic wire is driven at 630 mV. Forward and reversed frequency sweeps show the marked asymmetry in the A^{PP} evolution.

be that different laser power makes this difference in Q -factor. For the split-photodiode experiment, we use a laser emitting at 825 nm which can heat up the wire due to the absorption by the wetting layer. Here, the laser power is around $\sim 50 \mu\text{W}$. Compared to a few tenth of nanowatts laser power used in the photoluminescence measurement, an order of three higher power can heat up the wire significantly, thereby reducing its Q -factor. Figure 5.31(d) displays the driving power dependence of the resonant frequency respectively obtained for upward and downward frequency sweeps. Increasing the driving power shifts the mechanical resonance frequency to the high frequency side with larger peak-to-peak amplitude A_{QD}^{PP} (see, Fig.5.31). In contrast to the previous temperature dependence shown in Fig. 5.30, energy dissipation (Q^{-1}) is found to increase in Fig.5.31 by increasing the actuation voltage. In general, higher driving power more heats up the system. Again, the photoluminescence measurement can't directly be compared with the data taken with the split-photodiode. To avoid the laser heating problem, our work is in progress using the Toptica laser emitting at 930 nm.

5.4 Chapter Summary

In this Chapter, we have discussed the dynamical strain-mediated coupling of QDs with the mechanical motion of a trumpet-like GaAs photonic wire. First, we discussed the experimental setup employed in optomechanical studies covered in this Chapter. Two fundamental resonance frequencies of the wire were characterized for 435 kHz and 503 kHz, which were proven to be orthogonally and linearly polarized modes. The mechanical oscillation induced dynamical stress on the QDs which modulated in turn the QD emission energy. We observed a camel-back shape spectral modulation of QDs at mechanical frequencies of the first flexural modes of the wire. By performing the stroboscopic photoluminescence spectroscopy at the mechanical resonance frequencies, we isolated the wire oscillation at a given phase, thereby choosing the specific value of QD tuning. Full time-dependent spectral lineshape was reconstructed by varying the phase between the optical and mechanical excitations. With careful phase adjustments, we tuned the QD emission over 0.5 meV. In particular, two QDs which were located in the same photonic wire but experiencing different strains were brought into resonance. From the strength and phase of this coupling, we were able to draw the two-dimensional spatial map of embedded QDs in the photonic wire with a sub-wavelength accuracy.

5. STRAIN-INDUCED OPTOMECHANICAL COUPLING FOR QUANTUM DOTS IN PHOTONIC WIRES

To confirm the reliability of our QD spatial map, we clarified the mechanical excitation condition in which the nonlinear bistable effect is absent.

6

Conclusions and Outlook

In the framework of this thesis, single QD devices were studied by optical means. Starting with a general description of self-assembled InAs QDs, two types of single QD devices were presented in Chapter 2.

The first approach was a tapered photonic wire embedding single InAs QDs whose efficiency of $\beta \sim 90\%$ had already been proved (38). Revisiting the photoluminescence spectra of single QDs presented in Ref.(38), we investigated several optical properties of the single QDs. The single emitter spectroscopy techniques were discussed in Chapter 3. The charged and neutral states of the QD were identified and selectively excited for further usage of isolated two-level systems. The ground states of excitonic species were found to rather change at 20 K in terms of emission energies.

The change of QD emission energies around 20 K was further investigated with the new generation of trumpet-like photonic wires in Chapter 4. We strikingly observed a continuous temporal blue-drift of the QD emission energy. The temperature effect on this phenomenon revealed the adsorption peak around 20 K, which was the adsorption of O₂ on GaAs. We then attributed the blue drift to oxygen adsorption onto the sidewall of the wire, which modified the surface charge and hence the electric field seen by the QD. This observation is in good agreement with previous temperature studies with a tapered photonic wire. Moreover, we demonstrated a proper treatment of the GaAs photonic nanowire surface to suppress the drift. This was the first study of the spectral stability of photonic wires embedding QDs, crucial for resonant quantum optics experiments. As an alternative, we used the temporal drift to tune QD emission energies. In a controlled way, we tuned into resonance two different QDs which were

6. CONCLUSIONS AND OUTLOOK

located within the same photonic nanowire. The time-dependent QD tuning could be well reproduced after warming up to room temperature and re-cooling down the sample.

In the last part of this work, we studied the influence of the stress on single QDs contained in a trumpet-like GaAs photonic wire. We applied the stress to buried single QDs close to the bottom by exciting mechanical vibrating of the wire. We monitored the influence of stress via the modulation of excitonic transitions appearing in photoluminescence spectra. In time-integrated photoluminescence spectra, QD emission energies were observed to shift over a range of few meV of the mechanical resonance of the wire. The measured spectral modulation is a first signature of strain-mediated coupling between a trumpet-like photonic wire and embedded QDs. To choose a specific value of the QD tuning, stroboscopic experiments were performed. With the stroboscopic techniques, we isolated a certain state of oscillating wire and thereby selected a value of QD emission energies. The QD tuning range investigated in this work was about 5 meV. The sinusoidal oscillation of QD emission energies were fully resolved with a careful phase adjustment. As a highlight of our study, we managed to bring two different QDs contained in the same wire into resonance by controlling their relative phase. From the spectral shift in photoluminescence spectra, we calculated absolute values for the stress in the QD plane. We showed that the stress value depends on the position of buried QDs in the photonic wire. Since the numerical calculation was not precise enough for estimating experimental results, we extract the two-dimensional spatial positioning of embedded QDs by assuming a uniform distribution of QDs inside the wire. The position uncertainty was calculated to be ± 10 nm due to the scaling. It was found that QD's relative spacing has an error bar of about 11 nm. The investigation of the strain-mediated tuning of QDs can, therefore, be an effective tool to explore the QD positions without destroying the sample.

In the future, it will be interesting to tune QD emission statically. This could be done with nano-manipulators that would bend the wire in a specific position. This would allow the tuning of QD emission with respect to external reference. This would also enable us to bring into resonance two QDs within the same one-dimensional photonic wire. In the context of optomechanics, an optimized design of our nanostructure might be an effective hybrid system to probe and control a nano-mechanical oscillator using optics.

References

- [1] B. LOUNIS AND M. ORRIT. **Single-photon sources**. *Reports on Progress in Physics*, **68**:1129, 2005.
- [2] G. BRASSARD C.H. BENNETT AND A. K. EKERT. **Quantum cryptography**. *Sci. Am.*, **267**:50–57, 1992.
- [3] E. WAKS, K. INOUE, C. SANTORI, D. FATTAL, J. VUCKOVIC, G.S. SOLOMON, AND Y. YAMAMOTO. **Quantum cryptography with a photon turnstile**. *Nature*, **420**(6917):762, 2002.
- [4] E. KNILL, R. LAFLAMME, G.J. MILBURN, ET AL. **A scheme for efficient quantum computation with linear optics**. *nature*, **409**(6816):46–52, 2001.
- [5] ALEXIA AUFFÈVES-GARNIER, CHRISTOPH SIMON, JEAN-MICHEL GÉRARD, AND JEAN-PHILIPPE POIZAT. **Giant optical non-linearity induced by a single two-level system interacting with a cavity in the Purcell regime**. *Phys. Rev. A*, **75**(5):053823, May 2007.
- [6] A. MIGDALL. **Introduction to Journal of Modern Optics special issue on single-photon: detectors, applications, and measurement methods**. *Journal of Modern Optics*, **51**(9-10):1265–1266, 2004.
- [7] J.P. DOWLING. **Quantum optical metrology—the low-down on high-N00N states**. *Contemporary physics*, **49**(2):125–143, 2008.
- [8] HJ KIMBLE, M. DAGENAIS, AND L. MANDEL. **Photon antibunching in resonance fluorescence**. *Physical Review Letters*, **39**(11):691–695, 1977.
- [9] F. DIEDRICH AND H. WALTHER. **Nonclassical radiation of a single stored ion**. *Physical review letters*, **58**(3):203–206, 1987.
- [10] A. KUHN, M. HENNRICH, AND G. REMPE. **Deterministic single-photon source for distributed quantum networking**. *Physical review letters*, **89**(6):67901, 2002.
- [11] M. KELLER, B. LANGE, K. HAYASAKA, W. LANGE, AND H. WALTHER. **Continuous generation of single photons with controlled waveform in an ion-trap cavity system**. *Nature*, **431**(7012):1075–1078, 2004.
- [12] T. BASCHÉ, WE MOERNER, M. ORRIT, AND H. TALON. **Photon antibunching in the fluorescence of a single dye molecule trapped in a solid**. *Physical review letters*, **69**(10):1516–1519, 1992.
- [13] L. FLEURY, J.M. SEGURA, G. ZUMOFEN, B. HECHT, AND UP WILD. **Nonclassical photon statistics in single-molecule fluorescence at room temperature**. *Physical review letters*, **84**(6):1148–1151, 2000.
- [14] B. LOUNIS, WE MOERNER, ET AL. **Single photons on demand from a single molecule at room temperature**. *Nature*, **407**(6803):491–493, 2000.
- [15] R. BROURI, A. BEVERATOS, J.P. POIZAT, AND P. GRANGIER. **Photon antibunching in the fluorescence of individual color centers in diamond**. *Optics Letters*, **25**(17):1294–1296, 2000.
- [16] C. KURTSIEFER, S. MAYER, P. ZARDA, AND H. WEINFURTER. **Stable solid-state source of single photons**. *Physical Review Letters*, **85**(2):290–293, 2000.
- [17] P. MICHLER, A. KIRAZ, C. BECHER, WV SCHOENFELD, PM PETROFF, L. ZHANG, E. HU, AND A. İMAMOĞLU. **A quantum dot single-photon turnstile device**. *Science*, **290**(5500):2282–2285, 2000.
- [18] C. SANTORI, M. PELTON, G. SOLOMON, Y. DALE, AND Y. YAMAMOTO. **Triggered single photons from a quantum dot**. *Physical Review Letters*, **86**(8):1502–1505, 2001.
- [19] V. ZWILLER, H. BLOM, P. JONSSON, N. PANEV, S. JEPPESEN, T. TSEGAYE, E. GOOBAR, M.E. PISTOL, L. SAMUELSON, AND G. BJÖRK. **Single quantum dots emit single photons at a time: Antibunching experiments**. *Applied Physics Letters*, **78**:2476, 2001.
- [20] P. LODAHL, A.F. VAN DRIEL, I.S. NIKOLAEV, A. IRMAN, K. OVERGAAG, D. VANMAEKELBERGH, AND W.L. VOS. **Controlling the dynamics of spontaneous emission from quantum dots by photonic crystals**. *Nature*, **430**(7000):654–657, 2004.
- [21] A.J. SHIELDS. **Semiconductor quantum light sources**. *Nature Photonics*, **1**(4):215–223, 2007.
- [22] EM PURCELL. **Spontaneous emission probabilities at radio frequencies**. *Physical Review*, **69**:681, 1946.
- [23] D. KLEPPNER. **Inhibited spontaneous emission**. *Physical Review Letters*, **47**(4):233–236, 1981.
- [24] R.G. HULET, E.S. HILFER, AND D. KLEPPNER. **Inhibited spontaneous emission by a Rydberg atom**. *Physical review letters*, **55**(20):2137–2140, 1985.
- [25] P. GOY, JM RAIMOND, M. GROSS, AND S. HAROCHE. **Observation of cavity-enhanced single-atom spontaneous emission**. *Physical review letters*, **50**(24):1903, 1983.
- [26] G.S. JP REITHMAIER, A. LÖFFLER, C. HOFMANN, S. KUHN, S. REITZENSTEIN, LV KELDYSH, VD KULAKOVSKII, AND A.F. TL REINECKE. **Strong coupling in a single quantum dot–semiconductor microcavity system**. *Nature*, **432**(7014):197–200, 2004.
- [27] E. MOREAU, I. ROBERT, JM GÉRARD, I. ABRAM, L. MANIN, AND V. THIERRY-MIEG. **Single-mode solid-state single photon source based on isolated quantum dots in pillar microcavities**. *Applied Physics Letters*, **79**:2865, 2001.

REFERENCES

- [28] W.H. CHANG, W.Y. CHEN, H.S. CHANG, T.P. HSIEH, J.I. CHYI, AND T.M. HSU. **Efficient single-photon sources based on low-density quantum dots in photonic-crystal nanocavities.** *Physical review letters*, **96**(11):117401, 2006.
- [29] JM GÉRARD, B. SERMAGE, B. GAYRAL, B. LEGRAND, E. COSTARD, AND V. THIERRY-MIEG. **Enhanced spontaneous emission by quantum boxes in a monolithic optical microcavity.** *Physical review letters*, **81**(5):1110–1113, 1998.
- [30] E. MOREAU, I. ROBERT, L. MANIN, V. THIERRY-MIEG, JM GÉRARD, AND I. ABRAM. **A single-mode solid-state source of single photons based on isolated quantum dots in a micropillar.** *Physica E: Low-dimensional Systems and Nanostructures*, **13**(2):418–422, 2002.
- [31] S. STRAUF, N.G. STOLTZ, M.T. RAKHER, L.A. COLDREN, P.M. PETROFF, AND D. BOUWMEESTER. **High-frequency single-photon source with polarization control.** *Nature photonics*, **1**(12):704–708, 2007.
- [32] H. SAITO, K. NISHI, I. OGURA, S. SUGOU, AND Y. SUGIMOTO. **Room-temperature lasing operation of a quantum-dot vertical-cavity surface-emitting laser.** *Applied physics letters*, **69**:3140, 1996.
- [33] B. GAYRAL, JM GERARD, A. LEMAITRE, C. DUPUIS, L. MANIN, AND JL PELOUARD. **High-Q wet-etched GaAs microdisks containing InAs quantum boxes.** *Applied physics letters*, **75**:1908, 1999.
- [34] A. KRESS, F. HOFBAUER, N. REINELT, M. KANIBER, HJ KRENNER, R. MEYER, G. BÖHM, AND JJ FINLEY. **Manipulation of the spontaneous emission dynamics of quantum dots in two-dimensional photonic crystals.** *Physical Review B*, **71**(24):241304, 2005.
- [35] DIRK ENGLUND, DAVID FATTAL, EDO WAKS, GLENN SOLOMON, BINGYANG ZHANG, TOSHIHIRO NAKAOKA, YASUHIKO ARAKAWA, YOSHIHISA YAMAMOTO, AND JELENA VUČKOVIĆ. **Controlling the Spontaneous Emission Rate of Single Quantum Dots in a Two-Dimensional Photonic Crystal.** *Phys. Rev. Lett.*, **95**(1):013904, Jul 2005.
- [36] SUSUMU NODA, MASAYUKI FUJITA, AND TAKASHI ASANO. **Spontaneous-emission control by photonic crystals and nanocavities.** *Nat Photon*, **1**(8):449–458, aug 2007.
- [37] T. LUND-HANSEN, S. STOBBE, B. JULSGAARD, H.T. NIELSEN, T. SÜNNER, M. KAMP, A. FORCHEL, AND P. LODAHL. **Experimental realization of highly efficient broadband coupling of single quantum dots to a photonic crystal waveguide.** *Physical review letters*, **101**(11), 2008.
- [38] JULIEN CLAUDON, JOEL BLEUSE, NITIN SINGH MALIK, MAELA BAZIN, PERINE JAFFRENNOU, NIELS GREGERSEN, CHRISTOPHE SAUVAN, PHILIPPE LALANNE, AND JEAN-MICHEL GERARD. **A highly efficient single-photon source based on a quantum dot in a photonic nanowire.** *Nat Photon*, **4**(3):174–177, mar 2010.
- [39] M. SOLJAČIĆĆUTE AND JD JOANNOPOULOS. **Enhancement of nonlinear effects using photonic crystals.** *Nature materials*, **3**(4):211–219, 2004.
- [40] P. GRANGIER, J.A. LEVENSON, AND J.P. POIZAT. **Quantum non-demolition measurements in optics.** *Nature*, **396**(6711):537–542, 1998.
- [41] K. NEMOTO AND WJ MUNRO. **Nearly deterministic linear optical controlled-NOT gate.** *Physical review letters*, **93**(25):250502, 2004.
- [42] W. J. MUNRO, KAE NEMOTO, R. G. BEAUSOLEIL, AND T. P. SPILLER. **High-efficiency quantum-nondemolition single-photon-number-resolving detector.** *Phys. Rev. A*, **71**:033819, Mar 2005.
- [43] Q.A. TURCHETTE, CJ HOOD, W. LANGE, H. MABUCHI, AND H.J. KIMBLE. **Measurement of conditional phase shifts for quantum logic.** *Physical Review Letters*, **75**(25):4710–4713, 1995.
- [44] JT SHEN AND S. FAN. **Coherent photon transport from spontaneous emission in one-dimensional waveguides.** *Optics letters*, **30**(15):2001–2003, 2005.
- [45] G. SALLEN, A. TRIBU, T. AICHELE, R. ANDRÉ, L. BESOMBES, C. BOUGEROL, M. RICHARD, S. TATARENKO, K. KHENG, AND J.P. POIZAT. **Subnanosecond spectral diffusion measurement using photon correlation.** *Nature Photonics*, **4**(10):696–699, 2010.
- [46] H. LIM, S. TSAO, W. ZHANG, AND M. RAZEGHI. **High-performance InAs quantum-dot infrared photodetectors grown on InP substrate operating at room temperature.** *Applied physics letters*, **90**(13):131112–131112, 2007.
- [47] M. SUGAWARA AND M. USAMI. **Quantum dot devices: Handling the heat.** *Nature Photonics*, **3**(1):30–31, 2009.
- [48] J.D. SONG, W.J. CHOI, J.I. LEE, J.C. JUNG, I.K. HAN, ET AL. **High power broadband InGaAs/GaAs quantum dot superluminescent diodes.** *Electronics Letters*, **39**(11):863–865, 2003.
- [49] H. DREXLER, D. LEONARD, W. HANSEN, JP KOTTHAUS, AND PM PETROFF. **Spectroscopy of quantum levels in charge-tunable InGaAs quantum dots.** *Physical review letters*, **73**(16):2252–2255, 1994.
- [50] C. COHEN-TANNOUDJI. **B. Diu, and F. Laloe.** *Quantum Mechanics*, **1**, 1977.
- [51] D.D. AWSCHALOM AND J.M. KIKKAWA. **Electron spin and optical coherence in semiconductors.** *Physics Today*, **52**:33–39, 1999.
- [52] S. TRUMM, M. WESSELI, HJ KRENNER, D. SCHUH, M. BICHLER, JJ FINLEY, AND M. BETZ. **Spin-preserving ultrafast carrier capture and relaxation in InGaAs quantum dots.** *Applied Physics Letters*, **87**:153113, 2005.
- [53] M. WESSELI, C. RUPPERT, S. TRUMM, HJ KRENNER, JJ FINLEY, AND M. BETZ. **Nonlinear optical response of a single self-assembled InGaAs quantum dot: A femtojoule pump-probe experiment.** *Applied physics letters*, **88**:203110, 2006.
- [54] R. HEITZ, A. KALBURGE, Q. XIE, M. GRUNDMANN, P. CHEN, A. HOFFMANN, A. MADHUKAR, AND D. BIMBERG. **Excited states and energy relaxation in stacked InAs/GaAs quantum dots.** *Physical Review B*, **57**(15):9050, 1998.

REFERENCES

- [55] L. BESOMBES, J. J. BAUMBERG, AND J. MOTOHISA. **Coherent Spectroscopy of Optically Gated Charged Single InGaAs Quantum Dots.** *Phys. Rev. Lett.*, **90**:257402, Jun 2003.
- [56] GREGORY SALLEN. *Spectroscopie optique de boites quantiques de CdSe inserees dans des nanofils de ZnSe.* PhD thesis, Universite Joseph Fourier, 2009.
- [57] S. SEIDL, M. KRONER, PA DALGARNO, A. HÖGELE, JM SMITH, M. EDIGER, BD GERARDOT, J.M. GARCIA, P.M. PETROFF, K. KARRAI, ET AL. **Absorption and photoluminescence spectroscopy on a single self-assembled charge-tunable quantum dot.** *Physical Review B*, **72**(19):195339, 2005.
- [58] RJ WARBURTON, CS DÜRR, K. KARRAI, JP KOTTHAUS, G. MEDEIROS-RIBEIRO, AND PM PETROFF. **Charged excitons in self-assembled semiconductor quantum dots.** *Physical review letters*, **79**(26):5282–5285, 1997.
- [59] JJ FINLEY, AD ASHMORE, A. LEMAÎTRE, DJ MOWBRAY, MS SKOLNICK, IE ITSKEVICH, PA MAKSYM, M. HOPKINSON, AND TF KRAUSS. **Charged and neutral exciton complexes in individual self-assembled In (Ga) As quantum dots.** *Physical Review B*, **63**(7):073307, 2001.
- [60] K. HENNESSY, A. BADOLATO, M. WINGER, D. GERACE, M. ATATÛRE, S. GULDE, S. FÄLT, A.I. EL HU, ET AL. **Quantum nature of a strongly coupled single quantum dot-cavity system.** *Nature*, **445**(7130):896–899, 2007.
- [61] I. FRIEDLER, C. SAUVAN, J. P. HUGONIN, P. LALANNE, J. CLAUDON, AND J. M. GÉRARD. **Solid-state single photon sources: the nanowire antenna.** *Opt. Express*, **17**(4):2095–2110, Feb 2009.
- [62] M.O. SCULLY AND M.S. ZUBAIRY. **Quantum Optics (Cambridge. Ch, 4:17, 1997.**
- [63] JOËL BLEUSE, JULIEN CLAUDON, MEGAN CREASEY, NITIN. S. MALIK, JEAN-MICHEL GÉRARD, IVAN MAKSYMOM, JEAN-PAUL HUGONIN, AND PHILIPPE LALANNE. **Inhibition, Enhancement, and Control of Spontaneous Emission in Photonic Nanowires.** *Phys. Rev. Lett.*, **106**(10):103601, Mar 2011.
- [64] N.S. MALIK. *Les fils photoniques : une geometrie innovante pour la realisation de sources de lumiere quantique brillantes.* PhD thesis, Grenoble university, 2011.
- [65] V. ZWILLER, T. AICHELE, AND O. BENSON. **Single-photon Fourier spectroscopy of excitons and biexcitons in single quantum dots.** *Physical Review B*, **69**(16):165307, 2004.
- [66] T. SAIKI. **Visualizing exciton wavefunctions confined in a quantum dot.**
- [67] K. MATSUDA, T. SAIKI, S. NOMURA, M. MIHARA, Y. AOYAGI, S. NAIR, AND T. TAKAGAHARA. **Near-Field Optical Mapping of Exciton Wave Functions in a GaAs Quantum Dot.** *Phys. Rev. Lett.*, **91**:177401, Oct 2003.
- [68] Y.Y. PETER AND M. CARDONA. *Fundamentals of semiconductors: physics and materials properties.* Springer Verlag, 2010.
- [69] O. VERZELEN, R. FERREIRA, AND G. BASTARD. **Excitonic Polarons in Semiconductor Quantum Dots.** *Phys. Rev. Lett.*, **88**:146803, Mar 2002.
- [70] ARNO HARTMANN, YANN DUCOMMUN, ELI KAPON, ULRICH HOHENESTER, AND ELISA MOLINARI. **Few-Particle Effects in Semiconductor Quantum Dots: Observation of Multicharged Excitons.** *Phys. Rev. Lett.*, **84**:5648–5651, Jun 2000.
- [71] X. FAN, T. TAKAGAHARA, JE CUNNINGHAM, AND H. WANG. **Pure dephasing induced by exciton-phonon interactions in narrow GaAs quantum wells.** *Solid state communications*, **108**(11):857–861, 1998.
- [72] Y. P. VARSHNI. **Unknown Title.** *Phys. Rev. B*, **2**:3952, 1970.
- [73] Y. P. VARSHNI. **Unknown Title.** *Physica (Utrecht)*, **34**:149, 1967.
- [74] M. BAYER AND A. FORCHEL. **Temperature dependence of the exciton homogeneous linewidth in In_{0.60}Ga_{0.40}As/GaAs self-assembled quantum dots.** *Phys. Rev. B*, **65**:041308, Jan 2002.
- [75] C. KAMMERER, C. VOISIN, G. CASSABOIS, C. DELALANDE, PH. ROUSSIGNOL, F. KLOPF, J. P. REITHMAIER, A. FORCHEL, AND J. M. GÉRARD. **Line narrowing in single semiconductor quantum dots: Toward the control of environment effects.** *Phys. Rev. B*, **66**:041306, Jul 2002.
- [76] B. URBASZEK, E. J. MCGHEE, M. KRÜGER, R. J. WARBURTON, K. KARRAI, T. AMAND, B. D. GERARDOT, P. M. PETROFF, AND J. M. GARCIA. **Temperature-dependent linewidth of charged excitons in semiconductor quantum dots: Strongly broadened ground state transitions due to acoustic phonon scattering.** *Phys. Rev. B*, **69**:035304, Jan 2004.
- [77] P. BORRI, W. LANGBEIN, U. WOGGON, V. STAVARACHE, D. REUTER, AND A. D. WIECK. **Exciton dephasing via phonon interactions in InAs quantum dots: Dependence on quantum confinement.** *Phys. Rev. B*, **71**:115328, Mar 2005.
- [78] C. KAMMERER, G. CASSABOIS, C. VOISIN, M. PERRIN, C. DELALANDE, P. ROUSSIGNOL, AND JM GÉRARD. **Interferometric correlation spectroscopy in single quantum dots.** *Applied Physics Letters*, **81**:2737, 2002.
- [79] C.M. SANTORI. *Generation of nonclassical light using semiconductor quantum dots.* PhD thesis, stanford university, 2003.
- [80] DIRK ENGLUND, ANDREI FARAON, ILYA FUSHMAN, NICK STOLTZ, PIERRE PETROFF, AND JELENA VUCKOVIC. **Controlling cavity reflectivity with a single quantum dot.** *Nature*, **450**(7171):857–861, dec 2007.
- [81] THOMAS M. BABINEC, HAUSMANNBIRGIT J. M., MUGHEES KHAN, YINAN ZHANG, JERONIMO R. MAZE, PHILIP R. HEMMER, AND MARKO LONCAR. **A diamond nanowire single-photon source.** *Nat Nano*, **5**(3):195–199, mar 2010.
- [82] O. DEMICHEL, M. HEISS, J. BLEUSE, H. MARIETTE, AND A. FONTCUBERTA I MORRAL. **Impact of surfaces on the optical properties of GaAs nanowires.** *Applied Physics Letters*, **97**(20):201907, 2010.

REFERENCES

- [83] YAPING DAN, KWANYONG SEO, KUNIHARU TAKEI, JHIM H. MEZA, ALI JAVEY, AND KENNETH B. CROZIER. **Dramatic Reduction of Surface Recombination by in Situ Surface Passivation of Silicon Nanowires.** *Nano Letters*, **11**(6):2527–2532, 2011.
- [84] Y. IIMURA, T. SHIRAIISHI, H. TAKASUGI, AND M. KAWABE. **The origin of a highly resistive layer at a growth-interrupted interface of GaAs grown by molecular-beam epitaxy.** *Journal of applied physics*, **61**(5):2095–2097, 1987.
- [85] S. TANAKA, S. D. MORE, J. MURAKAMI, M. ITOH, Y. FUJII, AND M. KAMADA. **Surface photovoltage effects on p-GaAs (100) from core-level photoelectron spectroscopy using synchrotron radiation and a laser.** *Phys. Rev. B*, **64**(15):155308, Sep 2001.
- [86] P. W. FRY, I. E. ITSKEVICH, D. J. MOWBRAY, M. S. SKOLNICK, J. J. FINLEY, J. A. BARKER, E. P. O'REILLY, L. R. WILSON, I. A. LARKIN, P. A. MAKSYM, M. HOPKINSON, M. AL-KHAFAJI, J. P. R. DAVID, A. G. CULLIS, G. HILL, AND J. C. CLARK. **Inverted Electron-Hole Alignment in InAs-GaAs Self-Assembled Quantum Dots.** *Phys. Rev. Lett.*, **84**(4):733–736, Jan 2000.
- [87] B. D. GERARDOT, S. SEIDL, P. A. DALGARNO, R. J. WARBURTON, D. GRANADOS, J. M. GARCIA, K. KOWALIK, O. KREBS, K. KARRAI, A. BADOLATO, AND P. M. PETROFF. **Manipulating exciton fine structure in quantum dots with a lateral electric field.** *Applied Physics Letters*, **90**(4):041101, 2007.
- [88] Y. CHEN, F. STEPNIAK, J. M. SEO, S. E. HARVEY, AND J. H. WEAVER. **Effects of surface band bending on low-energy photon-induced oxidation of GaAs(110).** *Phys. Rev. B*, **43**(14):12086–12089, May 1991.
- [89] H. NIENHAUS AND W. MÖNCH. **Physisorption and chemisorption of O₂ on GaAs (110) surfaces: a Kelvin-probe study.** *Applied surface science*, **65**:632–637, 1993.
- [90] STEVEN G. ANDERSON, T. KOMEDA, J. M. SEO, C. CAPASSO, G. D. WADDILL, P. J. BENNING, AND J. H. WEAVER. **O₂/GaAs(110) interface formation at 20 K: Photon-induced reaction and desorption.** *Phys. Rev. B*, **42**(8):5082–5092, Sep 1990.
- [91] J. W. GADZUK. **Resonance vibrational excitation in electron-energy-loss spectroscopy of adsorbed molecules.** *Phys. Rev. B*, **31**(10):6789–6791, May 1985.
- [92] J. E. DEMUTH, D. SCHMEISSER, AND PH. AVOURIS. **Resonance Scattering of Electrons from N₂, CO, O₂, and H₂ Adsorbed on a Silver Surface.** *Phys. Rev. Lett.*, **47**(16):1166–1169, Oct 1981.
- [93] R. E. HONIG AND R. O. HOOK. **Vapor pressure data for some common gases.** *RCA Rev.*, **21**:360, 1960.
- [94] M. SCHEIBNER, T. SCHMIDT, L. WORSCHNECH, A. FORCHEL, G. BACHER, T. PASSOW, AND D. HOMMEL. **Superradiance of quantum dots.** *Nature Physics*, **3**(2):106–110, 2007.
- [95] A. AUFFÈVES, D. GERACE, S. PORTOLAN, A. DREZET, AND M. FRANÇA SANTOS. **Few emitters in a cavity: from cooperative emission to individualization.** *New Journal of Physics*, **13**:093020, 2011.
- [96] HAO LEE, WEIDONG YANG, AND PETER C. SERCEL. **Temperature and excitation dependence of photoluminescence line shape in InAs/GaAs quantum-dot structures.** *Phys. Rev. B*, **55**:9757–9762, Apr 1997.
- [97] MD LAHAYE, J. SUH, PM ECHTERNACH, KC SCHWAB, AND ML ROUKES. **Nanomechanical measurements of a superconducting qubit.** *Nature*, **459**(7249):960–964, 2009.
- [98] CA REGAL, JD TEUFEL, AND KW LEHNERT. **Measuring nanomechanical motion with a microwave cavity interferometer.** *Nature Physics*, **4**(7):555–560, 2008.
- [99] P. RABL, P. CAPPELLARO, M.V.G. DUTT, L. JIANG, JR MAZE, AND M.D. LUKIN. **Strong magnetic coupling between an electronic spin qubit and a mechanical resonator.** *Physical Review B*, **79**(4):041302, 2009.
- [100] O. ARCIZET, V. JACQUES, A. SIRIA, P. PONCHARAL, P. VINCENT, AND S. SEIDELIN. **A single nitrogen-vacancy defect coupled to a nanomechanical oscillator.** *Nature Physics*, **7**(11):879–883, 2011.
- [101] S. KOLKOWITZ, J.A.C. BLESZYNSKI, Q. UNTERREITHMEIER, S.D. BENNETT, P. RABL, JG HARRIS, AND M.D. LUKIN. **Coherent Sensing of a Mechanical Resonator with a Single-Spin Qubit.** *Science (New York, NY)*, 2012.
- [102] O. ARCIZET, P.F. COHADON, T. BRIANT, M. PINARD, A. HEIDMANN, J.M. MACKOWSKI, C. MICHEL, L. PINARD, O. FRANCAIS, AND L. ROUSSEAU. **High-sensitivity optical monitoring of a micromechanical resonator with a quantum-limited optomechanical sensor.** *Physical review letters*, **97**(13):133601, 2006.
- [103] L. TIAN AND P. ZOLLER. **Coupled ion-nanomechanical systems.** *Physical review letters*, **93**(26):266403, 2004.
- [104] K. HAMMERER, M. WALLQUIST, C. GENES, M. LUDWIG, F. MARQUARDT, P. TREUTLEIN, P. ZOLLER, J. YE, AND HJ KIMBLE. **Strong coupling of a mechanical oscillator and a single atom.** *Physical review letters*, **103**(6):63005, 2009.
- [105] N. AKOPIAN, L. WANG, A. RASTELLI, OG SCHMIDT, AND V. ZWILLER. **Hybrid semiconductor-atomic interface: slowing down single photons from a quantum dot.** *Nature Photonics*, **5**(4):230–233, 2011.
- [106] G.W. BRYANT, M. ZIELIŃSKI, N. MALKOVA, J. SIMS, W. JASKÓLSKI, AND J. AIZPURUA. **Controlling the optics of quantum dots with nanomechanical strain.** *Physical Review B*, **84**(23):235412, 2011.
- [107] R. TROTTA, P. ATKINSON, JD PLUMHOF, E. ZALLO, RO REZAEV, S. KUMAR, S. BAUNACK, JR SCHRÖTER, A. RASTELLI, AND OG SCHMIDT. **Nanomembrane Quantum-Light-Emitting Diodes Integrated onto Piezoelectric Actuators.** *Advanced Materials*, 2012.
- [108] KD JÖNS, R. HAFENBRACK, R. SINGH, F. DING, JD PLUMHOF, A. RASTELLI, OG SCHMIDT, G. BESTER, AND P. MICHLER. **Dependence of the Redshifted and Blueshifted Photoluminescence Spectra of Single In_{1-x}Ga_x(1-x)As/GaAs Quantum Dots on the Applied Uniaxial Stress.** *Physical Review Letters*, **107**(21):217402, 2011.

REFERENCES

- [109] JR GELL, MB WARD, RJ YOUNG, RM STEVENSON, P. ATKINSON, D. ANDERSON, GAC JONES, DA RITCHIE, AND AJ SHIELDS. **Modulation of single quantum dot energy levels by a surface-acoustic-wave.** *Applied Physics Letters*, **93**:081115, 2008.
- [110] M. METCALFE, S.M. CARR, A. MULLER, G.S. SOLOMON, AND J. LAWALL. **Resolved sideband emission of InAs/GaAs quantum dots strained by surface acoustic waves.** *Physical review letters*, **105**(3):37401, 2010.
- [111] TY WANG AND GB STRINGFELLOW. **Strain effects on $GaxIn_{1-x}As/InP$ single quantum wells grown by organometallic vapor-phase epitaxy with $0 < x < 1$.** *Journal of applied physics*, **67**(1):344–352, 1990.
- [112] W. SHOCKLEY. **Energy band structures in semiconductors.** *Physical Review*, **78**(2):173, 1950.
- [113] G.L. BIR AND G.E. PIKUS. *Symmetry and strain-induced effects in semiconductors*, **624**. Wiley New York, 1974.
- [114] J. D. PLUMHOF. *Strain-tuning of single semiconductor quantum dots*. PhD thesis, Technischen Universität Chemnitz, 2012.
- [115] S.L. CHUANG. **Efficient band-structure calculations of strained quantum wells.** *Physical Review B*, **43**(12):9649, 1991.
- [116] S.L. CHUANG. *Physics of photonic devices*, **69**. Wiley, 2009.
- [117] CHRIS G. VAN DE WALLE. **Band lineups and deformation potentials in the model-solid theory.** *Phys. Rev. B*, **39**:1871–1883, Jan 1989.
- [118] F.H. POLLAK. **Effects of homogeneous strain on the electronic and vibrational levels in semiconductors.** *Strained-layer superlattices: physics*, **32**:17–53, 1990.
- [119] B. LEGRAND, B. GRANDIDIER, JP NYS, D. STIEVENARD, JM GERARD, AND V. THIERRY-MIEG. **Scanning tunneling microscopy and scanning tunneling spectroscopy of self-assembled InAs quantum dots.** *Applied physics letters*, **73**:96, 1998.
- [120] B. GRANDIDIER, YM NIQUET, B. LEGRAND, JP NYS, C. PRIESTER, D. STIÉVENARD, JM GÉRARD, AND V. THIERRY-MIEG. **Imaging the wave-function amplitudes in cleaved semiconductor quantum boxes.** *Physical Review Letters*, **85**(5):1068–1071, 2000.
- [121] DM BRULS, J. VUGS, PM KOENRAAD, HWM SALEMINK, JH WOLTER, M. HOPKINSON, MS SKOLNICK, F. LONG, AND SPA GILL. **Determination of the shape and indium distribution of low-growth-rate InAs quantum dots by cross-sectional scanning tunneling microscopy.** *Applied physics letters*, **81**:1708, 2002.
- [122] A.N. CLELAND. *Foundations of nanomechanics: from solid-state theory to device applications*. Springer Verlag, 2003.
- [123] D. COHEN-TANUGI. *Anomalous Resonances of Nanowires: The Effect of Ion Beam Damage on the Vibrational Properties of Zinc Oxide Nanowires*. PhD thesis, Princeton University, 2009.
- [124] B. SANII AND P.D. ASHBY. **High sensitivity deflection detection of nanowires.** *Physical review letters*, **104**(14):147203, 2010.
- [125] A. GLOPPE. *High sensitivity optical readout of nanoresonator dynamics*. Master’s thesis, Grenoble INP university, 2011.
- [126] JS BLAKEMORE. **Key Papers in Physics, GaAs**, 1987.
- [127] P. MOHANTY, DA HARRINGTON, KL EKINCI, YT YANG, MJ MURPHY, AND ML ROUKES. **Intrinsic dissipation in high-frequency micromechanical resonators.** *Physical Review B*, **66**(8):085416, 2002.